Freie Universität Berlin

Fachbereich Biologie, Chemie, Pharmazie

Institut für Chemie und Biochemie

Core-Multishell Nanocarriers for the Topical Delivery of Pharmacophores

Dissertation

zur Erlangung des akademischen Grades

Doktor der Naturwissenschaften (Dr. rer. nat.)

vorgelegt von

Michael Unbehauen

aus Fulda

April 2018

Die vorliegende Arbeit wurde in der Arbeitsgruppe von Prof. Dr. Rainer Haag im Zeitraum von Februar 2014 bis April 2018 im Institut für Chemie und Biochemie der FU Berlin angefertigt.

1. Gutachter: Prof. Dr. Rainer Haag

2. Gutachter: Prof. Dr. Marcelo Calderón

Datum der Disputation: 23.5.2018

Acknowledgements

First of all, I'd like to thank Prof. Dr. Rainer Haag for the opportunity to conduct my PhD project in his working group. Prof. Dr. Marcelo Calderón is thanked for being my second referee and spanish sparring partner. Thanks also go to the whole AG Haag, but I want to mention a few people that most contributed directly or indirectly. Karolina Walker, thank you for being my postdoc, helping hand, partner in crime, perfect colleague and great friend. Balu, I am thankful for the help at getting the project going. Felix, Fang, Matthias, Sumati and Antara are thanked for the good time, interesting discussions (about scientific- and off-topics) and companionship throughout the past years. I also want to express my gratefulness to the people from our lab. Era, Anja, Manoj, Oli, Wan-Jun and Fatemeh, it was great working with you, big fun (in many ways), collaborational lab clean-ups and, discussions about societal things. The former 11:30 (now Weinhart) lunch group is thanked for providing input of a (mainly) different kind. Silke, Marie, Christoph, Daniel, Sabine, Katharina and Laura, billion-dollar ideas were just as important to talk about as the utter absurdities of life.

I also wish to thank Eike and Maren for their work in the lab, as well as Marleen and Carlo for everything they did to run the HPLC. The DendroPharm people are thanked, especially Emanuel, Florian and Markus, for the fruitful collaboration, scientific input and GPC measurements. I am also grateful to my collaborators abroad for letting conduct experiments in their labs: Priscila Schilreff and the whole crew from Quilmes, but also Nir Hananya, Doron Shabat and their team from Tel Aviv. Both times it was a truly amazing experience to see other labs and other (working) cultures.

The whole SFB 1112 is also thanked for having such productive collaborations. Stefan, Martina, Siavash, Hannah, Moritz, Nadine, Silke, Alexander, Pierre, Jonathan, it was great and productive fun. If there will be another student symposium, I will definitely go again. Maybe in Hawaii next time.

Last but not least, I want to mention the people who supported me more indirecty. Susanne, thank you for our valuable connection. My family, because you made me never lose the bigger picture, my (non-scientist) friends for reminding me that there's a world without science, and all my friends for making me feel at home here.

Abbreviations

5FU	5-fluorouracil
Ab	antibody
ABC	accelerated blood clearance
ADC	antibody-drug conjugate
AMD	age-related macular degeneration
bis-MPA	2,2-bismethylolpropionic acid
CD	cyclodextrin
CMC	critical micellar concentration
CMS	Core multi-shell
CS	core-shell
DB	degree of branching
DDS	drug delivery system
DNA	desoxyribonucleic acid
DXM	dexamethason
DOX	Doxorubicin
EPR	enhanced permeability and retention
FLIM	fluorescence lifetime imaging
GSH	glutathione
GSSG	glutathione disulfide
HBPH	hyperbranched polyhydroxyl polymer
HPAA	hyperbranched poly(amido amine)s
hPG	hyperbranched polyglycerol
hPG-NH2	hyperbranched polyglycerol amine
HPMA	N-(2-hydroxypropyl)methacrylamide
LUV	large unilamellar vesicles
MLV	multi-lamellar vesicles
MW	Molecular weight
NSAID	non-steroidal anti-inflammatory drugs
PAMAM	poly(amido amine)
PCL	poly(caprolactone)
PDEA	poly(2-(N,N-diethylamino)ethyl methacrylate)

PDI	polydispersity index
PE	polyethylene
PEG	poly(ethylene glycol)
PEI	poly(ethylene imine)
PES	polyesters
PLA	poly(lactic acid)
PLGA	poly(lactide-co-glycolide)
PS	photosensitizer
PVP	poly(N-vinylpyrrolidone)
SC	stratum corneum
SUPR	super enhanced permeation and retention
SUV	small unilamellar vesicles
THP	tetrahydropalmatine
T_m	melting temperature
ZnPc	Zn-phthalocyanine

Table of Contents

1 Introduction

1.1 Topical Drug Delivery

Controlled drug delivery is a concept based on Paul Ehrlich's Idea of the magic bullet. It deals with the effect of a drug only in the way it is intended without any side effect.[1] In the more than 100 years that have passed since the conception of this hypothesis, much research has been conducted towards its realization.

Side effects often come into play when a drug, for instance, binds to a different receptor in an unspecific manner. This usually happens, when the drug's concentration in the target tissue is too high or the drug enters a tissue with other potential binders being present. Increasing the specificity to the target receptor by chemical modification is one way to solve this problem, but it has its limits. Another way is to use nanomedicine. It helps to increase the drug's effectiveness, for example, by gaining control over the spatial distribution or by an improved control over the concentration in the target tissue. There is a minimum required concentration for an effect to occur and an upper limit, which marks the onset of toxic effects, caused by, e.g., non-specific binding (See Figure 1).

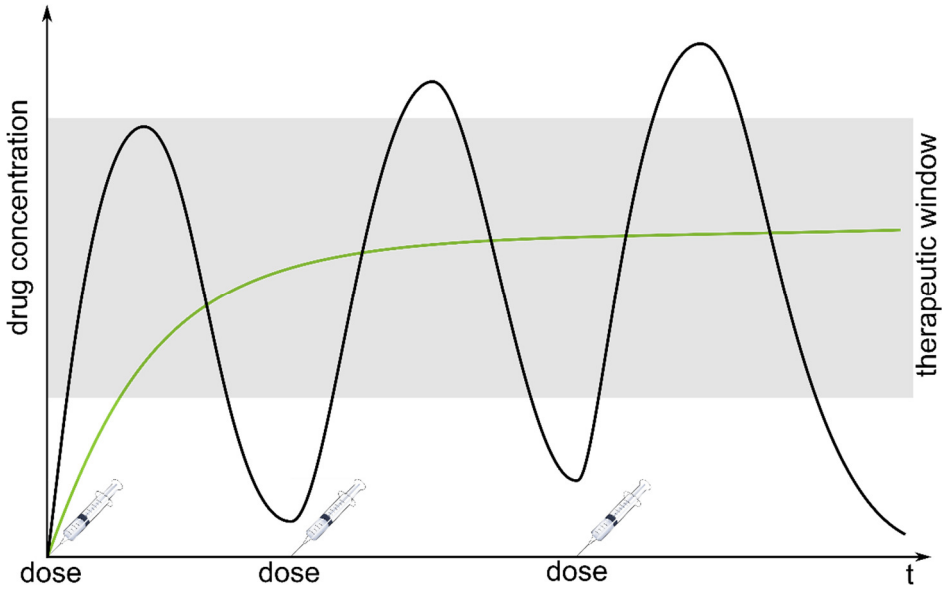

Figure 1. The drug concentration in the blood over the course of a medical treatment. By the administration of a small molecular drug (black curve), many dosages are needed and blood concentration varies strongly, even below and above the therapeutic window. Using the controlled release from a nanomedicine, the drug concentration is ideally kept within the therapeutic window in a single dosing. Modified from ref. [2].

The interval in between is called the therapeutic window and marks the effective range of concentration for a drug. Especially for cytotoxic anti-cancer drugs the therapeutic window can be very narrow.[3]

1.2 Nanomedicines

The task of nanomedicines is to gain control over the drug's distribution over the body in a temporal manner. This means on one hand to direct the drug to the site of pharmacological need, and on the other hand to maintain the drug's concentration within the therapeutic window. Examples for nanomedicines are antibody-based systems like antibody-drug conjugates (ADC),[4] or synthetic systems like micelles, liposomes, polymeric micelles, and polymer beads. All these systems are loaded with a drug either via covalent attachment or by physical entrapment. Depending on their properties, they can provide passive or active targeting, triggered release and protection from premature clearance, which is a common problem of low-molecular weight drugs. This can be prevented by the attachment of the drug to a nanoscale DDS with a molecular weight (MW) of > 30 kDa, which marks the limit for the renal excretion.[5]

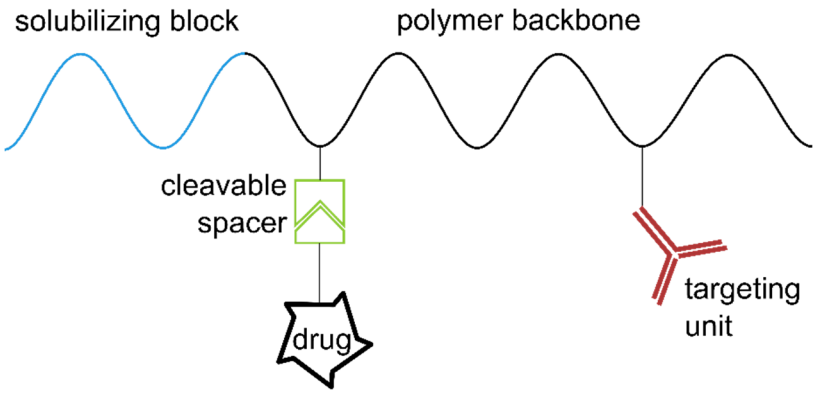

Figure 2. Visualization of Ringsdorf's model of a pharmacologically active polymer, adapted from ref. [3]

The concept, which first included these ideas and involved polymers for their realization, is Ringsdorf's model of the pharmacologically active polymer (see Figure 2).[6] In this model, a polymer was thought of as a modular platform that can provide certain properties to form a pharmacologically active architecture. In this concept, an active targeting unit (e.g. an antibody) can be attached to a partly hydrophilic block-copolymer which is bound to a hydrophobic drug through a cleavable linker. The hydrophilic block provides the necessary water solubility to an otherwise insoluble drug. The active targeting unit recognizes specific binding motifs on a target cell and

directs the polymer to its destination. Once the target is reached, the linker is cleaved and the released drug becomes active.

Along with the active targeting, which involves a specific binding, there is a second form, the passive targeting. A key mechanism of passive targeting is enhanced permeation and retention (EPR) effect which was first described by Maeda and coworkers in 1986.[7] It is based on the special condition of tumorous and inflamed tissue. Because of irregular growth of cells, the vasculatory system is more permeable for macromolecules and the tumor tissue fenestrated.[8] Macromolecules such as nanoscopic DDS are able to transcend into the target tissue. As lymphatic drainage is impaired in these types of tissues the macromolecules are retained and their cargo is more likely to be released. Additionally, tumor growth and inflammations are accompanied with low pH in the tissue. This condition can be used for a pH-dependent release (see chapter 1.4).

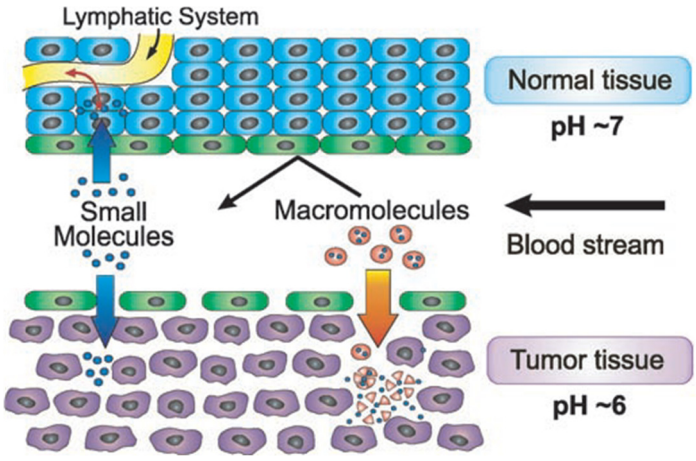

Figure 3. Schematic description of the EPR effect. Normal tissue (top) is not penetrated by macromolecules. Alterations in the structure of tumorous tissue lead to increased penetration of nanoscopic DDS and higher length of stay due to the lack of lymphatic drainage. Reproduced with permission from John Wiley and Sons.[9]

Based on the EPR effect, more sophisticated mechanisms of action have been developed. The super enhanced permeation and retention effect (SUPR) is a two-step procedure and involves an antibody (Ab)-bound photosensitizer.[10] In a first step, this ADC is injected intravenously and locates in the tumor tissue due to the specific binding of the Ab. Upon the irradiation of light, singlet oxygen is generated locally, which leads to the immediate necrotic cell death without harming the nearby normal tissue. Due to the tissue damage, the perfusion of the tumorous tissue is strongly elevated and the EPR-effect for nanoscopic therapeutics administered in a second step enhanced.

1.3 Classes of Nanomedicines

There are many types of nanomedicines of which can be subdivided into two classes. Polymer therapeutics describe all types of nanosized polymer-drug conjugates at which a small drug or protein is bound to a polymer covalently.[11] In contrast to that a Drug delivery system is an architecture that physically entraps the drug without a covalent linkage.

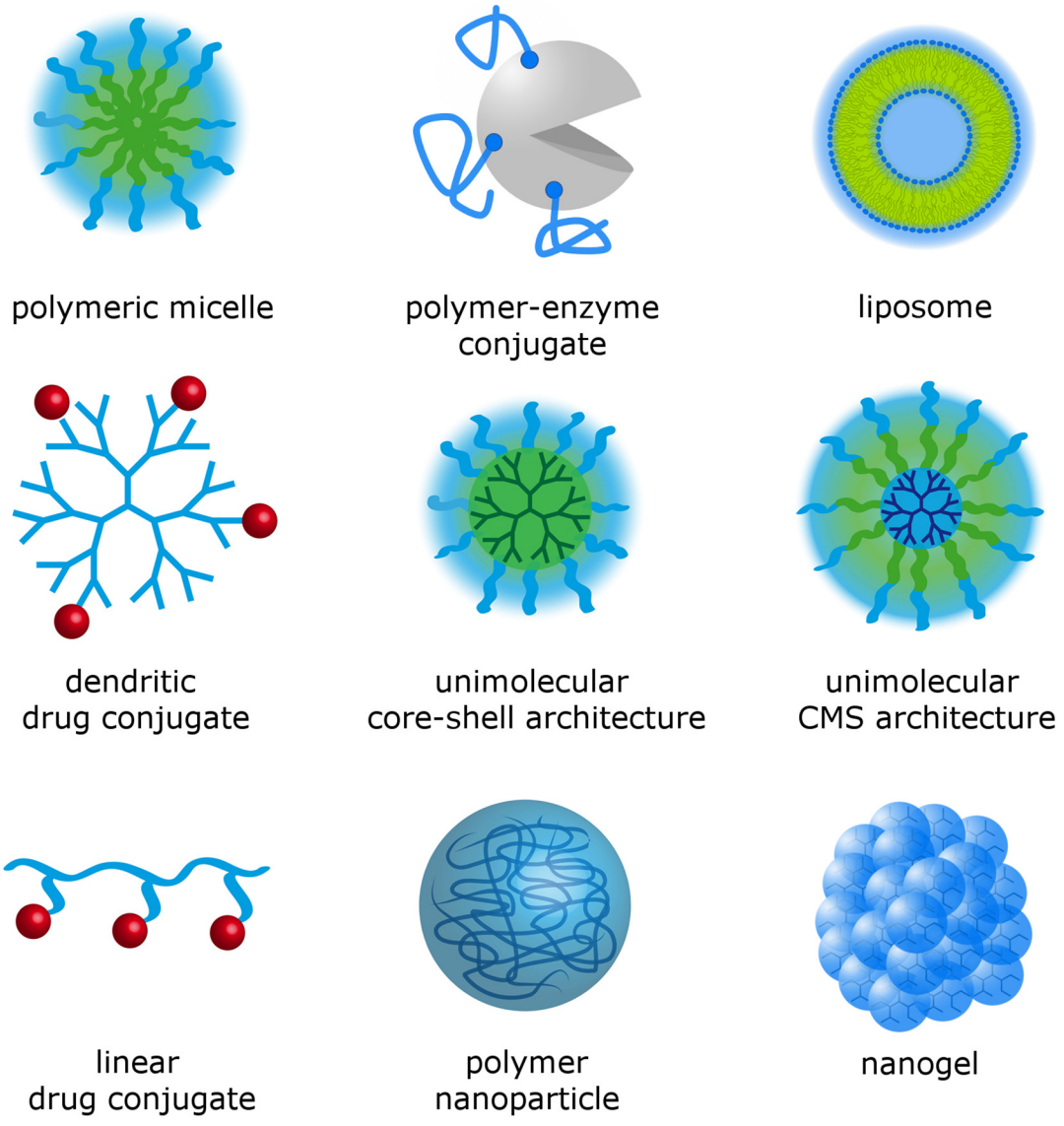

Figure 4. Structural variety of polymeric nanomedicines. Modified from [12].

1.1.1 Polymer therapeutics

The most typical way to alter a drug's or protein's properties is by conjugation with poly(ethylene-glycol) (PEG), N-(2-hydroxypropyl)methacrylamide (HPMA), or polyglutamate with typical molecular weights of 5 kDa to 40 kDa.[13] This leads to extended half-life in blood plasma, improved stability towards degradation and

shielding from recognition by the immune-system. In the case of conjugated small drug, the molecular weight is increased by one or several orders of magnitude to the range of the EPR effect. This strategy has been employed to a multitude of drugs and proteins, of which > 10 have entered the market and > 10 more are in clinical trials.[11] For example, Oncaspar, a PEGylated asparaginase was introduced into the market in 1994.[14] L-asparagine is a non-essential amino acid, which can be produced by normal cells, but not by cancer cells and thus has to be taken up from the blood stream. Oncaspar catalyzes the hydrolysis of asparagine and thus deprives the cancerous tissue of its asparagine source which slows down tumor growth. ProLindac is a platinum-based anti-cancer drug bound to a HMPA backbone via a pH-degradable linker.[15] Based on the EPR-effect, the conjugate accumulates in the tumor tissue, where the cis-platinum is released and thereby its cytotoxic effect activated.

1.1.2 Liposomes

Another big group of nanomedicines currently used in practice is made up by liposomal formulations.[16] Liposomes are lamellar vesicles with usually 50 to 150 nm in diameter that comprise an aqueous volume surrounded by a phospholipid bilayer.[17] The phospholipids typically used are amphiphilic molecules with fatty acids as lipophilic tails and a zwitterionic hydrophilic head group. While small unilamellar vesicles (SUV, 25 - 100 nm) and large unilamellar vesicles (LUV, 100 - 500 nm) possess only a single phospholipid bilayer as a membrane, multi-lamellar vesicles (MLV, 200 – 1000 nm) exhibit several ones. Verteporfin, for instance, is an injectable liposomal formulation of a porphyrin-type photosensitizer (PS) for the treatment of age-related macular degeneration (AMD). [18–20] In the more severe, so-called wet form of AMD, the macula is neovascularized. The newly formed, abnormal blood vessels are leaky and damage the surrounding tissue. The application of Verteporfin involves two steps. First, an enrichment of PS in the target tissue due to the nanoformulation takes place, which is the first way to limit the effect locally. Then, again locally, the macula is irradiated with red laser light to induce the generation of singlet oxygen and the subsequent damage to the endothelial cells. Platelet adhesion then leads to an occlusion of the abnormal blood vessels and stops the leakage.

Nanoliposomally formulated doxorubicin (Doxil) poses an example of a more complex design.[21,22] Doxorubicin is loaded into vesicles that bear PEG chains grafted onto the outer side of the membrane (see Figure 5). Doxil is then administered

intravenously and the liposomes, protected from the immunorecognition by the PEG-layer accumulate in the target tissue where it is released.

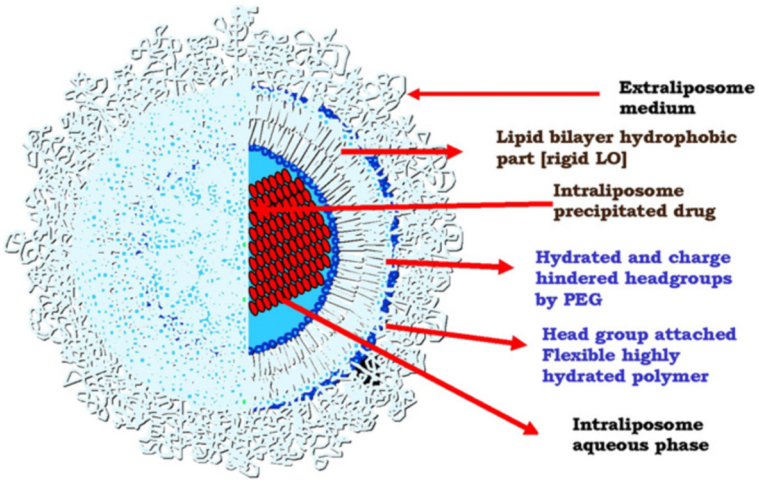

Figure 5. Structure of the liposomal formulation of DOX, doxil. Reproduced with permission from Elsevier.[22]

1.1.3 Polymeric micelles

Polymeric micelles are the polymeric analogs of small-molecular micelles. They self-assemble out of single polymeric molecules that form bigger structures driven by hydrophobic interactions.[23] In the same way they possess a hydrophobic part that forms the core, where lipophilic drugs can be solubilized, as well as one or two hydrophilic parts which assemble into the hydrophilic shell. The formation of the micellar structure is a concentration-dependent process, which means that a constant dynamic exchange of polymer chains takes place and dilution will lead to the disassembly. The micellar stability is expressed by the critical micellar concentration (CMC), the minimum concentration above which association to micelles takes place. The combination of materials used in this type of architecture also has a strong influence on its stability. As hydrophilic block, PEG is a commonly used material, because of its water solubility and its good biocompatibility. Still, some studies indicated the limitations of PEG, pointing out the accelerated blood clearance (ABC) phenomenon.[24,25] It describes the faster clearance of PEG-based micelles from the blood stream at the administration of the second dose in an IgM-mediated manner and indicates at least some immunogenicity of PEG. Other hydrophilic polymers used for polymeric micelles include poly(N-vinylpyrrolidone) (PVP) and the polyzwitterionic polybetaines. PVP has similar properties to PEG, it's biocompatible and hydrophilic, but is not as good in terms of resisting protein adsorption.[26] However, it has proven to not elicit the ABC phenomenon.[27]

As polymeric materials for the hydrophobic block biodegradable polyesters are commonly used. These include poly(lactic acid) (PLA),[28] poly(lactide-co-glycolide) (PLGA),[29] and poly(caprolactone) (PCL).[30] The usage of degradable materials ensures the complete degradation and prevents accumulation in the body.

Even though they're much more stable than their small-molecular counterparts (CMC 10^6-10^7 M, vs. 10^3-10^4 M),[31] polymeric micelles still undergo disassembly when diluted in a large volume, e.g. during *i.v.* injection. To overcome this problem, common attempts were made to crosslink the micelle in the hydrophobic core with cleavable linkages to maintain biodegradability and achieve a triggered release.[32]

In addition to the two blocks, further functionalization is possible and building blocks can be used for multiple purposes. In a recent example by Low et al., oligoaspartic acid was used as the hydrophilic block and targeting unit at the same time. At the hydrophobic terminus, doxorubicin, which contributed to the hydrophobic interactions, was attached covalently via a hydrazone bond, to provide a pH-dependent release (see Figure 6). [33]

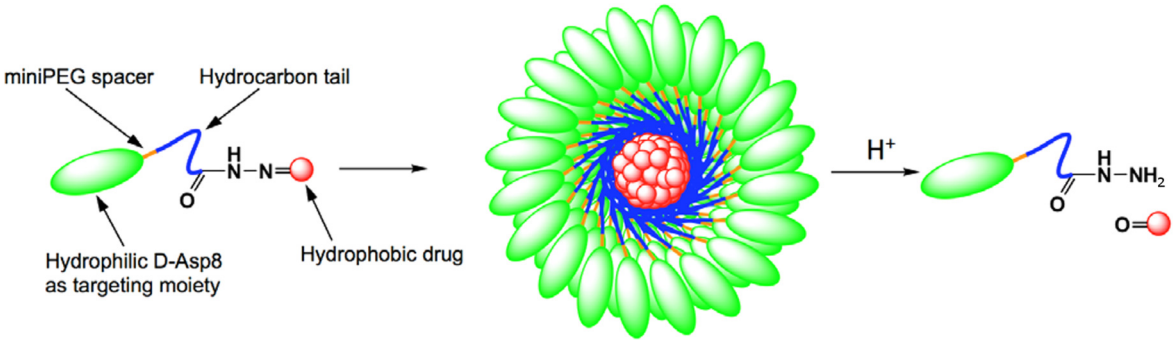

Figure 6. Structure of the polymeric chain and release principle of the polymeric micelles presented by Low et al. adapted from ACS ref. [33]*. This is an unofficial adaptation of an article that appeared in an ACS publication. ACS has not endorsed the content of this adaptation or the context of its use.*

1.1.4 Dendritic polymers

Dendrimers are polymers with globular shape and many highly branched arms originating from a focal point.[34] Their step-wise synthesis leads to highly defined macromolecules with a low dispersity and a precise number of end groups. In contrast to that, a hyperbranched polymer has a highly branched structure a high surface functionality, but also contains linear units. While dendrimers are identical molecules, hyperbranched polymers vary in MW and even two molecules with equal mass are most probably constitutional isomers. Thus, hyperbranched polymers are closely related to dendrimers but are synthesized via a much more direct route.

The combination of linear and dendritic polymers yields a plethora of structural possibilities.[35] These include linear-dendritic hybrids, a dendrimer functionalized with a linear chain at the center, multi-arm star polymers, a hyperbranched polymer decorated with linear chains, and dendrigrafts as well as hypergrafted polymers, linear chains to which either dendrimers or hyperbranched polymers are attached (see Figure 7).

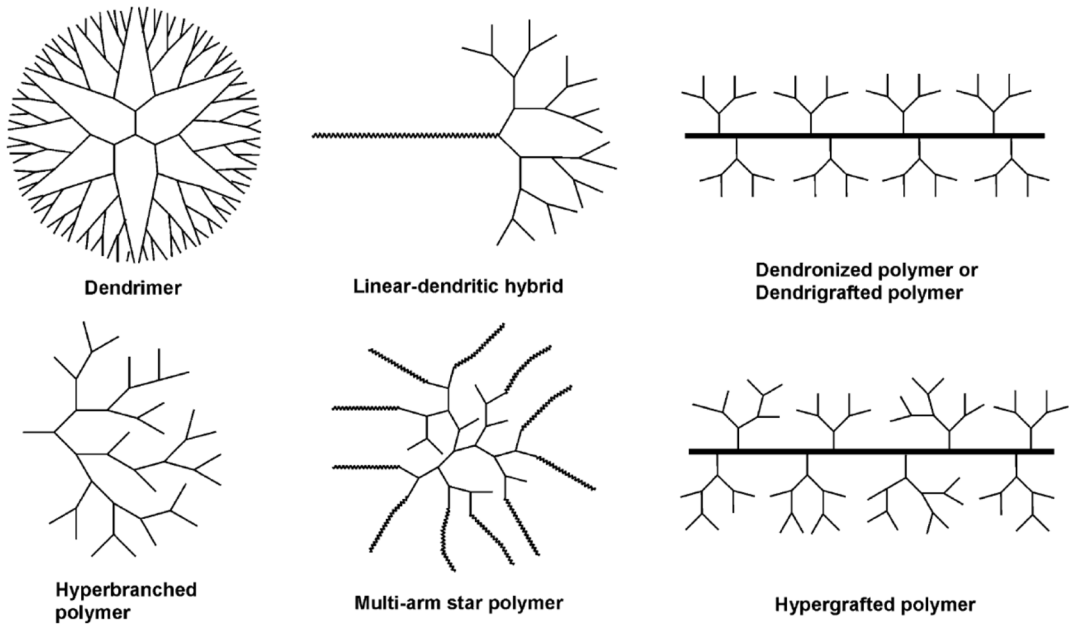

Figure 7. Different dendritic polymeric architectures. For more information see text. Reproduced with permission from Elsevier.[35]

1.1.4.1 Dendrimers

Dendrimers first emerged in the 1980's, when they were theoretically described by DeGennes after which Tomalia et al. realized the synthesis of the first example, the poly(amido amine) (PAMAM) dendrimer (see Figure 9).[36,37] Since then this new class of polymers has been explored with many other building blocks and different routes of synthesis. As full branching was the goal, usually AB_X-type monomers were used. (where X = 2,3,…) While in the divergent route the synthesis is started at the focal point and from then on, all peripheral groups are functionalized with another monomer, to form the next higher generation of a dendrimer,[36] in the convergent route this direction is inverted.[38] Here, the synthesis is started from the end groups and is completed by the attachment to the focal point. As in both types of synthetic strategies the generation is only extended by one, it is crucial that all reactive groups

bind exactly one additional monomer. This is typically done via the usage of either a protective group, or two chemically orthogonal reactions.[39]

The materials used to construct this type of polymers include hydrophobic polyarylethers,[38] dendritic PEG-analogs,[40] and polyester-based dendrimers (e.g. Boltorn H30, see Figure 9) have been synthesized and while in the early years,[41] the main focus lay on dendrimer chemistry, it has shifted more and more towards biomedical applications. Like their linear counterparts, dendrimers bear numerous functional groups, but there are many structural differences. Linear polymers are often more polydisperse and arrange in a random coil structure. In contrast to that, dendrimers are more globular, and their physiochemical properties often differ between their inner, often hydrophobic part and their surface, where many of the functional groups are located. These characteristics can be exploited for numerous biomedical applications.[42] An application for a lysin-based, surface-functionalized dendrimer as a microbicide against HIV and HSV is SPL 7013 (marketed as VivaGel®).[43,44] Its polyanionic surface allows one to bind to the surface of a virus by multivalent interactions and thereby prevents an infection. It is an example for a dendrimer to act as a drug itself, but it can also be used as a drug container. The reported dendritic box by the Meijer group was one of the first examples for this type of use.[45] The authors describe a G5 poly(propylene imine) dendrimer whose surface was decorated with Boc-protected phenylalanine in the presence and absence of various guest molecules (see Figure 8A). While for low-generation dendrimers, the guest molecules could still diffuse out of the container, the steric hindrance of the peripheral functionalization in the case of the high generation dendrimers was too high for the guest to leave the dendritic box. The authors also showed selective release after the co-encapsulation of two differently sized guest molecules. By cleaving off the Boc-protecting group, the smaller guest was released, while the removal of the amino acid was necessary to also free bigger guest (see Figure 8B).[46]

The dendrimer's interior can also as a hydrophobic pocket to bind an unpolar drug via hydrophobic interactions and a hydrophilic surface to increase water solubility.[47] For example, the solubility of a set of non-steroidal anti-inflammatory drugs (NSAIDs) could be improved by the encapsulation into PAMAM. In this study, not only hydrophobic interactions played a role, but also hydrogen bonding between the amines of the PAMAM dendrimers and the carboxylic acid of the NSAIDs.

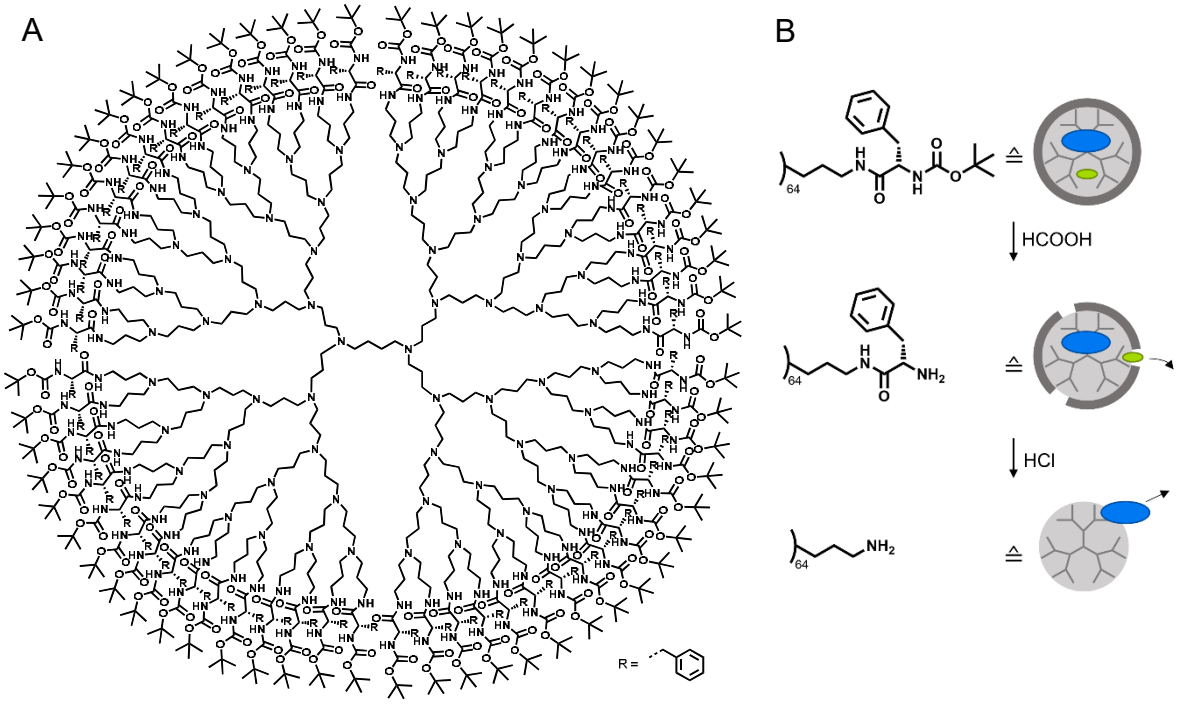

Figure 8. (A) Chemical structure of the "dendritic box" by de Meijer and co-workers. (B) Co-encapsulation of two differently sized guest molecules with subsequent selective release after deprotection and removal of the amino acid. [45,46]

Dendrimers with a hydrophobic interior and hydrophilic surface groups are generally not efficient carriers, because of their low water solubility. Additionally, polycations, such as polyamines usually have the problem of increased toxicity due to adherence to the negatively charged cellular membrane. To circumvent these problems, many dendrimers are PEGylated, forming a core-shell particle with a hydrophobic interior and a hydrophilic exterior, a unimolecular micelle (see section 1.1.6).

1.1.4.2 Hyperbranched polymers

Although dendrimers exhibit a perfectly branched structure and well defined molecular properties, their major drawback is their tedious synthesis. Hyperbranched polymers are far more accessible, because they can be produced in a one-step approach. Hyperbranched polymers are not perfectly branched but exhibit a certain percentage of linear monomeric units in their interior. The degree of branching is an important value to describe the character of a certain dendritic polymer as rather dendritic or linear. Unlike their fully branched counterparts, hyperbranched polymers are not limited to a certain generation and size, respectively. First examples have already been synthesized in the 19th century,[48] first theoretic description was done by Flory in 1941.[49] The interest for hyperbranched structures increased since the 1980's.

Many synthetic strategies have been developed involving either a single AB_2-type monomer or two different (typically A_2 and B_3) monomers.[35]

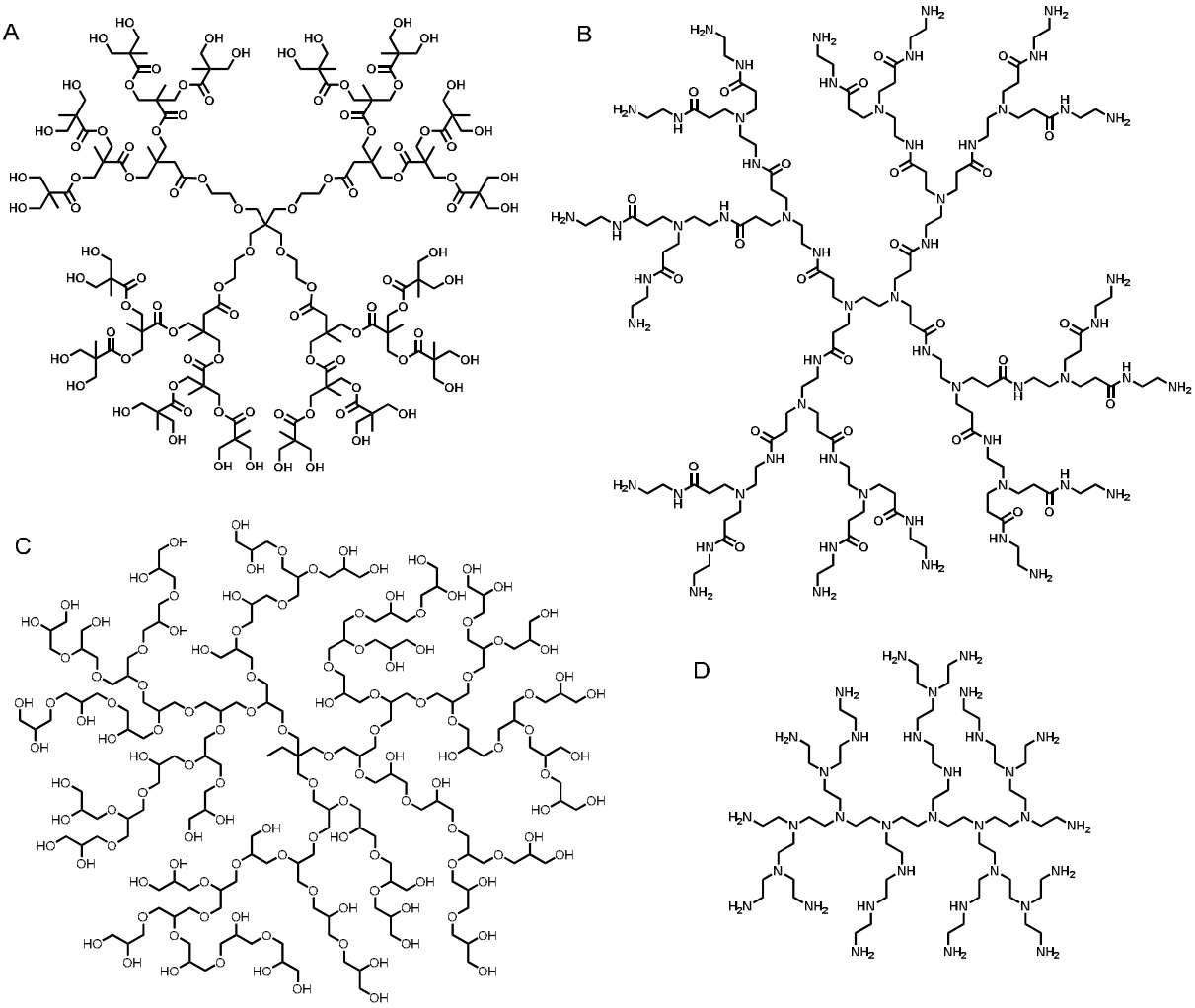

Figure 9. Chemical structure of different dendrimers (A,B) and hyperbranched polymers (C,D). (A) Boltorn H30, (B) poly(amido amine) G3, (C) hyperbranched polyglycerol, (D) poly(ethylene imine).

Due to their characteristics, hyperbranched polymers have been explored for a multitude of biomedical applications. A water-soluble hyperbranched polyhydroxyl polymer (HBPH) was used for the encapsulation of apoptosis-initiating cytochrome C and a near-IR dye.[50] The additional covalent attachment of folic acid ligands yielded theranostic nanoparticles for the passive and active targeting of folate receptor-positive cancer cells. Poly(ethylene imine) (PEI, see Figure 9) is a hyperbranched polyamine, that, among other applications, is used in gene transfection.[51,52] PEI of the molecular weight of 50 kDa and 800 kDa was employed as a DNA-carrier. The interaction of DNA and PEI is based on ionic interactions between the anionic poly sugar-phosphate backbone and the polycation PEI. In addition to that, the “proton-sponge effect” increases the endosomal escape of endocytosed genetic material

significantly. It describes the role of PEI as a polymer that binds protons due to its manifold amine groups and acts as a pH buffer. The results are first of all that transfected DNA is not degraded in the relatively mild environment and secondly that lysosomal swelling and rupture is the basis of the escape mechanism. Like PEI, hyperbranched poly(amido amine)s (HPAAs) can also be used for gene delivery. Chen et al. reported a cyclodextrin (CD)-decorated HPAA which could be used as a gene delivery vector.[53] The additional functionalization with CD increased the fluorescence of the material as well as could encapsulate rhodamine B as a model drug.

Tolerability and toxicity was improved while keeping the transfection efficiency in the same range by the usage of aminated hyperbranched polyglycerol (hPG-NH_2) instead of PEI.[52,54] Hyperbranched polyglycerol (hPG) is a polyether with few internal and many superficial -OH groups that provide both hydrophilicity and the possibility of functionalization (see Figure 9). It was shown that hPG-NH_2 could bind and transfect DNA in a comparable manner as PEI, the major difference lay in the charge of the hyperbranched polymer. While PEI has additional amine groups in its interior that contribute to its toxicity, amino-functionalization in hPG-NH_2 is only superficial, leading to an increased tolerability.

hPG (see Figure 9) is a highly branched (DB typically between 0.53 and 0.59), hydrophilic polymer that can be produced with a low PDI (1.1 to 1.5) via an anionic ring-opening multibranching polymerization from glycidol and a starter molecule.[55] Its biocompatibility, low toxicity, and high density of functional groups have made it a promising and well explored material for biomedical applications.[56–59] For example, it was used as a water-soluble polymer backbone for the delivery of drugs and cells. Jeong et al. functionalized hPG with a long alkyl chain as well as vascular binding peptide. This construct was then used to target stem cells to inflamed tissue, via the alkyl chain inserting into the cellular membrane and the oligopeptide binding to receptors on the inflamed endothelium.[60] González-Rodríguez et al. reported a hPG-morphine conjugate which passively targeted inflamed tissue and thus induced analgesia peripherally without side effects by acting on the central nervous system.[61] Low MW hPG can be employed in organ-preserving solutions. It was shown that the usage of hPG of a MW of 1 kDa was advantageous over the commonly used hydroxyethyl starch HES in cold storage of kidney and heart transplants.[62,63] hPG-

based solutions also outperformed the current gold standard, University of Wisconsin (UW) solution for the perfusion of organs before transplantation.[64] In this context, hPG was used to maintain the colloidal osmotic pressure and due to its hyperbranched architecture exhibited a low intrinsic viscosity compared to linear polymers, which was beneficial for this application. Among the vast number of applications that use hPG as a solubilizer, bind drugs and proteins or employ superficially functionalized hPG, numerous approaches exploit hPG as a building block for higher architectures, such as nanogels, core-shell and core-multishell architectures.[65]

1.1.5 hPG-based nanogels

Size is a critical issue when it comes to the fate of nanoparticles applied to the body. Thus gel-like, hydrophilic polymeric particles in the size range from 20 to 1000 are especially promising for biomedical applications.[66,67] To generate hPG particles of a size greater than 20 nm, different strategies were employed. Sisson et al. reported PG particles of a high molecular weight in a miniemulsion-based approach. hPG macromonomers and cross-linking agents were emulsified in a nanoreactor that defined the size. Alkyne/azide click chemistry was used to link the monomers and yielded particles of 20 to 90 nm.[68] This procedure was then improved by Steinhilber et al. via the introduction of the inverse nanoprecipitation.[69] This surfactant-free method allowed the encapsulation of an enzyme into nanogels of 100 to 1000 nm in size. pH-dependent degradation was realized by acid-labile acetal linkages after which the released enzyme was fully intact. A similar approach was used by Dimde et al. who synthesized a hPG/PEI-based nanogel with acetal linkages using thiol-ene click chemistry.[70] siRNA was encapsulated during the synthesis and the loaded particles were taken up by GFP-expressing HeLa cells. The cargo was released upon intracellular pH drop which eventually led to the successful silencing the expression of GFP. Although being mainly hydrophilic architectures, Giulbudagian et al. achieved the encapsulation of the small hydrophobic drug dexamethasone (DXM) into β-cyclodextrin (β-CD)-functionalized thermoresponsive nanogels.[71] In their study they proved the binding between DXM and the β-CD via electron paramagnetic resonance spectroscopy and could show that the formulation into this nanogel outperformed a conventional DXM cream regarding penetration enhancement in human skin *ex vivo*.

1.1.6 Dendritic core-shell and core-multishell systems

Unimolecular micelles are single molecules and as such maintain their structure at all concentrations. This advantage makes them especially appealing for any applications that involve high dilutions, such as *i.v.* injections. The first example of a unimolecular micelle was reported in 1991 by Newkome et al.[72,73] In this approach, an aliphatic dendrimer with multiple peripheral carboxylate groups was synthesized in a divergent approach. The unloaded particles showed no aggregation and could loaded with several dyes to prove their capability to solubilize a hydrophobic molecule. Hawker and Frechét extended this principle to an electron-rich dendrimer which was synthesized in the convergent route.[74] Aromatic guest molecules could be loaded, while the system showed no CMC.

Since then the basic design principle of a lipophilic or hydrophilic interior and a water-soluble outer part was used to construct nanoparticles. With building blocks like dendrimers or hyperbranched polymers at hand, the obvious choice was to use them as a core and facilitate water solubility by the functionalization with a linear hydrophilic polymer to yield a dendric core-shell (CS) nanoparticle.[75] Particularly, PEG was chosen for this task because of its many advantages like its stealth effect, solubility in many solvents, and high biocompatibility. CS nanosystems with hydrophilic cores were generally used to encapsulate hydrophilic guests. For instance, a PAMAM-dendrimer was functionalized with PEG and folic acid for active and passive tumor targeting in a mouse model.[76] 5-Fluorouracil (5FU) was loaded up to 31% and the application a mouse tumor model led to high accumulation in the target tissue. A similar setup was chosen by Jin et al. who also used PAMAM and employed a mixed shell approach with PEG and the pH-sensitive poly(2-(N,N-diethylamino)ethyl methacrylate) (PDEA).[77] The nanocarriers were also loaded with 5FU and showed a pH-dependent release. At systemic pH (7.4), the release was significantly slower than at a pH of 6.5 and the carriers enabled an enhanced tumor accumulation of 5FU.

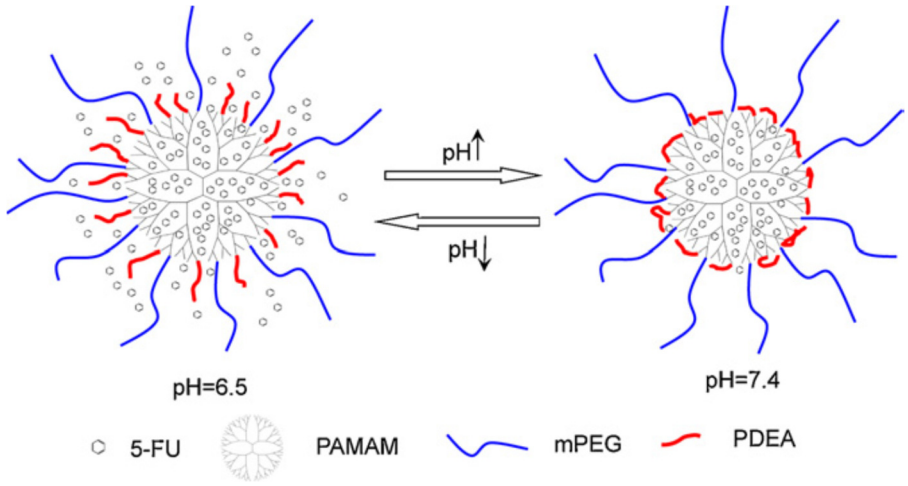

Figure 10. Illstration of the structure and release mechanism of the CS nanocarrier reported by Jin et al. The transporter can bo loaded wich 5FU and the additional functionalization with PDEA leads to pH dependent release. Reproduced with permission from Elsevier.[77]

For the encapsulation of hydrophobic guest molecules, the core needs to be hydrophobic. This can either be realized by the usage of a hydrophobic dendritic polymer or via the introduction of hydrophobic moieties in an otherwise hydrophilic core. Kurniasih et al. protected selectively the terminal 1,2-diols of hPG and functionalized the remaining ones selectively with different hydrophobic moieties.[78] The type of functionalization was adapted to the designated guest molecule by the usage of hydrophobic, fluorous-fluorous, or aromatic interactions. By deprotection, the hydrophilicity of the terminal groups was restored and a dendritic CS architecture obtained. The authors could prove that by this approach the water solubility of the loaded dyes increased manifold and the encapsulation involved supramolecular aggregates. The same authors extended a selected architecture bearing biphenyl groups at the core by the functionalization of the peripheral hydroxy groups with a PEG shell. [79] The resulting nanocarrier could then be co-loaded with pyrene and Nile red with interesting release properties. While pyrene was encapsulated into the unimers by π-π stacking, it could only be released via the enzymatic cleavage of the moieties in the core. Nile red, on the other hand, was solubilized in the nanocarrier aggregates and was released upon dilution or under acidic conditions.

A typical task in drug delivery is the solubilization of hydrophobic drugs with low water solubility. Thus, encapsulation into a core-shell architecture which a hydrophobic is the most promising approach. Mainly two types of polymers have been used, polyethylene (PE) and polyesters (PES). The first PE-based core-shell nanocarrier was reported by Chen et al. in 2003.[80] In a one-step synthesis they copolymerized

ethylene and a PEG-functionalized olefin to yield a polymer that formed a unimolecular core-shell structure in water and could be loaded with the dye Nile red. Another example is a PE-PG CS architecture reported by Popeney et al.[81] This nanotransporter could be loaded with hydrophobic dyes in a unimolecular fashion and enhance dye-uptake into A549 cells compared to an encapsulation in small molecular micelles. Although PE is a non-toxic material, it lacks bio-degradability, which is an important feature when it comes to biomedical applications. PES are commercially available materials and offer the possibility for biological degradation. The use of an AB_2-monomer (in this case bis-MPA) enables the synthesis of dendritic structures. The Boltorn H polymers (see Figure 9) are a commercially available material based on 2,2-bismethylolpropionic acid (bis-MPA) and were utilized for numerous approaches to unimolecular micelles. For example, Zeng et al. coupled PEG of various lengths (5 kDa and 10 kDa) to Boltorn H30 and H40 to construct CS nanocarriers. The carriers could then be loaded with doxorubicin (DOX) and exhibited an elevated cytotoxicity towards breast cancer cells compared to DOX alone. Additional functionalization of this setup with the bisphosphonate alendronate was reported by Chen et al.[82] The synthesized nanocarriers could also be loaded with DOX and showed binding to hydroxyapatite, which renders them promising candidates for the treatment of bone cancer.

1.1.6.1 Core-multishell (CMS) Nanocarriers

While core-shell nanoparticles mimic the structure of a micelle, the core multishell nanocarrier is inspired by the liposome (see Figure 11). In a unimolecular fashion, a hydrophilic dendritic polymer is surrounded by a lipophilic inner shell and a hydrophilic outer shell. The first report of this architecture was in 2007 by Radowski et al. who used a PEI core for the attachment of an amphiphilic double shell consisting of an aliphatic diacid and mPEG.[83] This universal CMS nanotransporter could transport both hydrophobic and hydrophilic guests in aqueous and organic media in an aggregation-based mechanism.[84] Depending on the guest molecule the nanocarriers exhibited a critical aggregation concentration (CAC). This is the minimum concentration above which the CMS nanocarriers aggregated supramolecularly and could transport hydrophobic dyes. The authors also showed that an indotricarbocyanine (ITCC)-loaded CMS-nanotransporters accumulated in an F9 carcinoma in mice due to the EPR effect. As PEI is a potentially toxic compound that

could be liberated in an enzymatic degradation, the core material was exchanged for hPG without change in the architecture.[85,86] Because of their versatility and biocompatibility, the CMS nanocarriers were explored regarding their drug-loading properties, aggregation phenomena, and biological applicability. Fleige et al. reported that not only the nanocarriers aggregate to form clusters in the size range of 100-200 nm, but also the loaded guest molecules can stack within those clusters.[86] Nile red, which was known to not aggregate, formed non-emissive H-stacks in this special nanoenvironment. SANS measurements confirmed the supramolecular nanoparticle aggregation but found a diameter of only 20 nm. Hydrophobic patches on the surface of the individual particles were identified as responsible for this effect.[87] Furthermore, the localization of the dye molecules within the aggregates was studied by UV/Vis spectroscopy,[86] fluorescence lifetime imaging (FLIM) and by a simplified theoretical model.[88,89] Not only small molecules can be transported by CMS-nanotransporters, but also other nanoparticles and metal ions. Pt-nanoparticles could be stabilized in a methanolic solution and could still catalyze a hydrogenation reaction.[90] For the loading of ions, a structurally altered CMS nanotransporter, which contained tertiary amines in the inner shell, was designed.[91] It was used to transport copper ions and release them in a pH dependent manner.

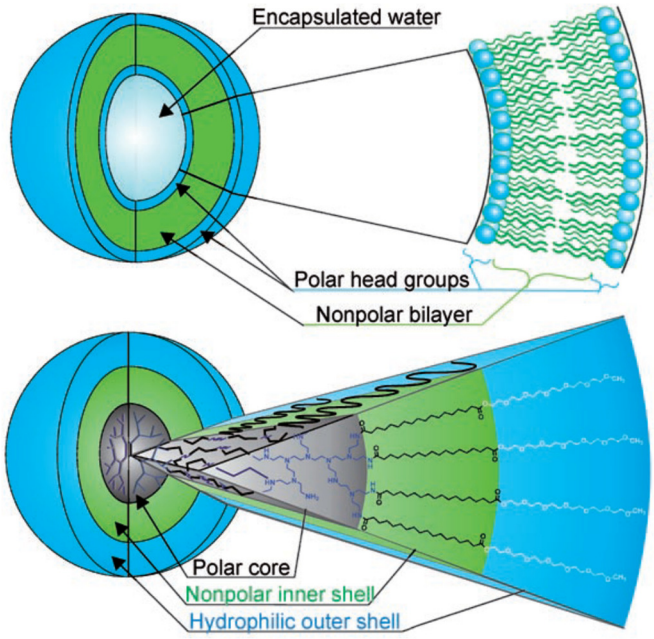

Figure 11. Schematic structure of the liposome compared to the CMS architecture. Reproduced with permission from John Wiley and Sons.[83]

Along with hPG and PEI, this parent architecture can be used with other dendritic polymers as a core. PES-based hyperbranched structures are especially promising if they are combined with polymeric shell arms, because they can be fully degraded. The combination of Boltorn H40, poly(lactic acid) (PLA), and PEG was used in several studies to construct CMS nanocarriers. Prabaharan et al. showed that their system was biocompatible and biodegradable and could be loaded with 5FU.[92] In a second study they additionally functionalized their system with folic acid. DOX-loaded particles were taken up by 4T1 mouse mammary carcinoma cells more rapidly when functionalized than without functionalization.[93] In a similar approach, Xu et al. utilized the same setup functionalized with an aptamer as a targeting ligand for the prostate-specific membrane antigen which is expressed in cancer cells. They found increased amounts of DOX when loaded into the targeted nanocarriers in comparison to untargeted ones *in vitro* as well as *in vivo*.[94]

1.4 Stimuli-Responsiveness

Many of the presented nanocarrier architectures can actively and passively target the desired tissue in a selective way. To gain even more or less control over the spatial and temporal distribution, stimuli responsive systems are used. Their main working principle is the triggered release which means not only site-specificity regarding the accumulation of particles, but also their release.[95] The release is facilitated by two major strategies (see Figure 12). The first one involves the introduction of a cleavable linker between the carrier molecule and the drug, forming a prodrug. Upon a certain stimulus, this bond is broken, and the bioactive agent liberated. In the second mechanism, the carrier reacts to a stimulus with a change in the carrier structure, e.g., by supramolecular aggregation, charging/discharging of functional groups, or even decomposition.

There is a multitude of stimuli that were used as a trigger for the release from nanocarriers that can be subdivided into two categories. Internal triggers are triggers that make use of certain conditions in the body that only exist in a confined space or undergo a change from one point in the body to another, e.g., from blood to a tumor or an inflammation. These include pH, enzymes, temperature, and redox potential. The second category, external stimuli offer an even more precise control over not only the spatial, but also the temporal distribution of a drug. They can be switched on and off in a controlled manner. So, they can come with an additional impact on patient

compliance. These external stimuli include, among others, light, magnetic field, and ultrasound.

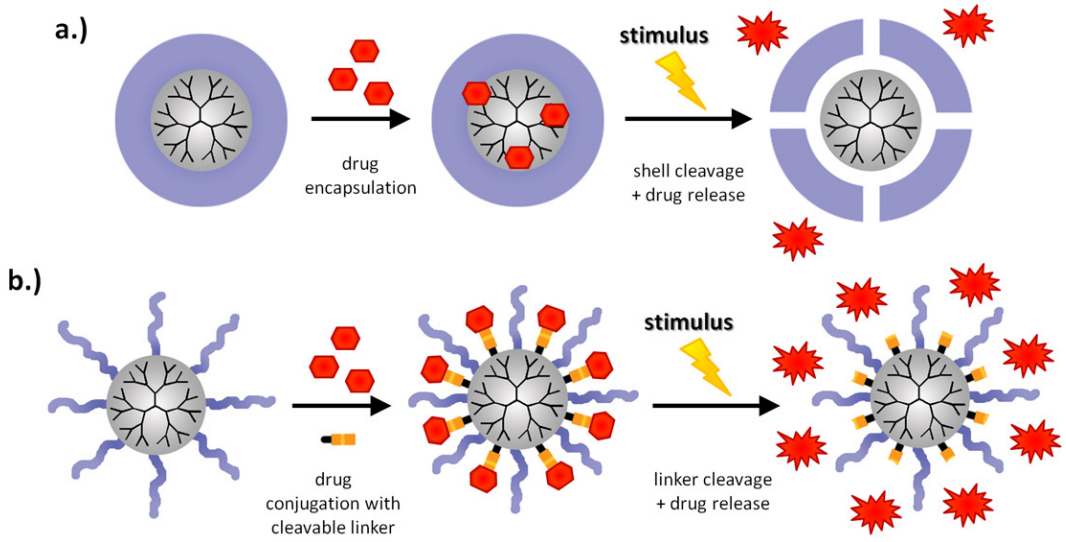

Figure 12. The two major strategies to facilitate triggered release. For details see text. Reproduced with permission from Elsevier.[95]

Redox potential changes from the rather oxidative extracellular space to the intracellular one in relation to the glutathione/glutathione disulfide (GSH/GSSG) concentration.[96] This redox potential difference can be used to cleave a redox-active bond, for instance, a disulfide bridge site-specifically. The change from the extracellular to the intracellular space is especially interesting for gene delivery, because the genetic material needs to be protected outside and should be liberated as soon as it reaches the intracellular space. Carlisle et al. complexed plasmid DNA with thiol-containing PEI which was further crosslinked via thiol or maleimide chemistry to form reducible disulfide or stable thioether bonds.[97] In the subsequent *in vitro* study, the cleavable complexes outperformed the stable ones with regard to their transfection efficiency. Another approach of a reducible polymeric micelle was reported by Liu et al.[98] In their approach, Boltorn H40 was coupled to a linear amphiphilic polymer chain consisting of PLA connected to hydrophilic polyphosphate through a disulfide bridge. Furthermore, the supramolecular encapsulation of DOX with this amphiphile showed significantly increased release *in vitro* under reductive conditions. These results could be confirmed on HeLa cells when treated with glutathione monoethyl ester.

There are many pH-gradients known in the human body. The most exploited one for many years has been the different parts of the gastro-intestinal system in which acidic

pH values are present as well as slightly basic ones (pH 2 – pH 8).[99] In skin, the pH gradient starts on the surface (the so-called acid mantle) at a pH around 5 and approximates the systemic 7.4 in deeper skin layers.[100] In pathological states, the pH value can deviate. In cancerous tissue the pH value is decreased to pH 6 and below,[101] similar values can be measured in inflamed tissue.[102] Even on a microscopic level, in different cell compartments, the pH value can vary significantly. After endosomal uptake, the newly formed vesicle is acidified, leading to low pH values in the early endosome (pH 5-6), and even lower ones in the late endosome (pH 4-5).[103] Depending on the application, these gradients can be used for a tissue-specific release. Li et al. reported a polymeric micelle to deliver a platinum-based anti-cancer agent into tumors.[104] A platinum compound was coupled to a PAMAM dendrimer to which amphiphilic chains was attached. While the hydrophilic part consisted of PEG, the hydrophobic part contained tertiary amine groups, which could be protonated. At neutral pH, the amphiphiles assembled into a supramolecular aggregate, that could passively target tumor tissue because of the EPR effect. Upon pH change (e.g., by entering the target tissue) the tertiary amine groups were protonated and the aggregate disassembled due to coulomb repulsion. Interestingly, this type of architecture showed a very sharp transition from the assembled to the disassembled state within a change of pH of only 0.1 to 0.2. In *in vivo* studies with multicellular spheroids and BxPC-3 tumor models these nanoassemblies showed improved activity as compared to their non-switching counterparts. Calderón et al. reported a hPG/PEG CS system with DOX coupled to the core via a hydrazide linker.[105] pH-dependent liberation of DOX was demonstrated *in vitro* and when applied to a ovarian carcinoma A2780 xenograft model, the anti-cancer activity exceeded the one of free DOX.

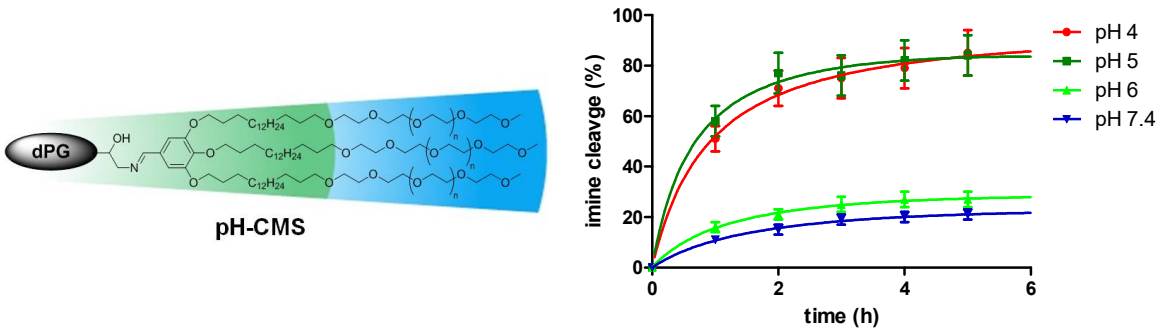

Figure 13. Chemical structure of a pH-cleavable CMS nanocarrier (left). Cleavage kinetics of the pH sensitive imine bond at different pH values. See text for more details. Reproduced with permission from Elsevier.[106]

A pH-responsive CMS nanocarrier was presented by Fleige et al. in 2014.[106] Into the parent CMS architecture, an imine linker was introduced between core and inner shell. While particle showed only slow degradation under pH 7.4 and 6, accelerated decomposition took place at pH values of 5 and 4 (see Figure 13). And when applied to A549 lung cancer cells *in vitro*, DOX loaded to pH-cleavable nanocarriers exhibited a higher toxicity compared to their DOX-loaded non-cleavable counterparts.

The presence of enzymes can be exploited by providing a specific substrate, which involves in many cases its cleavage, namely, of an ester or an amide bond. This means usually the (partial) degradation of the carrier scaffold or the cleavage of the linker structure that connects the pharmacophore to the carrier. Mao and Gan prepared polymeric micelles with a PG-b-PCL-copolymer to which pyrene could be loaded.[107] These micelles were then used to examine the degradation of this copolymer by a lipase. Even though the degradable polyester core was shielded by non-degradable PEG chains, the authors observed a decrease in fluorescence intensity of the cargo pyrene. These results indicated that by the dynamic exchange the polymeric amphiphiles become accessible and degradable and thus a triggered release can be facilitated. In a prodrug approach, Calderón et al. coupled DOX and methotrexate, respectively, to a hPG backbone via two different peptide substrates for the enzyme cathepsin B.[108] The conjugates were proven to be non-toxic and the incubation with cathepsin B led to the release of the drug. Khandare et al. prepared paclitaxel prodrugs by coupling it to a PAMAM dendrimer through two ester bonds and a flexible PEG-linker.[109] Incubation with an enzyme led to liberation of the original drug and when the constructs were applied on ovarian carcinoma cells, they showed an increased toxicity compared to the free drug, indicating uptake and cleavage of the conjugate.

1.5 Dermal Drug-Delivery

Skin is the most accessible organ of the body and thus has great potential as a drug delivery route.[110] But it’s also the reason why nature has fortified its natural barriers to prevent the entrance of xenobiotics. Aiming at dermal drug delivery, the goal is to overcome the natural barriers, that are closely related to the skin’s structure, with least possible irritation. The skin comprises of three major layered parts: hypodermis, dermis, and epidermis.[111] The uppermost layer, the epidermis, can again be subdivided into four different layers, the stratum basale, stratum spinosum, stratum

granulosum, which is only covered by the stratum corneum. While the dermis is vascularized, the epidermis does not contain any blood vessels. Its major part consists of keratinocytes together with a low percentage of melanocytes, which are responsible for the production of UV-protecting melanin and Langerhans cells, the outposts of the immune system in skin. As dermal regeneration is a dynamic process involving the migration of skin cells, the keratinization increases with the different layers, to finally yield dead terminally differentiated corneocytes forming the stratum corneum (SC).

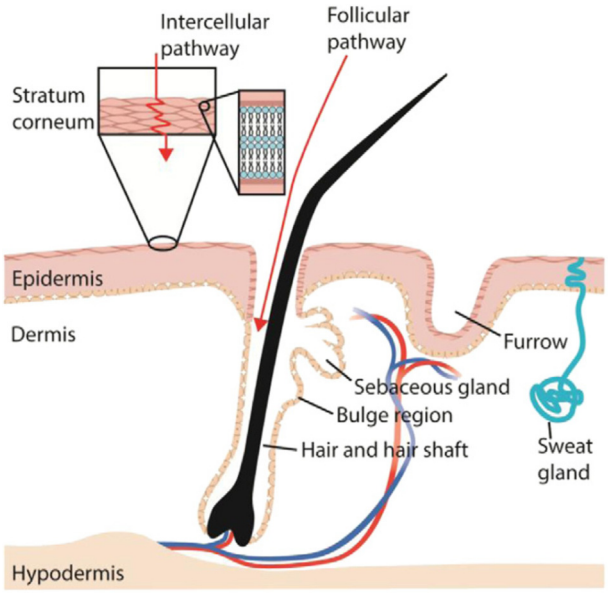

Figure 14: Schematic depiction of the skin's layered structure and the two major penetration pathways for nanomedicines. Reproduced with permission from Elsevier.[110]

This outermost layer is the first physical barrier of the skin which needs to be overcome for successful drug delivery. It comprises flattened, hexagonally shaped corneocytes containing fibrous keratin which are surrounded by extracellular lipids. It is commonly described as brick and mortar model.[112] In addition to this basic description, corneodesmosomes and anchoring structures are important structural features that contribute to mechanical stability. In principle, there are three different pathways through skin of which two lead through the SC in a more or less direct manner.[113] The intracellular pathway describes the way through the SC passing through the dead corneocytes, while the more important intercellular one leads around them. In addition, there is a third, follicular pathway. Hair follicles are shunts through the skin barrier and thus pose an attractive drug delivery route. The follicles roots deeply into the dermis, but in addition to a hair growing out of the follicle, the sebaceous gland excretes sebum, which impedes the entry of nanoparticles.

While there is a “500 Da rule” for dissolved small molecule to cross the skin barrier,[114,115] the situation is much more complicated for nanoparticles. Whether and how deep a nanotransporter penetrates skin and by which mechanism is a matter of a multitude of factors. Such factors include deformability, charge and shape, but the most important factor is size.[113] A multitude of nanoparticles of different sizes and materials was tested for skin penetration. While particles like liposomes, which are comprised of small molecules, usually disintegrated into their building blocks while entering the SC, polymeric and inorganic particles mostly only penetrated the top part of the SC. The hair follicle, however, was penetrated by nanoparticles of various sizes. Vogt et al. reported the increased uptake into hair follicles and Langerhans cells of 40 nm-sized particles compared to particles with a diameter of 750 and 1500 nm.[116] In contrast to that, a different size dependence was observed by Patzelt et al. They applied PLGA and SiO_2 particles of a size from 122 to 1000 nm to porcine skin using a massager for three minutes.[117] In the subsequent analysis, the particle showed different penetration depths with a maximum at around 640 nm particle size. This optimum was attributed to the combination of vibrational massage and the hair’s sawtooth-like surface structure, and postulated a “ratchet”-like mechanism, which was also described in theoretic models.[118] In diseased skin, penetration of nanoparticles can be different from the normal state. Psoriasis and atopic dermatitis alter the differentiation of the corneocytes, lipid composition, and organization. In general, these changes lead to an impaired barrier function and thus to increased penetration of nanoparticles.[119,120]

There are several types of polymeric nanocarriers that have been used for the transport of biologically active agents. Amphiphilic polymeric architectures can enhance the penetration of a loaded guest molecule. Xing et al. reported nanoparticles based on an amphiphilic graft copolymer which were loaded with tetrahydropalmatine (THP). In an evaluation *in vitro* on a Franz cell setup, the particles did not only transport THP through the skin but also penetrated the skin themselves.[121] In a similar setup, Conte el al. used a PEG-co-PCL block copolymer for the encapsulation and penetration enhancement of a Zn-phthalocyanine (ZnPc). While without β-CD, the ZnPc penetrated skin only poorly, the addition of a β-cyclodextrin could enhance skin penetration depth significantly. A similar type of amphiphilic polymeric structure, the CMS nanocarriers, were also used to enhance the penetration of Nile red *ex vivo*.

Küchler et al. applied dye-loaded CMS nanotransporters on pig skin *ex vivo* and found their penetration-enhancing effect superior over the one of solid lipid nanoparticles.[85] In a subsequent study,[122] the same Nile red-loaded nanocarrier and an unloaded dye-labeled analog were compared regarding their penetration on normal and stripped skin human skin *ex vivo* (see Figure 15). While Nile red penetrated rapidly even after 6 h incubation time in deep skin layers, the nanocarrier could only be found in the SC after this period. However, penetration of the nanocarrier could be enhanced by tape-stripping or an extended incubation time. These results showed that CMS nanocarriers are promising candidates for the dermal drug delivery of small hydrophobic drugs.

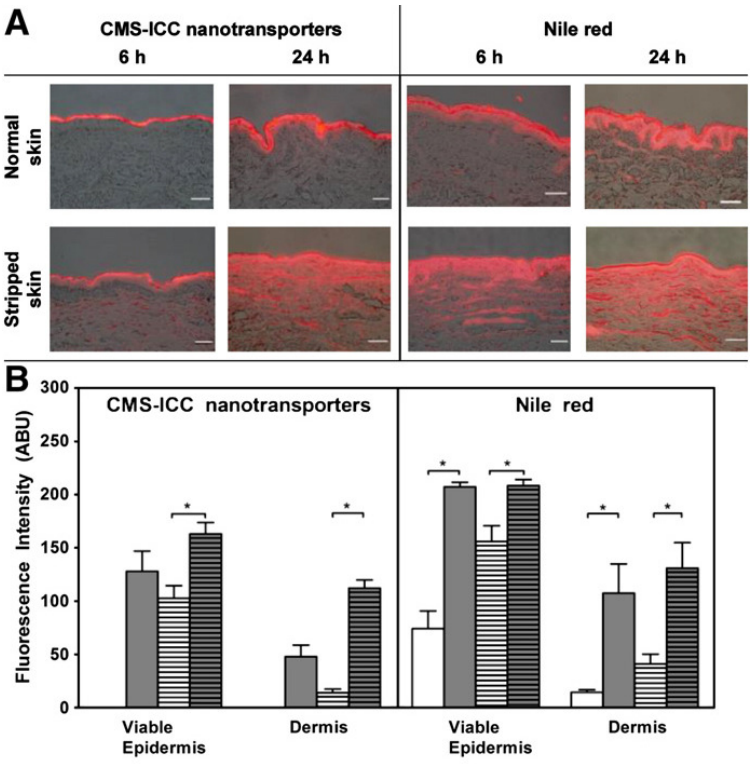

Figure 15. Penetration of ICC-labeled CMS nanocarriers and NR (0.004%, loaded into CMS nanotransporters) into normal (white bars) and tape-stripped (grey bars) human skin. Incubation times were 6 h (open columns) and 24 h (striped columns). A. Overlay images of fluorescence and bright field microscopy. B. Quantification of fluorescence intensity into arbitrary brightness units (ABU) in the different skin layers ± standard error of the mean, n = 3, scale bar 100 µm, p ≤ 0.05, reprinted with permission from Elsevier.*[122]

As amphiphilic nanocarriers are more suitable for hydrophobic small drugs, bigger and more hydrophilic structures are the obvious choice for biomolecules like proteins or DNA. In a study by Witting et al. hPG was crosslinked with PNIPAM to yield thermoresponsive nanocarriers with a trigger point at 35 °C.[123] Exceeding this trigger point, the nanogels released 93% of the loaded protein. Subsequent skin penetration experiments on barrier-deficient skin resulted in the successful delivery of transglutaminase 1 into skin, while no penetration of the nanogel was detected.

2 Scientific Goals

CMS nanocarriers are a versatile platform for the solubilization of a variety of compounds and can be used for the delivery of a multitude of pharmacophores to certain sites in the human body. Drug targeting to tumors, has been facilitated as well as penetration enhancement into skin. To improve the current approaches and tackle unsolved problems, novel CMS architectures have to be explored. This work can be subdivided into two parts. The first one will deal with biocompatible and biodegradable CMS-nanocarriers for the encapsulation of hydrophobic drugs and the enhanced penetration into skin. In the second part, a CMS nanoarchitecture will be designed for the binding and pH-dependent release of a small cationic analgesic.

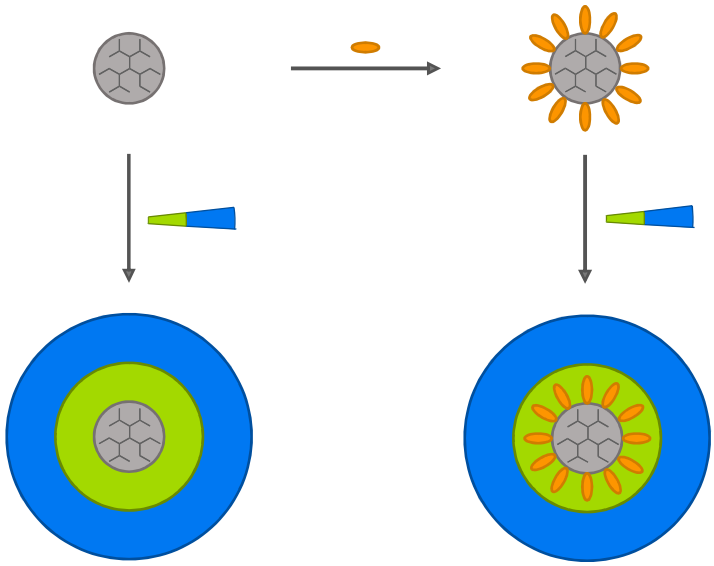

Figure 16. Schematic illustration of the synthetic strategies. grey circle = hPG core, green/blue wedge = amphihilic double shell, orange oval = anchor molecule.

The skin is a strong barrier that has to be overcome in order to improve dermal delivery for an efficient treatment. CMS nanocarriers have become promising candidates to enhance the penetration of hydrophobic drugs. To improve this architecture, crucial issues have to be addressed, such as ease of synthesis, degradability, nontoxicity of building blocks, and controlled release. In addition, it is important to investigate the drug-carrier interaction. To this point, it is known that hydrophobic interactions play a key role in the encapsulation process. However, only little attention was paid to aspects like chain length, branching, and the type of bond used to attach the amphiphilic double shell. Additional factors are defined by the drug itself. Hydrophobic drugs can vary strongly with respect to polarity, size and rigidity, which can influence the interaction with a DDS. To investigate this, two structurally different hydrophobic

anti-inflammatory drugs, which are important for the treatment of auto-inflammatory skin diseases, will be investigated regarding their loading into architectural various CMS nanotransporters.

Degradability is a crucial to avoid accumulation in the tissue during *in vivo* applications but can also be controlled release mechanism. Hence, the goal is to redesign the synthesis to yield biodegradable, ester-based carriers. This strategy has two advantages, it reduces the number of synthetic steps and avoids the formerly used, potentially toxic building block hPG-NH_2. The final products will then be tested regarding their degradability both *in vitro* and *in vivo* and with respect to the controlled release of a hydrophobic drug. Toxicity of not only of the CMS architectures but also of their building blocks will also be determined. Finally, the penetration of the carriers and the guest molecules will be quantified on different skin models, including excised human skin, an inflammatory skin model, and murine oral mucosa.

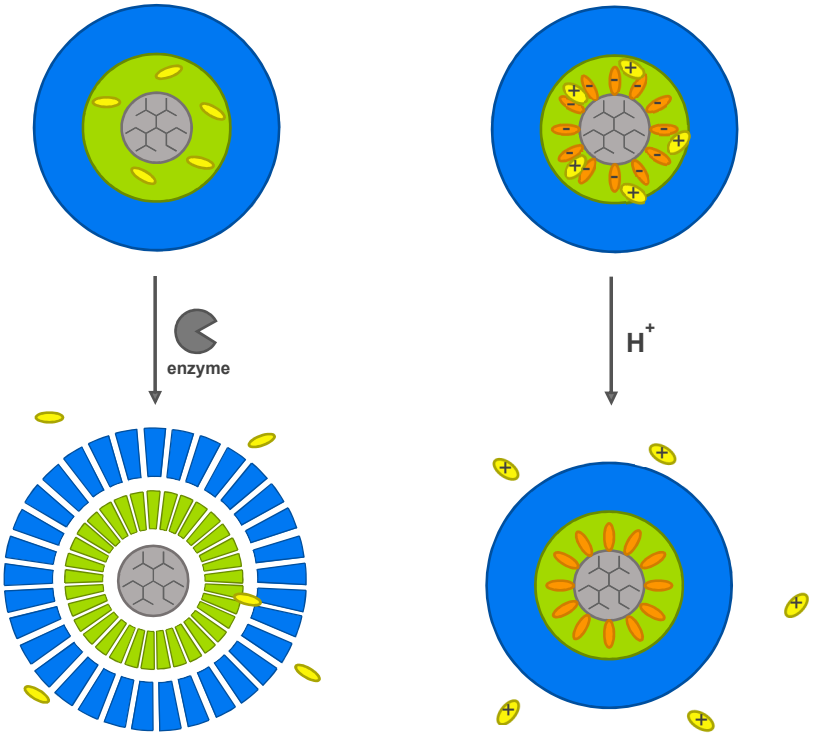

Figure 17. Different release mechanisms for the two CMS nanocarriers. Enzymatic degradation (left) and protonation of the anchor group (right)

U 50,488H is a strong analgesic with potential application in post-operative pain treatment, which is cationic under physiological conditions. However, there are severe side effects which only occur when the drug crosses the blood brain barrier. After an operation, the tissue is inflamed and thus exhibits a lower pH. The goal is to use these conditions to design a functionalized nanocarrier for the transport and pH-dependent

release of U 50,488H. To achieve this, the architecture of the CMS nanocarrier will be extended by an anchor moiety, which can bind U 50,488H via ionic interaction, π-π stacking and hydrogen bonding. After synthesis and characterization, the drug-loading properties of the nanocarriers will be determined. The release-kinetics of U 50,488H from the carrier will be measured under various conditions to quantify the retention effect. Finally, a selected carrier will be tested in a rat model for *in vivo* performance.

3 Publications and Manuscripts

3.1 Biodegradable Core–Multishell Nanocarriers: Influence of Inner Shell Structure on the Encapsulation Behavior of Dexamethasone and Tacrolimus

This chapter was published in:

Michael L. Unbehauen, Emanuel Fleige, Florian Paulus, Brigitta Schemmer, Stefan Mecking, Sam Dylan Moré and Rainer Haag, Polymers 2017, 9, 316.

DOI: https://doi.org/10.3390/POLYM9080316

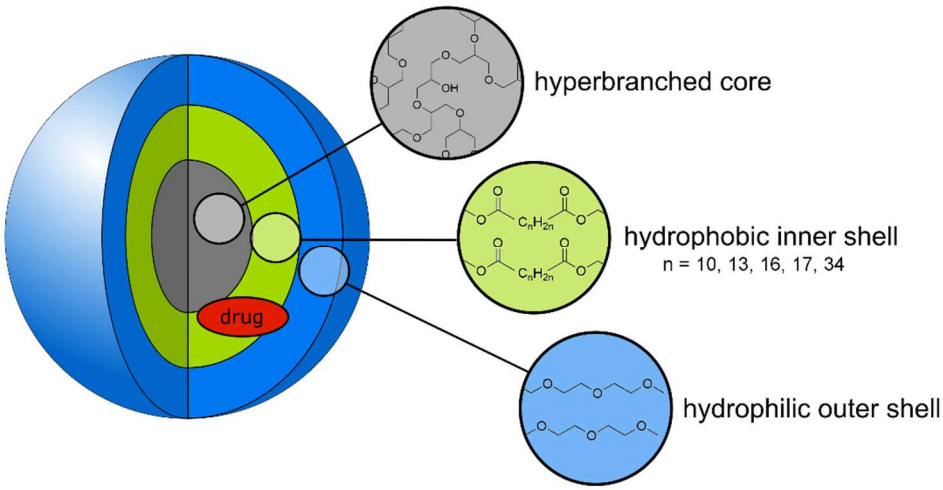

Author contributions:

- Development of synthetic strategy
- Synthesis of CMS nanocarriers CMS-E18, CMS-E19, CMS-E18b, CMS-A18 and their double-shell building blocks
- DLS and loading capacity measurements
- Determination of the kinetics of degradation and release
- Preparation of the manuscript

polymers

MDPI

Article

Biodegradable Core–Multishell Nanocarriers: Influence of Inner Shell Structure on the Encapsulation Behavior of Dexamethasone and Tacrolimus

Michael L. Unbehauen [1], Emanuel Fleige [1,2], Florian Paulus [1,2], Brigitta Schemmer [3], Stefan Mecking [3], Sam Dylan Moré [2] and Rainer Haag [1,*]

1 Freie Universität Berlin, Institute for Chemistry and Biochemistry, Takustraße 3, 14195 Berlin, Germany; m.unbehauen@fu-berlin.de (M.L.U.); emafl@zedat.fu-berlin.de (E.F.); florian.paulus@fu-berlin.de (F.P.)
2 DendroPharm GmbH, Arnimallee 14, 14195 Berlin, Germany; sam.more@dendropharm.de
3 Chemical Materials Science, Department of Chemistry, University of Konstanz, Universitätsstraße 10, 78467 Konstanz, Germany; brigitta.schemmer@uni.kn (B.S.); stefan.mecking@uni-konstanz.de (S.M.)
* Correspondence: haag@chemie.fu-berlin.de; Tel.: +49-308-385-2633

Received: 21 June 2017; Accepted: 25 July 2017; Published: 29 July 2017

Abstract: We here present the synthesis and characterization of a set of biodegradable core–multishell (CMS) nanocarriers. The CMS nanocarrier structure consists of hyperbranched polyglycerol (hPG) as core material, a hydrophobic (12, 15, 18, 19, and 36 C-atoms) inner and a polyethylene glycol monomethyl ether (mPEG) outer shell that were conjugated by ester bonds only to reduce the toxicity of metabolites. The loading capacities (LC) of the drugs, dexamethasone and tacrolimus, and the aggregate formation, phase transitions, and degradation kinetics were determined. The intermediate inner shell length (C15) system had the best overall performance with good LCs for both drugs as well as a promising degradation and release kinetics, which are of interest for dermal delivery.

Keywords: biodegradable CMS nanocarrier; drug delivery; dendritic polymers; dexamethasone; tacrolimus

1. Introduction

Cutaneous drug delivery is the method of choice when skin is the target and systemic side effects are to be avoided. This is especially the case in inflammatory skin diseases such as psoriasis and atopic dermatitis. The drugs, e.g., the commonly used dexamethasone and tacrolimus, must penetrate the skin first, which is the body's natural barrier against xenobiotics. Especially the outermost layer, the stratum corneum, has to be overcome to reach the target, namely, the skin's viable layers. Amphiphiles, among other penetration enhancers, are extensively used to facilitate a deeper penetration [1]. The application of nanoparticles, which have attracted much attention in recent years [2], has been widely explored. A nanoparticle can either consist of only the drug or be a carrier particle that contains the respective agents. The nanoparticles are classified according to their size, shape, and charge and are categorized into hard and soft, biological, organic, and inorganic particles. The skin offers different pathways for various types of nanoparticles that address one or more of the transdermal pathways, the intracellular, intercellular, or the follicular pathway, and also target the sebaceous gland [3]. Particulate formulation has been shown to enhance both the uptake of drugs into skin in general [4,5] but also specifically into hair follicles in a size-dependent manner [6,7]. Some of the polymeric particles that are reported in the literature contain esters or are ester-based (e.g., PCL [8], PLA [6], PLGA [7]) and thus are principally biodegradable.

A more sophisticated structure is the so-called core–multishell (CMS) nanocarrier that extends the idea of the unimolecular micelle to the parent structure of a unimolecular liposome [9–11]. While a unimolecular micelle consists of simple, usually hydrophilic polymeric chains anchored to a dendritic core [12], the CMS nanocarrier is a unimolecular structure that has a branched core-unit with amphiphilic polymeric chains attached to it, which at least consist of one hydrophilic and one hydrophobic block (see Figure 1). Frequently used core structures are the polyester Boltorn® H40 [13,14], poly (ethyleneimine) (PEI) and the highly hydrophilic hyperbranched polyglycerolamine (hPG-NH_2) [15,16]. Initially designed as a unimolecular liposome, the CMS nanotransporter has been reported by our group for the transport of both hydrophilic and lipophilic guest molecules [11,15]. The CMS nanocarrier can solubilize hydrophobic guest molecules in a hydrophilic environment and vice versa [16]. In contrast to other drug delivery systems (DDS), the mode of solubilization is physical entrapment upon which larger aggregates are formed. The CMS nanocarrier and its differently functionalized derivatives have been successfully used for the transport of the fluorescence dye ITCC in a tumor xenograft model as well as the penetration enhancement of the model drug Nile Red into skin [16,17]. Their aggregation phenomena and host–guest interactions have been studied both experimentally and theoretically [18,19].

The long-term toxicity of the polymeric DDS is an important issue when it comes to in vivo applications. Not only the polymer assemblies but also their degradation products have to be taken into consideration. The usage of polyamines can be especially problematic: Their polycationic character enables interaction with the positively charged cellular membranes and can be a source of cytotoxicity [20]. In the case of hPG–NH_2, another drawback is the synthetic effort. Three synthetic steps are necessary to convert the hyperbranched glycerol (hPG) to its amino-functionalized derivative [21].

Complementary to a previous biological study [22], here we present esterification as a promising alternative to amide formation for the synthesis of the CMS nanocarriers. Furthermore, the influence of different chain length, branching of inner shell, the type of chemical bond on melting point, and drug loading behavior of dexamethasone and tacrolimus are investigated.

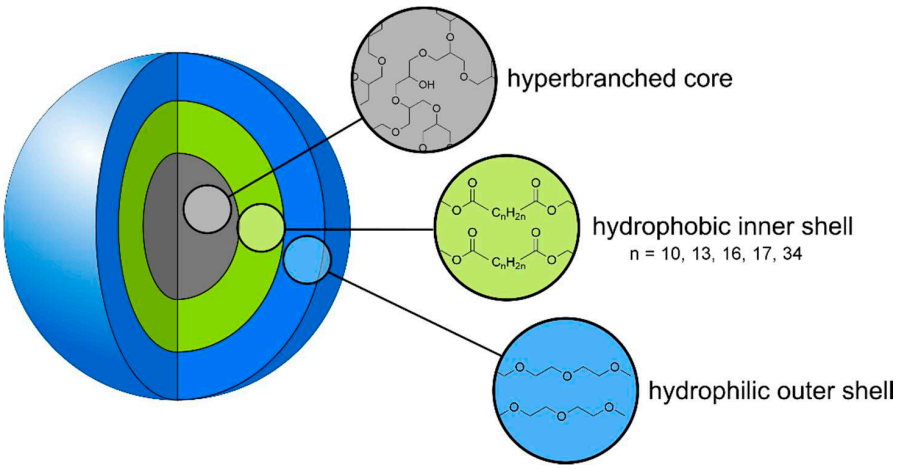

Figure 1. Structure of an ester-based CMS nanocarrier.

2. Materials and Methods

All chemicals were used as bought without any further purification. Polyethylene glycol monomethyl ether (mPEG) 350 was bought from Sigma-Aldrich, Munich, Germany. 1,18-Octadecandioic acid was a kind gift from Cognis, Monheim am Rhein, Germany. 1,19-nonadecanedioic acid was received as the dimethyl ester from the Mecking group, Konstanz, Germany [23]. The branched C18b-diacid was a gift from Cognis (see Scheme S1 for composition

and purification). 1,12-Dodecandioic acid was bought from Sigma Aldrich, St. Louis, MI, USA and 1,15-pentadecandioic acid was bought from ToniChemPharma (Huizhou, China). hPG and CMS-A18 were produced by previously published methods [21,24].

Methanol was bought from Sigma-Aldrich; dry pyridine was bought from Acros, Geel, Belgium and stored over calcium hydride (Acros). Dry DCM was taken from solvent purification system (SPS-800) by MBRAUN (Stratham, NH, USA) and stored over a molecular sieve (4 Å, Roth).

2.1. Nuclear Magnetic Resonance (NMR)

NMR spectra were recorded either on a Jeol Eclipse 500 MHz (Tokyo, Japan) or a Bruker AVANCE III 700 MHz spectrometer (Billerica, MA, USA). Proton and carbon NMR were recorded in ppm and were referenced to the indicated solvents [25]. NMR data were reported including: chemical shift, multiplicity (s = singlet, d = doublet, t = triplet, m = multiplet), integration, and coupling constants (s) in Hertz (Hz). Multiplets (m) were reported over the range (ppm) in which they appear in the spectrum. All spectra were recorded at 300 K.

2.2. Infrared (IR) Spectroscopy

IR spectra were recorded on a Jasco FT/IR 4100LE spectrometer (Groß-Umstadt, Germany) equipped with a MIRacleTM single reflection ATR device from PIKE Technologies (Fitchburg, WI, USA). Samples were directly placed on the ATR crystal. Data recording and analysis was done with Spectra Manager® II software from Jasco.

2.3. Dynamic Light Scattering (DLS)

For the determination of hydrodynamic sizes, dynamic light scattering (DLS) measurements were performed on a Malvern Zetasizer Nano (Herrenberg, Germany) equipped with a laser at 532 nm using backscattering mode (detector angle 173°). The samples were filtered through 0.45 µm regenerated cellulose syringe filters prior to DLS measurement and 100 µL of the resulting solution added to a disposable micro-cuvette. Autocorrelation functions were analyzed using Zetasizer DTS software (Malvern, Herrenberg, Germany) to determine the size distribution by intensity or number. The fraction (%) indicates the proportion of measured size relative to the total signal scattered by the CMS nanocarriers. Measurements were performed at 25 °C if not stated otherwise.

2.4. Gel Permeation Chromatography

A Shimadzu (Kyoto, Japan) liquid chromatography (LC) system was employed for the gel permeation chromatography (GPC) measurements. Three PolarSil columns (PSS Polymer Standards Service GmbH, Germany; PolarSil 8 × 300 mm, 100 Å, 1000 Å, 3000 Å with 5 µm particle size) and a refractive index detector (RI) were used to separate and analyze polymer samples. As the mobile phase DMF (0.3 wt % LiBr and 0.6 wt % acetic acid) was used at a flow rate of 1 mL·min^{-1}. Columns and RI detector were heated to 40 °C. The system was calibrated against polystyrene calibration standards (PSS, Germany). Samples were measured at a concentration of 10 mg·mL^{-1}. LC solution software from Shimadzu was used for data analysis.

2.5. Film Encapsulation Method

The film uptake method was chosen for the encapsulation procedure. To form a film, 50 wt % of the guest compound (dexamethasone or tacrolimus) was dissolved in a vial and the solvent removed on a rotavap. A stock solution of the respective CMS nanocarrier (5 mg·mL^{-1}) was filled onto the film and the suspension stirred for 22 h at room temperature. Excess guest was removed via filtration through a 450 nm RC syringe filter. The same procedure was carried out at 60 °C for the CMS-E19 nanocarrier, which was poorly soluble at low temperatures.

2.6. HPLC Analysis

The guest concentration was determined via high performance liquid chromatography (HPLC, Phenomenex Gemini, Torrance, CA, USA, C18, 5 µm 110 Å, 250 mm × 6.4 mm, flow 1 mL·min^{-1}, 210 nm, 40% acetonitrile/H_2O for dexamethasone, acetonitrile for tacrolimus) using a UV detector set to λ = 210 nm. For the preparation of the sample, the samples were diluted with acetonitrile (dexamethasone) or lyophilized and redissolved in acetonitrile (tacrolimus).

2.7. Determination of Enzymatic Activity

The enzymatic activity of *Rhizomucor miehei* lipase was determined photometrically similar to a previously published method [26]. First, 5–10 µL of the diluted enzyme solution was added to a solution of 1 mM 4-nitrophenyl acetate in PBS (1% acetonitrile, total volume 1 mL). After 1 h stirring at 200 RPM and 32 °C, the concentration of the reaction product 4-nitrophenol was determined photometrically using a spectrophotometer and the extinction coefficient of 4-nitrophenol (ε = 11.9 × 10^3 M^{-1}·cm^{-1}, λ = 400 nm). A sample without enzyme was used to deduct the fraction of thermal hydrolysis. One unit of enzymatic activity equals the release of 1 µmol 4-nitrophenol per minute.

2.8. Enzymatic Degradation

To determine the rate of enzymatic degradation, a solution of CMS nanocarrier (5 mg·mL^{-1}) in PBS was prepared and lipase from Rhizomucor miehei (8 mU·mg^{-1} polymer) was added. The solutions were stirred with a small stir bar at 200 RPM at 32 °C. Samples were taken at different time points, lyophilized, redissolved in DMSO-d_6 and analyzed via NMR. Due to the high consumption of material, the experiment was only performed once.

2.9. Release by Enzymatic Degradation

To measure the release of the drug from an enzymatically degraded carrier, a solution of dexamethasone-loaded CMS nanocarrier in PBS was prepared (10 mg mL^{-1} polymer), Rhizomucor miehei lipase (8 mU·mg^{-1} polymer) added (or not added in the case if the untreated control (UC)) and the solution stirred at 200 RPM. At different time points, the solution was centrifuged for 10 min at 4000 RPM (Heraeus Biofuge Primo), the supernatant sampled and stirring was continued. Samples were either diluted with acetonitrile before measurement with HPLC to match the eluent.

2.10. Synthesis

1,19-Nonadecandioic Acid

Following a previously published procedure [23], dimethyl-1,19-nonadecanedioate (854.9 mg, 2.4 mmol) was suspended in 6.4 mL methanol and the suspension heated to 70 °C (oil bath). After dissolution, a solution of 1.8 g (31.4 mmol) KOH in 6.4 mL Methanol was added dropwise and the solution was stirred overnight at 70 °C. The methanol was distilled off and the residue dissolved in water. Then it was acidified via the addition of 3 M HCl to a pH of 1. The precipitate was filtered off with a glass frit, washed with water, and dried in the air stream of the pump. The product could be isolated as 764 mg (2.3 mmol) of a colorless solid (yield 97%).

^{1}H NMR: (DMSO-d_6, 500 MHz, TMS): δ 2.17 (t, 2H, *J* = 7.4 Hz, 4H, HOOC–CH_2–); 1.51–1.43 (m, 4H, HOOC–CH$_2$–CH_2–); 1.28–1.20 (br s, 26H, –CH$_2$– backbone). ^{13}C NMR: (DMSO-d_6, 125 MHz, TMS): δ 174.42 (HOOC–CH$_2$–), 33.66 (HOOC–CH$_2$–), 29.03–28.54 (HOOC–CH$_2$–CH$_2$–), 24.49 (–CH$_2$– backbone).

2.11. Double-Shell Building Blocks

2.11.1. C12-mPEG350

In a three-neck flask equipped with a gas inlet, thermometer with quick fit, and septum, a mixture of mPEG350 (0.3 mol, 1 equiv.) with dodecanedioic acid (C12, 0.9 mol, 3 equiv.) was stirred under high vacuum and heated to 120 °C. The mixture was kept at this temperature for at least 1.5 h until a clear melt was obtained. The temperature was then raised to 180 °C and stirred for an additional 4.5 h. The reaction mixture was kept under vacuum and allowed to cool to 120 °C. While still a melt, the hot reaction mixture was transferred to a beaker and cooled to room temperature. The still warm waxy solid was chopped, 2 L of methylene chloride added, and the resulting mixture vigorously stirred until a near homogeneous suspension was formed. The suspension was filtered and the filtrate concentrated to a final volume of 600 mL by rotary evaporation. The solution was kept a 5 °C for 18 h. Precipitated excess C15 was removed by filtration. The remaining filtrate was concentrated by rotary evaporation and subsequently dried under high vacuum to yield a colorless wax (69%) of C12-mPEG350.

^{1}H NMR (500 MHz, methanol-d_4, TMS): δ (ppm) = 4.22–4.18 (m, 2H, –CH_2–OCO–), 3.75–3.50 (m, 30H, mPEG backbone), 3.36 (s, 3H, –O–CH_3), 2.33 (t, 2H, J = 7.4 Hz, ROOC–CH_2–CH_2–), 2.28 (t, 2H, J = 7.4 Hz, HOOC–CH_2–CH_2–), 1.65–1.55 (m, 4H, –CO–CH_2–CH_2–), 1.37–1.20 (m, 12H, –CH_2–(CH_2)$_6$–CH_2–). ^{13}C NMR (125 MHz, methanol-d_4, TMS): δ (ppm) = 177.4, 175.2, 72.9, 71.7–71.3, 70.3, 70.1, 64.5, 64.3, 59.1, 59.1, 34.9, 34.9, 30.7, −30.1, 26.0, 26.0. IR (cm^{-1}): 2923, 2856, 1732, 1456, 1349, 1247, 1099, 1040, 946, 849, 724. GPC: M_n = 680 g·mol^{-1}, M_w = 750 g·mol^{-1}, PDI = 1.10.

2.11.2. C15-mPEG350

C15-mPEG350 was synthesized in analogy to C12-mPEG350. The reaction of mPEG350 (0.3 mol, 1 equiv.) and 1,15-pentadecanedioic acid (0.9 mol, 3 equiv.) resulted in C15-mPEG350 as a pale-yellow wax (68% yield).

^{1}H NMR (500 MHz, methanol-d_4, TMS): δ (ppm) = 4.22–4.18 (m, 2H, –CH_2–OCO–), 3.75–3.50 (m, 30H, mPEG backbone), 3.36 (s, 3H, –O–CH_3), 2.33 (t, 2H, J = 7.4 Hz, ROOC–CH_2–CH_2–), 2.28 (t, 2H, J = 7.4 Hz, HOOC–CH_2–CH_2–), 1.65–1.55 (m, 4H, –CO–CH_2–CH_2–), 1.37–1.20 (m, 18H, –CH_2–(CH_2)$_9$–CH_2–). ^{13}C NMR (125 MHz, methanol-d_4, TMS): δ (ppm) = 177.5, 175.3, 72.9, 71.6–71.5, 71.3, 70.1, 64.5, 59.1, 34.9, 34.9, 30.7, −30.1, 26.0, 26.0. IR (cm^{-1}): 2922, 2854, 1733, 1456, 1349, 1248, 1099, 1040, 946, 850, 723. GPC: M_n = 680 g·mol^{-1}, M_w = 735 g·mol^{-1}, PDI = 1.08.

2.11.3. C18-mPEG350

Similar to an already published method [15], 14.9 g (42.7 mmol) methoxy-poly(ethylene glycol) (mPEG) 350 (dried overnight at 70 °C under low pressure (5×10^{-2} mbar) and 47.7 g (15.2 mmol) 1,18-octadecanedioic acid were added without solvent into a Schlenk flask. The reaction mixture was heated up to 185 °C and the reaction mixture was stirred vigorously for 3 h under vacuum (5×10^{-2} mbar). After 3 h, a sample was taken and submitted for NMR, the mixture was allowed to cool down to 140 °C, and a reflux condenser was installed. Then, 300 mL toluene was added into the flask. While still stirring, the reaction mixture was slowly allowed to cool down to 0 °C. The resulting suspension was filtrated and the white residue was washed with 300 mL of cold (0 °C) toluene. The filtrate and washings were combined and concentrated by rotary evaporation in vacuo and the remaining solvent removed in vacuo at 50 °C. Of the pre-purified product (19.8 g, 72% yield), 5 g were purified via HPLC (Phenomenex Gemini, C18, 5 µm, 110A, 250 mm × 21.2 mm, flow 20 mL min^{-1}, 210 nm, 95% MeOH/H_2O) to yield 3.9 g of a white wax (yield 56%).

^{1}H NMR (700 MHz, methanol-d_4, TMS): δ (ppm) = 4.21 (m, 2H, –CH_2–OOC–), 3.71–3.52 (m, 28.4H, mPEG backbone), 3.36 (s, 3H, –O–CH_3), 2.34 (t, 2H, J = 7.4 Hz, 2H, R–OOC–CH_2–CH_2–), 2.28 (t, 2H, J = 7.4 Hz, 2H, –HOOC–CH_2–CH_2–), 1.65–1.54 (m, 4H, –OOC–CH_2–CH_2–), 1.38–1.25 (br s, 24H,

–CH_2–(CH_2)$_{12}$–CH_2–). ^{13}C NMR (176 MHz, methanol-d_4, TMS): δ (ppm) = 177.57, 175.35, 72.96, 71.75–71.25, 70.15, 64.55, 35.00–34.90, 30.80–30.15, 26.12–26.00. IR (cm^{-1}): 2916, 2848, 1730, 1702, 1462, 1342, 1243, 1106, 954, 848, 729. GPC: M_n = 830 g·mol^{-1}, M_w = 920 g·mol^{-1}, *PDI* = 1.11.

2.11.4. C19-mPEG350

C19-mPEG350 was synthesized analog to C18-mPEG350. In total, 1.8 g (5.0 mmol) mPEG350 and 4.9 g (15.0 mmol) 1,19-nonadecanedioic acid led to 2.4 g (3.7 mmol) of the colorless solid product (74% yield).

^{1}H NMR (700 MHz, methanol-d_4, TMS): δ 4.21 (m, 2H, –CH_2–OOC–), 3.71–3.52 (m, 26.8H, mPEG backbone), 3.36 (s, 3H, –O–CH_3), 2.33 (t, 2H, *J* = 7.4 Hz, 2H, R–OOC–CH_2–CH_2–), 2.28 (t, 2H, *J* = 7.4 Hz, 2H, –HOOC–CH_2–CH_2–), 1.64–1.57 (m, 4H, –OOC–CH_2–CH_2–), 1–1.27 (br m, 26H, –CH_2–(CH_2)$_{12}$–CH_2–). ^{13}C NMR: (176 MHz, methanol-d_4, TMS): δ 177.58, 175.34, 72.97, 71.65–71.50, 71.37, 70.16, 64.56, 59.10, 34.99, 34.94, 30.85–30.15, 26.10, 26.03. IR (cm^{-1}): 2917, 2848, 1729, 1694, 1463, 1345, 1234, 1105, 961, 847, 730. GPC: M_n = 840 g·mol^{-1}, M_w = 920 g·mol^{-1}, *PDI* = 1.10.

2.11.5. C18b-mPEG750

8.5 g C18b-diacid (15.0 mmol) and 2.8 g mPEG750 (3.7 mmol) were added into a Schlenk flask and stirred at 60 °C for 30 min. Afterwards, the reaction mixture was heated to 180 °C and stirred under high vacuum (<0.5 × 10^{-2} mbar) for 3 h. After cooling down, the mixture was purified via column chromatography using the eluents chloroform/acetic acid (80:1), chloroform/methanol 20:1, and methanol, which yielded the product as 3.8 g of a yellow oil (yield 78%).

^{1}H NMR: (700 MHz, methanol-d_4, TMS): δ 6.85 (m, 0.4H, arom. –H), 4.21 (m, 2H, –CH_2–OOC–), 3.75–3.50 (m, 63.2H, mPEG backbone), 3.36 (s, 3H, –O–CH_3), 2.54 (m, 1.6H, benzyl–H), 2.33 (t, 2H, *J* = 7.1 Hz, 2H, R–OOC–CH_2–CH_2–), 2.28 (t, 2H, *J* = 7.1 Hz, 2H, HOOC–CH_2–CH_2–), 1.64–1.50 (m, 8.2H, –OOC–CH_2–CH_2– + –CH_2–CH_2–Ph), 1.5–1.1 (br s, 44.5H, aliph. backbone), 0.91 (m, 3H, –CH_2–CH_3). GPC: M_n = 1380 g mol^{-1}, M_w = 1610 g mol^{-1}, *PDI* = 1.17. ^{13}C NMR: (176 MHz, methanol-d_4, TMS): δ 177.50, 175.28, 72.98, 71.87–71.05, 70.17, 64.57, 59.11, 34.98, 33.08, 31.05–29.95, 26.12, 23.76, 14.52. IR (cm^{-1}): 2921, 2855, 1732, 1456, 1349, 1249, 1101, 947, 850, 722.

2.12. Nanocarriers

2.12.1. CMS-E12

To link the shell components with the hPG core (M_n = 9.9 kDa; M_w = 15.8 kDa), 141 g C12-mPEG350 (0.3 mol, 1 equiv.) were dissolved in 625 mL anhydrous methylene chloride in a three-necked flask equipped with a gas inlet and two septa. The solution was cooled down to 0 °C and 25.9 mL thionyl chloride (42.5 g, 0.4 mol, 1.5 equiv.) was added. One septum was then replaced with a reflux condenser connected to two washing flasks, the second of which was filled with sodium hydroxide solution. The reaction was refluxed for 4.5 h. Methylene chloride and the excess of thionyl chloride were removed by cryo-distillation, and the residue dried for a further 3 h under high vacuum. In the meantime, 26 g hPG (2.6 mmol) were dissolved in 530 mL dry pyridine. The resulting acid chloride was dissolved in 200 mL dry methylene chloride and added dropwise to the hPG solution. The reaction was stirred overnight and then quenched by the addition of methanol (1.48 mol). Solvents were then removed with a rotary evaporator. The crude product was purified with a Millipore bench scale tangential flow field filtration system, equipped with a 30 kDa·MW cut-off membrane and at least 250 mL of distilled water per gram CMS nanocarrier. The product was freeze-dried, which yielded 117 g of a clear viscous yellow oil of CMS-E12 (62%).

^{1}H NMR (500 MHz, DMSO-d_6, TMS): δ (ppm) = 4.09 (s, 2H, –CH_2–OCO–), 3.69–3.25 (m, 37H, mPEG repeating unit and hPG backbone), 3.23 (s, 3H, –O–CH_3), 2.25 (m, 4H, –CH_2–COO–), 1.49 (m, 4H,

–C*H*$_2$–CH$_2$–COO–), 1.22 (m, 12H, –(CH$_2$)$_6$–). ^{13}C NMR (125 MHz, DMSO-d$_6$, TMS): δ (ppm) = 172.7, 71.3, 69.9–69.6, 68.4, 63.0, 58.0, 33.4, 29.3–28.4, 24.5. IR (cm^{-1}): 3462, 2922, 2856, 1732, 1456, 1349, 1248, 1100, 948, 850, 723. GPC: M_n = 32,200 g·mol^{-1}, M_w = 42,200 g·mol^{-1}, *PDI* = 1.31.

2.12.2. CMS-E15

CMS-E15 was synthesized in analogy to CMS-E12. In total, 151 g (0.3 mol) C15-mPEG350 were reacted with 25.9 mL thionyl chloride (42.5 g, 0.4 mmol) and 26 g (2.6 mmol) hPG (M_n = 10.4 kDa; M_w = 16 kDa) to yield 138 g of a yellow to brown oil (79%).

^{1}H NMR (500 MHz, DMSO-d$_6$, TMS): δ (ppm) = 4.09 (s, 2H, –CH$_2$–OCO–), 3.69–3.25 (m, 30H, mPEG repeating unit and hPG backbone), 3.23 (s, 3H, –O–CH$_3$), 2.25 (m, 4H, –CH$_2$–COO–), 1.49 (m, 4H, –C*H*$_2$–CH$_2$–COO–), 1.21 (m, 18H, –(CH$_2$)$_9$–). ^{13}C NMR (125 MHz, DMSO-d$_6$, TMS): δ (ppm) = 172.7, 71.3, 69.9–69.6, 68.3, 63.0, 58.0, 33.4, 29.3–28.4, 24.5. IR (cm^{-1}): 3460, 2922, 2853, 1733, 1456, 1349, 1248, 1100, 949, 851, 722. GPC: M_n = 41,100 g·mol^{-1}, M_w = 59,100 g·mol^{-1}, *PDI* = 1.44.

2.12.3. CMS-E18

hPG (480 mg, 6.5 mmol OH groups, M_n = 8.1 kDa; M_w = 16.2 kDa) was dried by dissolving in 5 mL of anhydrous pyridine and evaporating the solvent. Then it was dissolved in 38 mL dry pyridine. C18-mPEG350 (1.7 mmol, 7.5 g, previously dried at 50 °C under vacuum <5 × 10^{-2} mbar overnight) in a three-neck flask (equipped with a reflux-condenser, an olive and a septum) was dissolved in 38 mL dry methylene chloride. At 0 °C, 1.27 mL thionyl chloride were added and after 10 min the temperature was increased to the boiling point of methylene chloride. After 2 h, the solvent was evaporated by cryo-distillation. At 0 °C, the intermediate was dissolved in dry pyridine and the solution was added dropwise to the solution of hPG. After stirring overnight, the solvent was distilled off and the crude product purified with dialysis (5 kDa, 3 × 3 L) and ultrafiltration (MWCO 30 kDa, methanol) yielding the product as a viscous, brownish oil (2.7 g, 78%).

^{1}H NMR (700 MHz, methanol-d$_4$, TMS): δ (ppm) = 4.21 (s, 2H, –CH$_2$–OCO–), 3.72–3.52 (m, 31.7H, mPEG repeating unit and hPG backbone), 3.36 (s, 3H, –O–CH$_3$), 2.34 (m, 4H, –OOC–CH$_2$–), 1.62 (m, 4H, –OOC–CH$_2$–C*H*$_2$–), 1.31 (m, 24H, –(CH$_2$)$_{12}$–). ^{13}C NMR (176 MHz, methanol-d$_4$, TMS): δ (ppm) = 175.0, 73.0, 71.6–71.4, 70.2, 64.6, 59.2, 35.0, 31.0–30.4, 26.2. IR (cm^{-1}): 3445, 2922, 2852, 1733, 1456, 1349, 1248, 1103, 949, 851, 722. GPC: M_n = 34,900 g·mol^{-1}, M_w = 49,200 g·mol^{-1}, *PDI* = 1.41.

2.12.4. CMS-E19

88.3 mg hPG (1.2 mmol OH groups, M_n = 6.9 kDa; M_w = 12.4 kDa) was dried by dissolving in 1 mL of anhydrous pyridine and evaporating the solvent. Then the residue was dissolved in 7 mL dry pyridine. C19-mPEG350 (2.4 mmol, 1.6 g, previously dried at 50 °C under vacuum <5 × 10^{-2} mbar overnight) in a three-neck flask (equipped with a reflux-condenser, an olive, and a septum) was dissolved in 8 mL dry methylene chloride. At 0 °C, 0.3 mL thionyl chloride were added and after 10 min the temperature increased to the boiling point of methylene chloride. After 2 h, the solvent was evaporated by cryo-distillation. At 0 °C, the intermediate was dissolved in dry methylene chloride and the solution was added dropwise to the solution of hPG. After stirring overnight, the solvent was distilled off and the crude product purified with dialysis (2 kDa, 3 × 3 L) and ultrafiltration (MWCO 30 kDa, methanol) yielding the product as a colorless solid (284 mg, 64%).

^{1}H NMR (700 MHz, methanol-d$_4$, TMS): δ (ppm) = 4.20 (s, 2H, –CH$_2$–OCO–), 3.72–3.51 (m, 31.3H, mPEG repeating unit and hPG backbone), 3.35 (s, 3H, –O–CH$_3$), 2.33 (m, 4H, –OOC–CH$_2$–), 1.62 (m, 4H, –OOC–CH$_2$–C*H*$_2$–), 1.32 (m, 24H, –(CH$_2$)$_{13}$–). ^{13}C NMR (176 MHz, methanol-d$_4$, TMS): δ (ppm) = 174.9, 73.1z, 71.8–71.4, 70.3, 64.6, 59.3, 35.1, 31.7–30.4, 26.2. IR (cm^{-1}): 3399, 2917, 2850, 1712, 1486, 1306, 1226, 1111, 953, 851, 746. GPC: M_n = 32,300 g·mol^{-1}, M_w = 42,600 g·mol^{-1}, *PDI* = 1.32.

2.12.5. CMS-E18b

CMS-E18b was synthesized analog to CMS-E19. In total, 2.2 mg (1.7 mmol) C18b-mPEG750 were reacted with 186 µL thionyl chloride (305 mg, 2.6 mmol) and 105.6 g (1.4 mmol OH groups, M_n = 6.9 kDa; M_w = 12.4 kDa) hPG to yield after purification with UF (methanol, 30 kDa MWCO) 577 mg of a brown oil (42% yield).

^{1}H NMR (500 MHz, methanol-d_4, TMS): δ (ppm) = 7.08–6.69 (m, 0.4H, arom.-H); 4.21 (s, 2H, –CH_2–OCO–), 3.72–3.50 (m, 70.4H, mPEG repeating unit and hPG backbone), 3.36 (s, 3H, –O–CH_3), 2.55 (m, 1.6H, benzyl–H); 2.33 (m, 4H, –OOC–CH_2–), 1.61 (m, 4H, –OOC–CH_2–CH_2–, –CH_2–CH_2–Ph), 1.31 (br s, 44.5H, aliph. backbone); 0.91 (m, 3H, –CH_2–CH_3). ^{13}C NMR (125 MHz, methanol-d_4, TMS): δ (ppm) = 174.4, 73.0, 71.7–71.3, 70.2, 64.6, 59.2, 35.1, 31.2–30.2, 26.2, 23.9, 15.0. IR (cm^{-1}): 3454, 2922, 2855, 1732, 1456, 1349, 1248, 1098, 949, 849, 756. GPC: M_n = 33,300 g·mol^{-1}, M_w = 56,100 g·mol^{-1}, *PDI* = 1.68.

2.12.6. CMS-A18

Amide-based CMS nanocarriers CMS-A18 were synthesized according to procedures published elsewhere [16].

3. Results

3.1. Synthesis of the Ester-Based Core–Multishell Nanocarriers

3.1.1. Synthesis of the Shell Molecule

The double shells of the various CMS architectures were synthesized according to a previously published procedure [15]. The esterification reaction was conducted without a catalyst at 180 °C and under low pressure (<10^{-1} mbar, see Scheme 1). To avoid diester formation, stoichiometries of 3–4:1 (diacid to mPEG) were chosen. Purification was either carried out by precipitation (C12 and C15) or chromatography. Normal column chromatography was sufficient for the C18b-mPEG750 double shell but reverse-phase HPLC had to be applied for C18-mPEG350 and C19-mPEG350 to remove residual diacid.

3.1.2. Synthesis of the CMS Architectures

Using hPG as a core molecule instead of its amino derivative not only avoids the potentially toxic hPG–NH_2 as a degradation product, it also supersedes its synthesis from hPG amine and thus three synthetic steps [21].

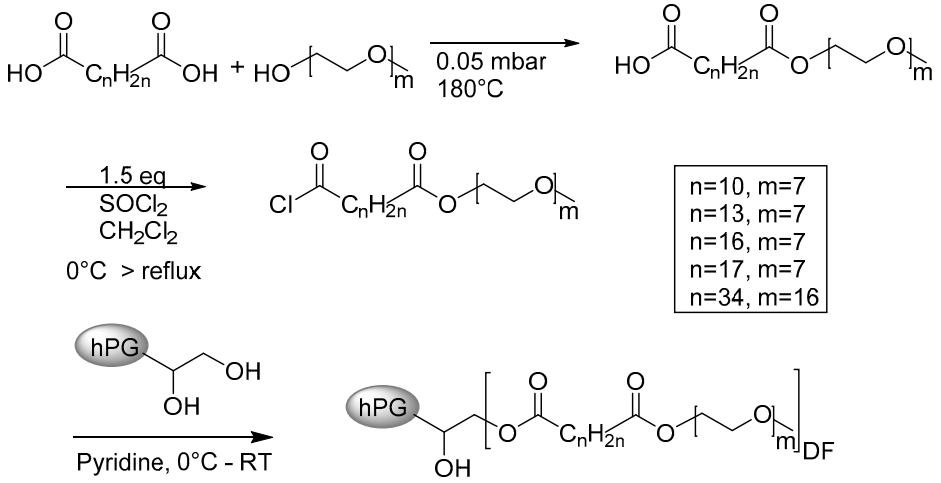

Scheme 1. Synthetic route of all ester-based CMS nanocarriers.

The alcohol of bare hPG, however, features a lowered nucleophilicity in comparison to its aminated counterpart. Therefore, a higher reactivity of the carboxylic group becomes necessary. Activation to the acid chloride prior to the reaction with thionyl chloride led to the desired product (see Scheme 1). The amounts of 0.8–2 eq. acid chloride-activated shell (depending on batch size) were used because of its sensitivity towards water. Ultrafiltration compared to dialysis yielded purer compounds and the molecular-weight cut-offs were between 3 kDa and 30 kDa in methanol, depending on the molecular weight of the double-shell.

3.2. Degree of Functionalisation

In order to estimate the degree of functionalization, the molecular weights of all CMS were determined by gel permeation chromatography (GPC) in DMF. All systems were as well analyzed with NMR spectroscopy. The results are given in Table 1, the estimated error of the determination of the DF by NMR is in the range of 10% (see Figure S2).

The molecular weights determined by GPC analysis were all in the same range. The degree of functionalization (DF) was determined from 1H NMR by comparing the combined hPG/mPEG peak to the signal of the aliphatic protons of the inner shell. The residual signal originated from core protons and therefore the DF could be calculated using Equation (1) for CMS nanocarrier with an inner shell length of 12 to 19 carbon atoms and Equation (2) for CMS-E18b.

$$DF = \frac{5}{\sigma_{a,e,f,g} - 31.8} \quad (1)$$

$$DF = \frac{5}{\sigma_{g} - 63.2} \quad (2)$$

The M_n of CMS nanocarriers and hPG were used for calculating the DF values from the GPC data, and are all stated in Table S1. The GPC data indicates that all nanocarriers were defined ($PDI < 2$) and of comparable molecular weights (M_n ~40 kDa). The GPC-based DF values were smaller than the ones calculated from NMR spectra. This was due to the comparison to a linear standard (polystyrene) in the GPC analysis that made the nanocarriers appear smaller, which is why the estimation via NMR is more realistic.

Table 1. Estimation of the degree of functionalization (NMR) and GPC analytical data.

Compound	M_n [kDa]	*PDI*	*DF* (NMR)
CMS-A18	41.8	1.85	65%
CMS-E12	32.2	1.31	88%
CMS-E15	43.1	1.79	90%
CMS-E18	34.9	1.41	88%
CMS-E19	32.3	1.31	75%
CMS-E18b	33.3	1.68	69%

3.3. DSC Measurements

Differential scanning calorimetry was used to analyze the carriers regarding their phase-separation and thermal transitions (Figure 2). All carriers except CMS-E18b and CMS-E12 exhibited two peaks. Each of those peaks represents a segregated phase. The calorigrams of CMS-E18b and CMS-E12 only showed one peak. Possible reasons for this include that no phase segregation took place in these carriers or that the melting point (T_m) of the aliphatic phase was too close to the T_m of the mPEG phase to result in separated peaks. The mPEG phase exhibited a T_m in the −20 to −10 °C region for all carriers, which was in accordance with the melting point of mPEG350 (−8 °C) [27]. The second peak represents the hydrophobic domain and proves phase-segregation. The temperature at which this transition occurred reflects the interaction between chains in the phase that needs to be overcome

for a less ordered state. Comparing CMS-E12, CMS-E15, CMS-E18, and CMS-E19, this T_m increases as expected with higher chain lengths. Surprisingly, there is a significant step between CMS-E18 and CMS-E19 of 26.8 °C with a difference of an inner chain length of only one methylene group. This unexpectedly high T_m also influences other properties of the unimolecular micelle. While all other CMS nanocarriers are highly soluble in water, the solubility of CMS-E19 at RT is only 60 mg·L^{-1}. At temperatures around 60 °C, it exceeds 5 mg mL^{-1}, which is why the loading experiments were also carried out at this temperature.

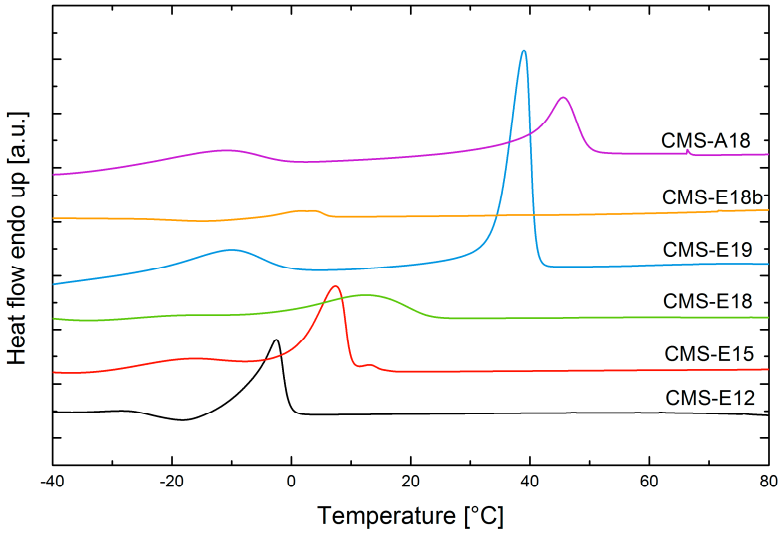

Figure 2. DSC measurements of CMS nanocarriers. Samples have been heated to 85 °C to erase any thermal history. Graphs show second heating at 5 °C min^{-1}.

3.4. DLS Analysis of Loaded and Unloaded CMS Nanocarriers

DLS analysis was applied to estimate hydrodynamic diameters in polar solvents and aggregation phenomena upon loading in water. The two pharmacophores dexamethasone and tacrolimus were chosen for two reasons: First, they are both commonly used in the therapy of inflammatory skin diseases. Secondly, they are very different on a molecular level. While dexamethasone is a small molecule and exhibits a rigid structure, tacrolimus features a relatively high molecular weight and dynamic conformal changes. Table S2 summarizes the number-averaged results in methanol, which reflect well the sizes of the unimolecular micelles. In water, the nanocarriers readily aggregated into smaller and bigger aggregates, which was not the case for methanol. The hydrodynamic diameters of ester-based nanocarriers were all in the range of 5 to 10 nm, which was expected for unimolecular micelles and classifies them as nano-scale objects.

As the intensity-based distribution of a DLS measurement focuses more on larger particles in suspension, the abundance of larger aggregates becomes visible. At the concentration of 5 mg mL^{-1}, DLS data (Table 2) indicated the formation of small aggregates even without a guest molecule. This was in accordance to the findings published by Rabe et al. that suggested that CMS-A18 formed aggregates of around eight unimers [28]. The next generation ester-based nanocarriers showed comparable sizes that suggest a similar trend towards aggregates at higher concentrations.

When loaded with a hydrophobic guest molecule, the tendency towards aggregation increased. The smaller aggregates disappeared and the larger colloidal structures became more predominant in the DLS spectra, which is in accordance with previously published data [15,18]. These results suggest bridging of two or more unimolecular micelles by a hydrophobic drug molecule, similar to the formation of hydrophobic patches that drove aggregation. Tacrolimus-loaded CMS-A18 was the only exception to this trend, but it also featured one of the lowest loading capacities. The ζ-potential of all

carriers were approximately neutral. Thus, electrostatic interactions are assumed to play a minor role in the aggregation phenomena.

Table 2. Intensity-based hydrodynamic diameters of unloaded and loaded CMS nanocarriers and the ζ potential of unloaded CMS nanocarriers. Samples had a concentration of 5 g·mL^{-1} polymer and were measured at 25 °C. Experiments were performed in triplicates.

Compound	Unloaded		Tacrolimus-Loaded		Dexamethasone-Loaded		ζ Potential
	d [nm]		*d* [nm]		*d* [nm]		[mV]
CMS-A18	15 210	(81%) (19%)	19 204	(5%) (95%)	32		0.07 ± 0.09
CMS-E12	14 134	(48%) (52%)	14 215	(5%) (95%)	63 361	(10%) (90%)	−1.27 ± 1.04
CMS-E15	15 138	(23%) (77%)	16 208	(10%) (90%)	16 270	(9%) (91%)	0.01 ± 0.06
CMS-E18	37		18 224	(15%) (85%)	24 272	(25%) (74%)	−5.9 ± 0.7
CMS-E19 *	216		364		47 329	(9%) (91%)	0.01 ± 0.03
CMS-E18b	76		123		121		−0.003 ± 0.06

* Measured at 60 °C.

3.5. Loading Capacities of Dexamethasone and Tacrolimus

The loading capacity (*LC*) of a carrier depends on the method and on the guest molecule encapsulated in it. It is defined as the solubilized mass concentration of a guest compared to the mass concentration of its host (see Equation (3)).

$$LC = \frac{w(guest) - w_0(guest)}{w(carrier)} \quad (3)$$

To determine *LC*, dexamethasone and tacrolimus were encapsulated via the film uptake method, respectively. Fifty weight percent of the drug was dissolved in ethanol and the solvent was removed to form a film. Then, the stock solution of the carrier in water was added and the suspension stirred for 22 h. After removal of the non-solubilized drug by filtration, the guest concentration was measured by HPLC and the loading capacities calculated (see Equation (3)). Dexamethasone, a rather small hydrophobic drug, can be encapsulated in all carriers (except for CMS-E19) with reasonable loading capacities (Figure 3 and Table S4 for numerical values). Comparing CMS-E12, CMS-E15, CMS-E18, and CMS-E19, one could find no clear trend between the chain length and the melting points obtained from DSC measurements (see Figure S3). The higher the hydrophobic interactions between the carriers, the lower were the interactions between drug and carrier. CMS-A18 and CMS-E18 differ only in the bond between core and inner shell (amide versus ester bond). Amide bonds are known to form hydrogen bonds and can induce highly ordered structures. This seems to be beneficial for a rigid and planar drug such as dexamethasone. Furthermore, hydrogen bonds can be formed between the core amide and hydroxyl groups of the guest molecule. These two factors resulted in an overall higher loading capacity for dexamethasone in CMS-A18 compared to CMS-E18. Due to its branching and structural diversity, CMS-E18b exhibited the least ordered hydrophobic segment, which also resulted in a low T_m (see Figure 2). Apparently, the low degree of order for the hydrophobic chains was not beneficial compared to the unbranched system CMS-E18 for encapsulation of the rigid drug dexamethasone.

Employing the same method and a similar, HPLC-based analysis, the LCs for tacrolimus were determined as well (see Figure 4 and Table S4 for numerical values). Among the carrier architectures in discussion, there was a clear maximum at the inner shell length of 15 carbon atoms. This was

due to two effects. Along the carriers, CMS-E12–CMS-E15–CMS-E18, the increasing hydrophobic interactions impeded higher drug loading such as in the case of dexamethasone. Additionally, the sterically demanding molecule tacrolimus required a minimum size of hydrophobic segments, which was too small in the case of CMS-E12. Hence, the optimum size in this row was 15 carbon atoms.

Comparing CMS-A18 to CMS-E18, exchanging the ester bonds to amide bonds had a tremendous effect on the *LC*. The rather rigid segments of C18 chains in the amide-functionalized carrier impaired efficient encapsulation of the flexible and large macrocycle tacrolimus. This did not seem to be the case for CMS-E18. Three to fourfold higher *LC*s were measured for this system. CMS-E18b, which featured the least ordered hydrophobic segment, had a similar *LC* to CMS-E18. The branching of the inner shell and a longer PEG outer shell was not beneficial for the encapsulation of tacrolimus.

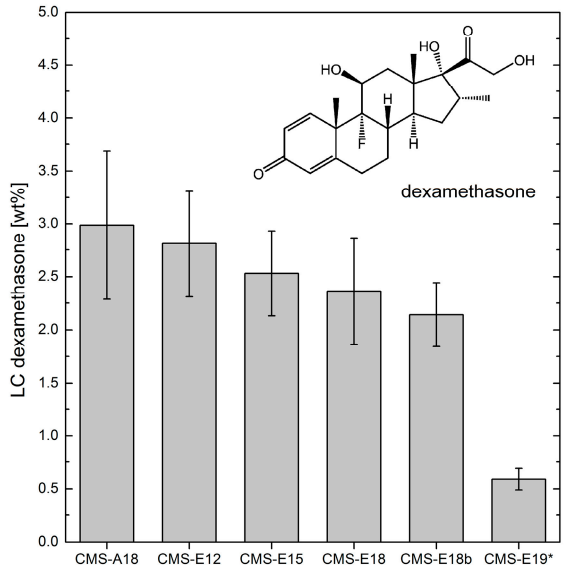

Figure 3. Loading capacities of the investigated carrier systems. Encapsulation was performed with the film uptake method, n = 3, * performed at 60 °C.

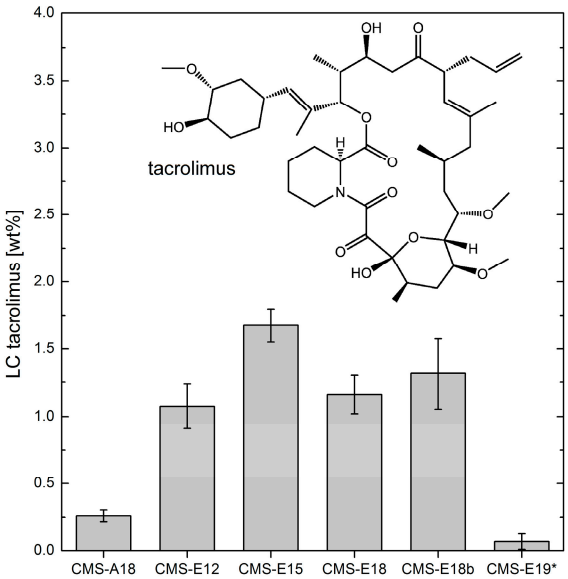

Figure 4. Loading capacities of tacrolimus in the examined carrier systems vs. the T_m values of the inner shell. Encapsulation was done with the film-uptake method, n = 3, error bars indicate standard deviation, * performed at 60 °C.

3.6. Enzymatic Degradation of Unloaded Carriers

The rate at which the carrier is degraded enzymatically was determined by adding a lipase to a solution of nanotransporter in PBS and taking samples at certain time points. The commercially available lipase from Rhizomucor miehei was chosen because of the resemblance of the inner shell building blocks to fatty acids, its native substrate. The samples were lyophilized, redissolved in DMSO-d_6 and analyzed in ^{1}H NMR. The α-protons and the methylene group adjacent to the ester group on the PEG side were tracked in the ^{1}H NMR spectra (the protocol was adapted from a method published earlier by our group) [29]. The chemical shift of the α-protons depends on whether the carboxylic acid was esterified or not. At $t = 0$, there were only the peak at 2.23 ppm, which represented the 4 esterified α-protons, as well as the peak at 4.07 ppm, that originated from the two PEG protons adjacent to the ester bond. These signals indicated ester bonds only. Upon degradation, the peak at 4.07 ppm decreased and two new peaks appeared and started to grow over time in the NMR spectrum (see Figure S4). One was a triplet at 2.17 ppm and the other one was a broad signal at 2.12 ppm. Both represent non-esterified α-protons, the triplet originated from a non-carrier bound carboxylic functionality, while the broad signal can be attributed to a carboxylic function still bound to the nanocarrier architecture. Hence, ester cleavage is reflected in the signals of the α-protons. Whether the inter-shell ester or the core-ester is cleaved (Figure 5), can be determined by tracking the PEG protons at 4.07 ppm. By cleavage at the inter-shell site, this signal will lose intensity. The results of this analysis are plotted in Figure 6 and complement a previous study examining the degradation of the nanocarriers by skin lysate [22]. The graph shows degradation of more than 70% of all ester groups for all carriers after six days. Since the used method not only allows one to follow the total cleavage of all ester groups but also the individual monitoring of cleavage sites, one can see which bond was cleaved first (Figures 5 and 6 and Figure S5).

Surprisingly, the core ester bond was cleaved at a comparable rate as the inter-shell ester. In the first 24 h, almost no inter-shell esters cleaved. The reaction rate was very similar after that. The simultaneous cleavage of core and inter-shell ester showed that an enzyme of a molecular weight of 29.6 kDa still could enter the spherical particle and catalyze ester cleavage, which indicated the high flexibility of the CMS nanocarriers. In contrast, no cleavage could be observed for the amide-based CMS nanotransporters under the same conditions (see Figure S6). This was surprising because the CMS-A18 also has esters as the linkage of the diacid with the mPEG and hence ester cleavage should have been still possible to a certain degree.

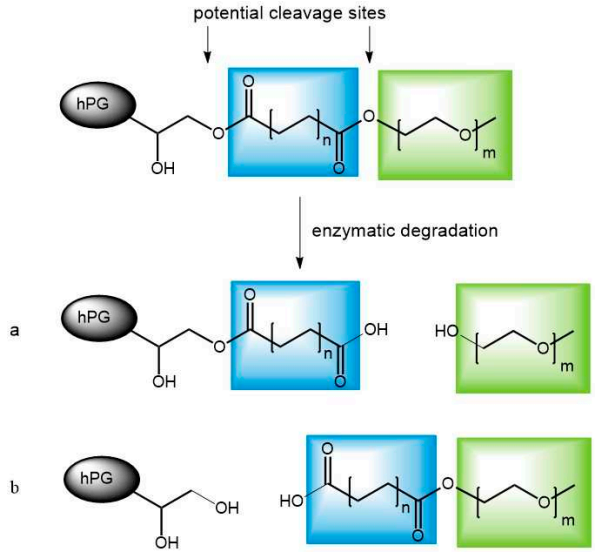

Figure 5. Different cases of ester cleavage. Depending on the site of cleavage, either the double shell (**a**) or the PEG-chain (**b**) is cleaved off.

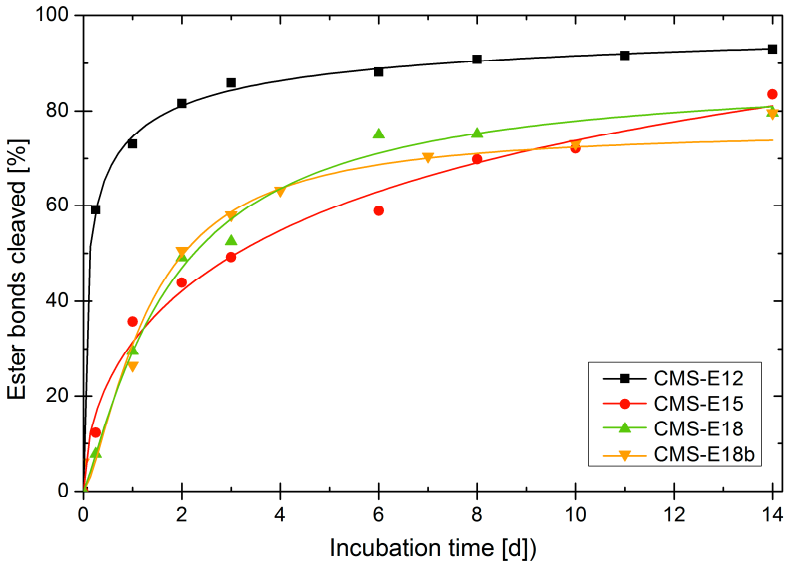

Figure 6. Comparison of the degree of hydrolysis for the ester bonds by lipase from Rhizomucor miehei as determined by NMR (DMSO-d_6), n = 1.

3.7. Release Mediated by Enzymatic Cleavage

The guest molecule is encapsulated in the CMS nanocarrier by physical entrapment, which leads to its solubilization. Its release is realized by diffusion out of the nanoparticle into the surrounding medium. A second mechanism is the degradation of the carrier in a confined volume upon which it will lose its ability to solubilize hydrophobic drugs. In order to determine the kinetics of this second mechanism, the particles were loaded with dexamethasone and enzymatically degraded. The released drug precipitated, and was separated by centrifugation. The reduced drug content of the supernatant was measured by HPLC to determine the remaining solubilizing effect of the partially degraded carrier. After resuspension, the procedure was repeated at different time points. In this procedure, we focused on the best performing carrier systems, CMS-E12, CMS-E15 and CMS-E18. In order to only determine the surplus value of the CMS nanotransporter, from each value, $c(sup)$ and $c_{t=0}(sup)$, the natural solubility of Dexamethasone, $c_{sat}(Dx)$, was deducted (Equation (4)). Then, the ratio of each value $c(sup)$ to its initial value $c_{t=0}(sup)$ was calculated and subtracted from 1 to normalize the graphs. CR (cumulative release) represents the percentage of drug that was released from the carrier due to degradation.

$$CR = 1 - \frac{c(sup) - c_{sat}(Dx)}{c_{t=0}(sup) - c_{sat}(Dx)} \quad (4)$$

This protocol was carried out with double carrier concentration to increase the effect but the carrier/enzyme ratio was kept identical to get a comparable time scale in which the degradation took place. Figure 7 indicates that all carriers underwent a rapid change in their transport properties. The solubilization enhancing properties strongly diminished within a degradation time of one day. In the same period, only around 3% of the payload was released in the UC and around 20% in seven days.

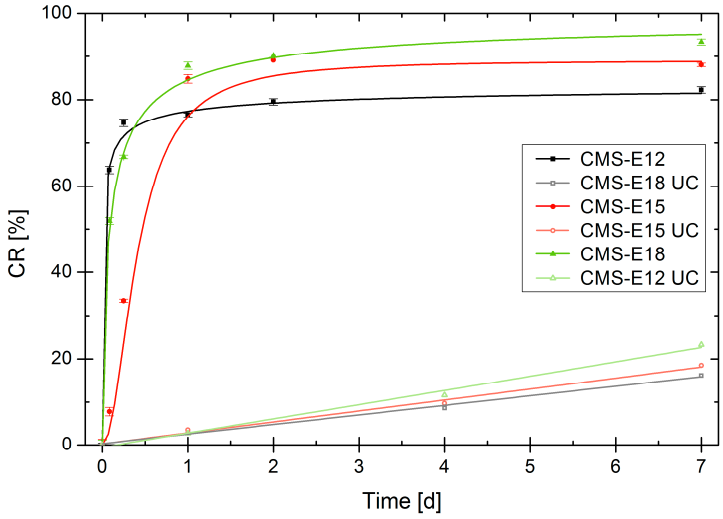

Figure 7. Increase of drug release upon degradation in comparison to the untreated control (UC). CMS nanocarrier concentration 10 mg·mL^{-1}, n = 3.

4. Discussion

By introducing the ester linkage between core and inner shell of CMS nanocarriers, an easier synthetic route was established. The synthesis was reduced to three synthetic steps as compared to six for the amide-based system. The resulting CMS nanocarriers showed different aggregation phenomena from its amide-functionalized counterpart. These properties were strongly linked to the loading capacities of the carriers. While a short inner shell of 12 carbon atoms and amide bonds were beneficial for encapsulation of the rigid molecule dexamethasone, the bulkier tacrolimus showed a clear optimum at an inner shell chain length of 15 carbon atoms which was attached via an ester linkage. Furthermore, ester-based carriers showed a high degree of enzymatic degradability. Hence, this new class of ester-based CMS nanocarrier presented here combines optimized loading capacities for the anti-inflammatory hydrophobic drugs dexamethasone and tacrolimus, easy synthesis, and enzymatic degradability.

Supplementary Materials: Supplementary materials are available online at http://www.mdpi.com/2073-4360/9/8/316/s1.

Acknowledgments: We acknowledge Pamela Winchester for proofreading the manuscript and thank Eike Mucha, Maren Meurer, and Oliver Etzold for their support in the lab as well as Luisa Duque and Roland Bodmeier for their help with the DSC measurements. We would also like to thank the Deutsche Forschungsgemeinschaft (DFG) via SFB 1112 for the financial support.

Author Contributions: Michael L. Unbehauen and Rainer Haag conceived and designed the experiments; Michael L. Unbehauen synthesized the nanocarriers CMS-E18, CMS-E19 and CMS-E18b and performed the experiments; Michael L. Unbehauen analyzed the data; Emanuel Fleige, Florian Paulus and Sam Dylan Moré provided the Nanocarriers CMS-E12, CMS-E15 and CMS-A18 and the performed GPC Analysis; Stefan Mecking and Brigitta Schemmer contributed the C19 building block; and Michael L. Unbehauen wrote the paper.

Conflicts of Interest: The authors declare no conflict of interest.

Abbreviations

CMC	Critical micellar concentration
CMS	Core–multishell
CR	Cumulative release
DDS	Drug delivery system
DF	Degree of functionalization
hPG	Hyperbranched polyglycerol

hPG–NH_2	Hyperbranched polyglycerol amine
ITCC	Indotriscarbocyanine
PEI	Poly(ethyleneimine)

References

1. Williams, A.C.; Barry, B.W. Penetration enhancers. *Adv. Drug Deliv. Rev.* **2012**, *64*, 128–137. [CrossRef]
2. Papakostas, D.; Rancan, F.; Sterry, W.; Blume-Peytavi, U.; Vogt, A. Nanoparticles in dermatology. *Arch. Dermatol. Res.* **2011**, *303*, 533–550. [CrossRef] [PubMed]
3. Bolzinger, M.-A.; Briançon, S.; Pelletier, J.; Chevalier, Y. Penetration of drugs through skin, a complex rate-controlling membrane. *Curr. Opin. Colliod Interface Sci.* **2012**. [CrossRef]
4. Alves, M.P.; Scarrone, A.L.; Santos, M.; Pohlmann, A.R.; Guterres, S.S. Human skin penetration and distribution of nimesulide from hydrophilic gels containing nanocarriers. *Int. J. Pharm.* **2007**, *341*, 215–220. [CrossRef] [PubMed]
5. Alvarez-Román, R.; Naik, A.; Kalia, Y.N.; Guy, R.H.; Fessi, H. Enhancement of Topical Delivery from Biodegradable Nanoparticles. *Pharm. Res.* **2004**, *21*, 1818–1825. [CrossRef] [PubMed]
6. Rancan, F.; Papakostas, D.; Hadam, S.; Hackbarth, S.; Delair, T.; Primard, C.; Verrier, B.; Sterry, W.; Blume-Peytavi, U.; Vogt, A. Investigation of polylactic acid (PLA) nanoparticles as drug delivery systems for local dermatotherapy. *Pharm. Res.* **2009**, *26*, 2027–2036. [CrossRef] [PubMed]
7. Patzelt, A.; Richter, H.; Knorr, F.; Schäfer, U.; Lehr, C.-M.; Dähne, L.; Sterry, W.; Lademann, J. Selective follicular targeting by modification of the particle sizes. *J. Control. Release* **2011**, *150*, 45–48. [CrossRef] [PubMed]
8. Shim, J.; Seok Kang, H.; Park, W.-S.; Han, S.-H.; Kim, J.; Chang, I.-S. Transdermal delivery of mixnoxidil with block copolymer nanoparticles. *J. Control. Release* **2004**, *97*, 477–484. [CrossRef]
9. Newkome, G.R.; Moorefield, C.N.; Baker, G.R.; Saunders, M.J.; Grossman, S.H. Unimolecular Micelles. *Angew. Chem. Int. Ed. Engl.* **1991**, *30*, 1178–1180. [CrossRef]
10. Jansen, J.F.; de Brabander-van den Berg, E.M.; Meijer, E.W. Encapsulation of guest molecules into a dendritic box. *Science* **1994**, *266*, 1226–1229. [CrossRef] [PubMed]
11. Kurniasih, I.N.; Keilitz, J.; Haag, R. Dendritic nanocarriers based on hyperbranched polymers. *Chem. Soc. Rev.* **2015**, *44*, 4145–4164. [CrossRef] [PubMed]
12. Kataoka, K.; Harada, A.; Nagasaki, Y. Block copolymer micelles for drug delivery: Design, characterization and biological significance. *Adv. Drug Deliv. Rev.* **2001**, *47*, 113–131. [CrossRef]
13. Prabaharan, M.; Grailer, J.J.; Pilla, S.; Steeber, D.A.; Gong, S. Amphiphilic Multi-Arm Block Copolymer Based on Hyperbranched Polyester, Poly(L-lactide) and Poly(ethylene glycol) as a Drug Delivery Carrier. *Macromol. Biosci.* **2009**, *9*, 515–524. [CrossRef] [PubMed]
14. Li, X.; Qian, Y.; Liu, T.; Hu, X.; Zhang, G.; You, Y.; Liu, S. Amphiphilic multiarm star block copolymer-based multifunctional unimolecular micelles for cancer targeted drug delivery and MR imaging. *Biomaterials* **2011**, *32*, 6595–6605. [CrossRef] [PubMed]
15. Radowski, M.R.; Shukla, A.; von Berlepsch, H.; Böttcher, C.; Pickaert, G.; Rehage, H.; Haag, R. Supramolecular aggregates of dendritic multishell architectures as universal nanocarriers. *Angew. Chem. Int. Ed. Engl.* **2007**, *46*, 1265–1269. [CrossRef] [PubMed]
16. Küchler, S.; Radowski, M.R.; Blaschke, T.; Dathe, M.; Plendl, J.; Haag, R.; Schäfer-Korting, M.; Kramer, K.D. Nanoparticles for skin penetration enhancement—A comparison of a dendritic core-multishell-nanotransporter and solid lipid nanoparticles. *Eur. J. Pharm. Biopharm.* **2009**, *71*, 243–250. [CrossRef] [PubMed]
17. Quadir, M.A.; Radowski, M.R.; Kratz, F.; Licha, K.; Hauff, P.; Haag, R. Dendritic multishell architectures for drug and dye transport. *J. Control. Release* **2008**, *132*, 289–294. [CrossRef] [PubMed]
18. Fleige, E.; Ziem, B.; Grabolle, M.; Haag, R.; Resch-Genger, U. Aggregation Phenomena of Host and Guest upon the Loading of Dendritic Core-Multishell Nanoparticles with Solvatochromic Dyes. *Macromolecules* **2012**, *45*, 9452–9459. [CrossRef]
19. Weber, M.; Zoschke, C.; Sedighi, A.; Fleige, E.; Haag, R.; Schäfer-Korting, M. Free Energy Simulations of Cargo-Carrier Interactions for Core-Multishell Nanotransporters. *J. Nanomed. Nanotechnol.* **2014**, *5*. [CrossRef]

20. Zhu, Y.; Hazeldine, S.; Li, J.; Oupický, D. Dendritic polyglycerol with secondary amine shell as an efficient gene delivery vector with reduced toxicity. *Polym. Adv. Technol.* **2014**, *25*, 940–947. [CrossRef]
21. Roller, S.; Zhou, H.; Haag, R. High-loading polyglycerol supported reagents for Mitsunobu- and acylation-reactions and other useful polyglycerol derivatives. *Mol. Divers.* **2005**, *9*, 305–316. [CrossRef] [PubMed]
22. Hönzke, S.; Gerecke, C.; Elpelt, A.; Zhang, N.; Unbehauen, M.; Kral, V.; Fleige, E.; Paulus, F.; Haag, R.; Schäfer-Korting, M.; et al. Tailored dendritic core-multishell nanocarriers for efficient dermal drug delivery: A systematic top-down approach from synthesis to preclinical testing. *J. Control. Release* **2016**, *242*, 50–63. [CrossRef] [PubMed]
23. Stemp, F.; Quinzler, D.; Heckler, I.; Mecking, S. Long-Chain Linear C 19 and C 23 Monomers and Polycondensates from Unsaturated Fatty Acid Esters. *Macromolecules* **2011**, 4159–4166. [CrossRef]
24. Sunder, A.; Hanselmann, R.; Frey, H.; Mülhaupt, R. Controlled synthesis of hyperbranched polyglycerols by ring-opening multibranching polymerization. *Macromolecules* **1999**, *32*, 4240–4246. [CrossRef]
25. Fulmer, G.R.; Miller, A.J.M.; Sherden, N.H.; Gottlieb, H.E.; Nudelman, A.; Stoltz, B.M.; Bercaw, J.E.; Goldberg, K.I. NMR Chemical Shifts of Trace Impurities: Common Laboratory Solvents, Organics, and Gases in Deuterated Solvents Relevant to the Organometallic Chemist. *Organometallics* **2010**, *29*, 2176–2179. [CrossRef]
26. Brundiek, H.; Sa, S.; Evitt, A.; Kourist, R.; Bornscheuer, U.T. The short form of the recombinant CAL-A-type lipase UM03410 from the smut fungus Ustilago maydis exhibits an inherent trans-fatty acid selectivity. *Appl. Microbiol. Biotechnol.* **2012**, *94*, 141–150. [CrossRef] [PubMed]
27. Chauvin, C.; Ollivrin, X.; Alloina, F.; Lenest, J.-F.; Sanchez, J.-Y. Lithium salts based on oligoether sulfate esters. *Electrochim. Acta* **2005**, *50*, 3843–3852. [CrossRef]
28. Rabe, C.; Fleige, E.; Vogtt, K.; Szekely, N.; Lindner, P.; Burchard, W.; Haag, R.; Ballauff, M. The multi-domain nanoparticle structure of a universal core-multi-shell nanocarrier. *Polymer* **2014**, *55*, 6735–6742. [CrossRef]
29. Kurniasih, I.N.; Liang, H.; Kumar, S.; Mohr, A.; Sharma, S.K.; Rabe, J.P.; Haag, R. A bifunctional nanocarrier based on amphiphilic hyperbranched polyglycerol derivatives. *J. Mater. Chem. B* **2013**, *1*, 3569. [CrossRef]

Supporting Information

Biodegradable Core-Multishell Nanocarriers: Influence of Inner Shell Structure on the Encapsulation Behavior of Dexamethasone and Tacrolimus

Michael L. Unbehauen [1], Emanuel Fleige [1,2], Florian Paulus [1,2], Brigitta Schemmer [3], Stefan Mecking [3], Sam Dylan Moré [2] and Rainer Haag [1,*]

[1] Freie Universität Berlin, Institute for Chemistry and Biochemistry, Takustraße 3, 14195 Berlin, Germany
[2] DendroPharm GmbH, Arnimallee 14, 14195 Berlin, Germany
[3] Chemical Materials Science, Department of Chemistry, University of Konstanz, Universitätsstraße 10, 78467 Konstanz, Germany
* Correspondence: haag@chemie.fu-berlin.de; Tel.: +49-30-838-52633

1. Material and Methods

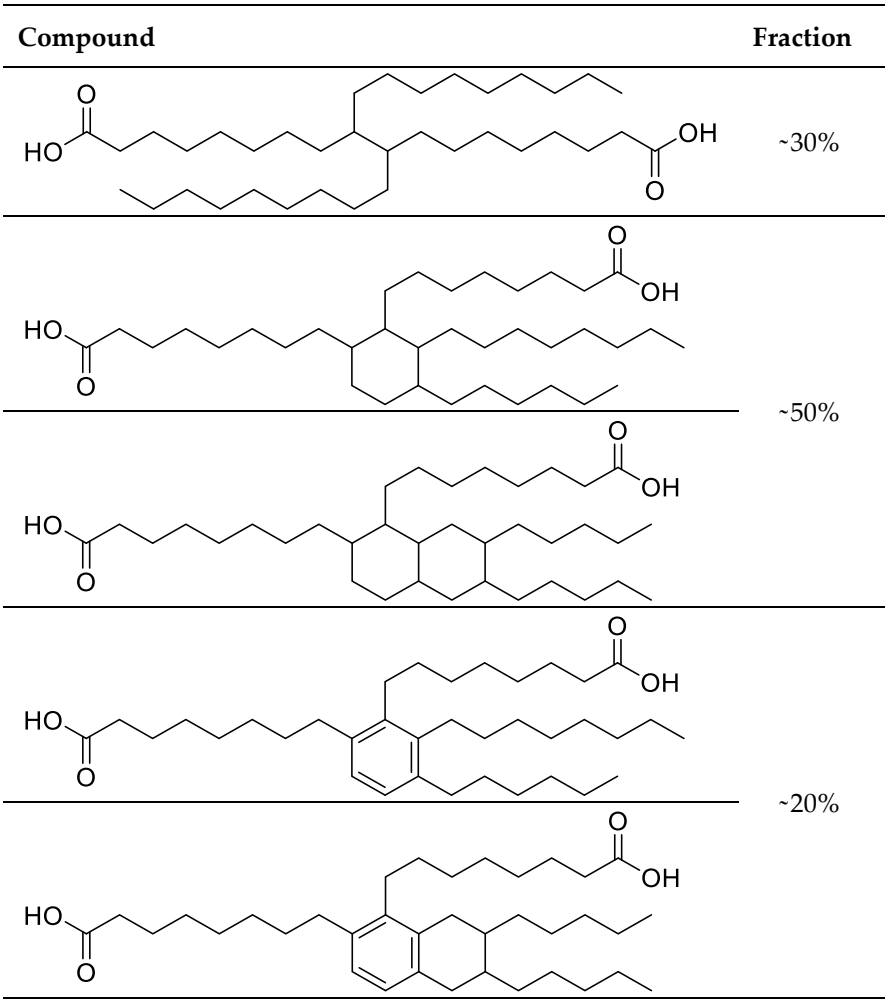

Scheme S1. Constituents of the dimeric fraction of EMPOL 1026.

The compound C18b is a mixture of different isomers of the dimeric fraction of the product EMPOL 1026 from Cognis. The dimeric fraction was isolated by column chromatography with hexane/ethyl acetate on acidified (acetic acid) silica. The dimeric fraction comprises of the compounds that are given in Scheme S1 and its isomers.

2. Degree of Functionalization

Table S1. Estimation of the degree of functionalization from GPC analytical data based on M_w.

compound	DF (GPC)
CMS-A18	42%
CMS-E12	20%
CMS-E15	45%
CMS-E18	24%
CMS-E19	29%
CMS-E18b	42%

2.1. Calculation of DF via NMR

All signals between 4.48 ppm and 3.32 ppm and an additional peak at 5.20 ppm can be attributed to all methylene and methine protons of hPG (Figure S1, a) and is partially overlaid with peaks assigned to the PEG backbone. (Figure S1, e,f,g) The aliphatic signal at 1.34 ppm, which has 18 protons (d), is needed to estimate the fraction that is assigned to the hPG backbone (a).

Per glycerol unit, the signal (a) originates from 5 protons of the hPG backbone and, depending on the degree of functionalization (DF), another 28.8 protons are in position e + f at the PEG backbone and additional 3 at position g (Equation S1 and S2). The signal of the 18 protons in (d) also depends on the DF (Equation S3).

Having established these relations (S1-3), the focus is now on the single double-shell chain. Scaling the peak (d) ppm to 18, one can now calculate the relation between DF and $\sigma_{a,e,f,g}$ (Equation S4) using Equation S2 and S3. This equation is then simplified to Equation S5 and later solved for DF to yield Equation S6, which now can be used to calculate DF from $\sigma_{a,e,f,g}$ after having set σ_d to 18. This procedure works equally for CMS-A18, for CMS-E12 σ_d set to 12, for CMS-E18 to 24, and for CMS-E19 to 26. An adapted form of this equation (Equation S7) was used to calculate DF of CMS-E18b. In this case, the methoxy peak at 3.36 ppm was set at 3.

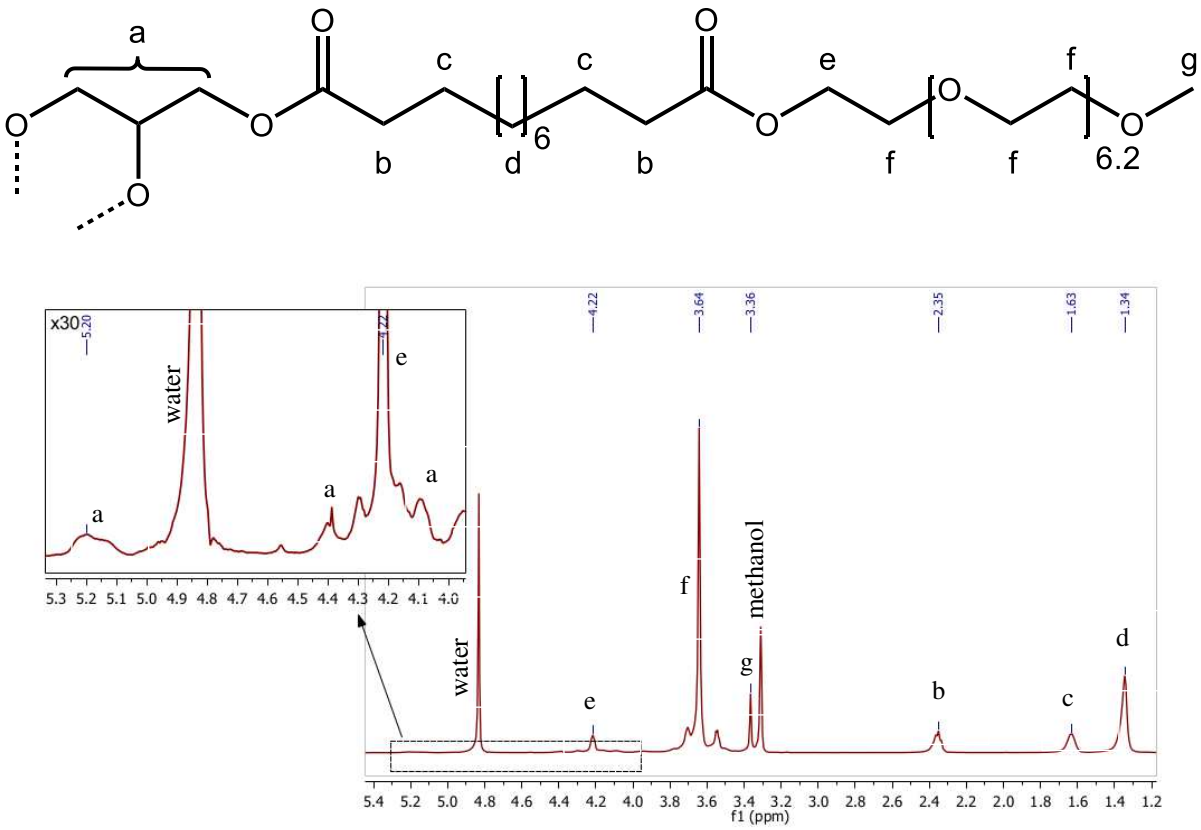

Figure S1. Exemplary chemical structure of a functionalized glycerol unit (top) and the respective ^{1}H-NMR spectrum (bottom) of CMS-E12.

$$\sigma_{a,e,f,g} = 5 + 7.2 \cdot 4 \cdot DF + 3 \cdot DF \tag{S1}$$

$$\sigma_{a,e,f,g} = 5 + 31.8 \cdot DF \tag{S2}$$

$$\sigma_{d} = 18 \cdot DF \tag{S3}$$

$$\sigma_{a,e,f,g} = \frac{\sigma_{a,e,f,g}}{\sigma_{d}} \cdot 18 = \frac{5 + 31.8 \cdot DF}{DF} \tag{S4}$$

$$\sigma_{a,e,f,g} = \frac{5}{DF} + 31.8 \tag{S5}$$

$$DF = \frac{5}{\sigma_{a,e,f,g} - 31.8} \tag{S6}$$

$$DF = \frac{5}{\sigma_{g} - 63.2} \tag{S7}$$

2.2. Accuracy of the NMR experiment

Assuming an average measurement error (ME) of 3 %, the deviation for the measured DF was calculated depending on the real DF (see Figure S2) using Equation S8. This Equation combines Eq. S5

and S6 and estimates the deviation by converting a theoretical DF into an NMR integral σ, adding or subtracting the measuring error (ME) and converting it back. Equation S8 is valid for CMS nanocarriers using mPEG350, S9 for CMS-E18b. As depicted in Fig. S2, the range of error increases with higher DF, leading to a rather rough estimation for highly functionalized CMS architectures.

$$DF_{min/max} = \frac{5}{\left(\frac{5}{DF_{real}} + 31.8\right) \cdot (1 \pm ME) - 31.8} \tag{S8}$$

$$DF_{min/max} = \frac{5}{\left(\frac{5}{DF_{real}} + 63.2\right) \cdot (1 \pm ME) - 63.2} \tag{S9}$$

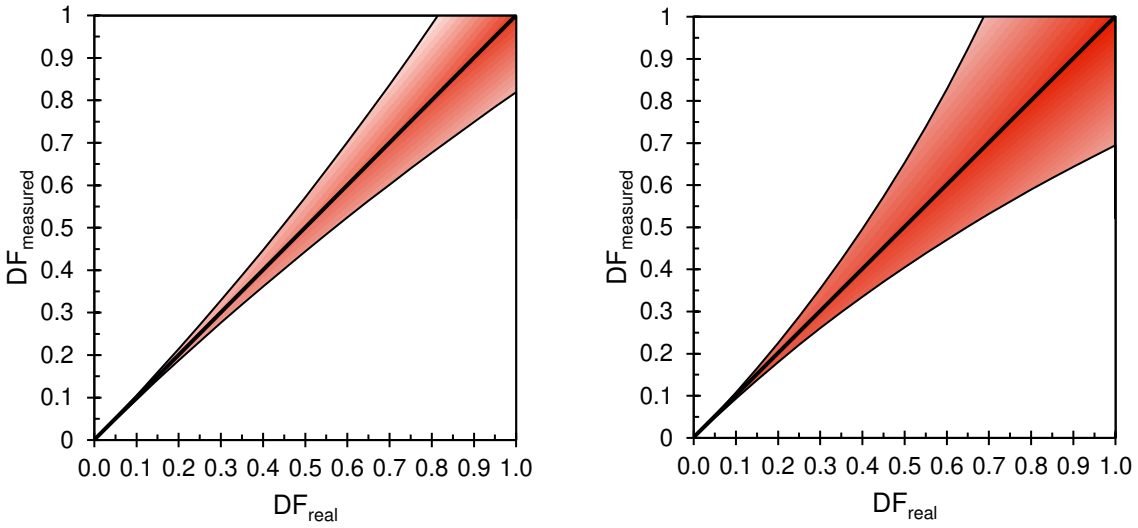

Figure S2. Estimated range of deviation (red) based on a measuring error of the NMR-experiment of 3% for CMS with mPEG350 (left) and mPEG750 (right).

3. Hydrodynamic sizes

Table S2. Hydrodynamic diameters of CMS in methanol determined by DLS.

Compound	Size (DLS, diameter, methanol, number)
CMS-A18	6.4
CMS-E12	8.5
CMS-E15	5.9
CMS-E18	8.6
CMS-E19	6.9
CMS-E18b	8.2

Table S3. Hydrodynamic diameters of CMS water, before and after filtration, and in PBS determined by DLS, percentage of signal in brackets.

Compound	Size before filtration	Size after filtration	Size after addition of PBS
CMS-E12	14.5 nm (43%) 228 nm (54%)	13.8 nm (48%) 143 nm (52%)	14.8 nm (48%) 143 nm (48%)
CMS-E15	14.1 nm (27%) 113 nm (73%)	16.3 nm (31%) 145 nm (69%)	20.6 nm (36%) 154 nm (64%)
CMS-E18	42.3 nm	39.2 nm	39.6 nm

The hydrodynamic diameter was measured before and after filtration with a 450 nm RC filter and after the dissolution of PBS salt. The sizes and populations widely remained the same, only in CMS-E12 the aggregates' diameters decreased.

4. Loading Capacity vs. T_m of the inner shell

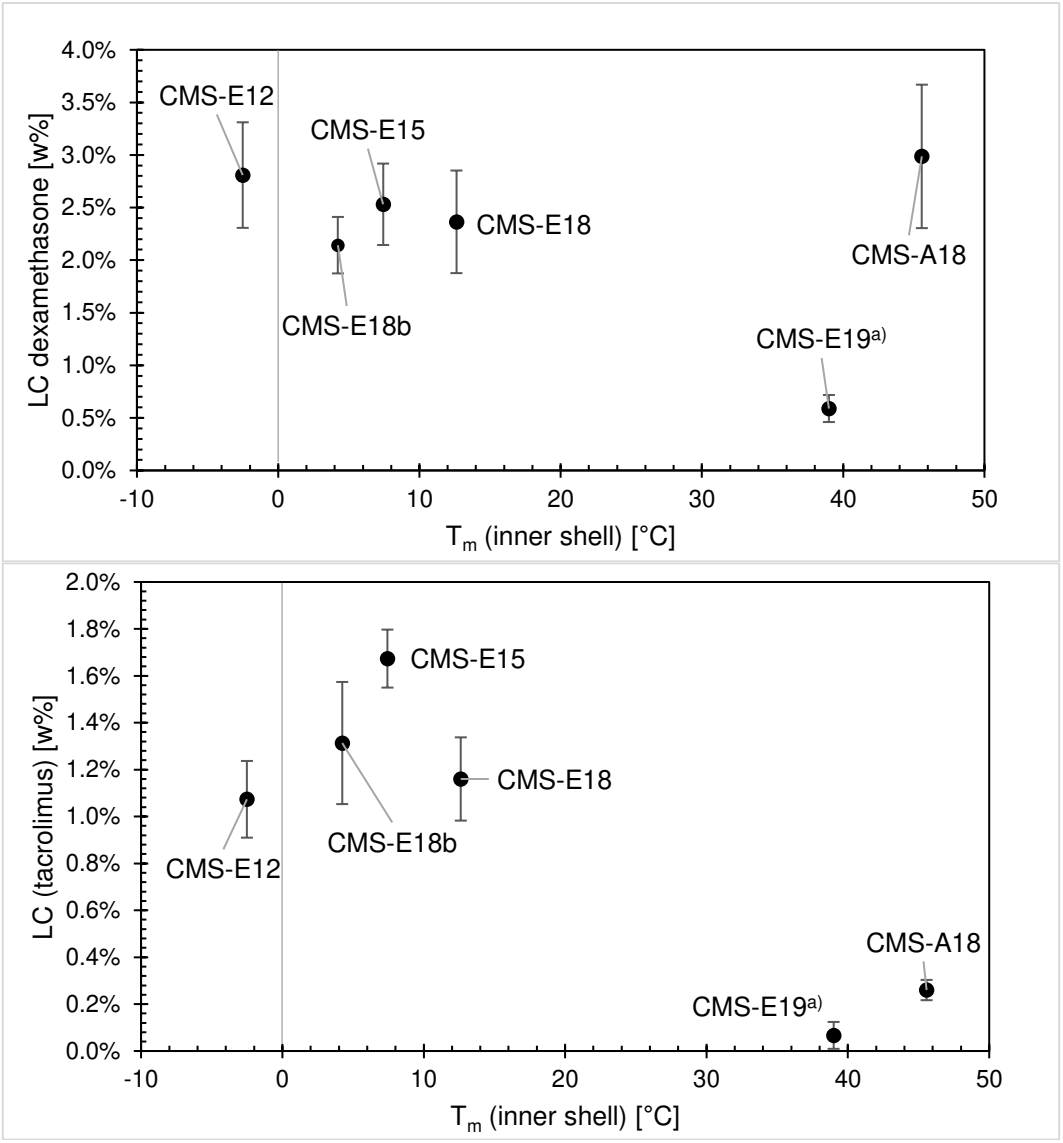

Figure S4. Loading capacities of the investigated carrier architectures for dexamethasone (top) and tacrolimus (bottom) plotted against the melting temperature of their respective inner shell. No correlation could be found. [a)]Encapsulation performed at 60 °C.

Table S4. Loading capacities of dexamethasone and tacrolimus.

compound	loading capacity dexamethasone [wt%]	loading capacity tacrolimus [wt%]
CMS-A18	3.0 ± 0.7	0.26 ± 0.1
CMS-E12	2.8 ± 0.5	1.1 ± 0.2
CMS-E15	2.5 ± 0.4	1.7 ± 0.1
CMS-E18	1.7 ± 0.5	1.16 ± 0.1
CMS-E19*	0.6 ± 0.1	0.07 ± 0.1
CMS-E18b	2.1 ± 0.3	1.3 ± 0.3

*measured at 60°C

5. Enzymatic degradation of CMS-E

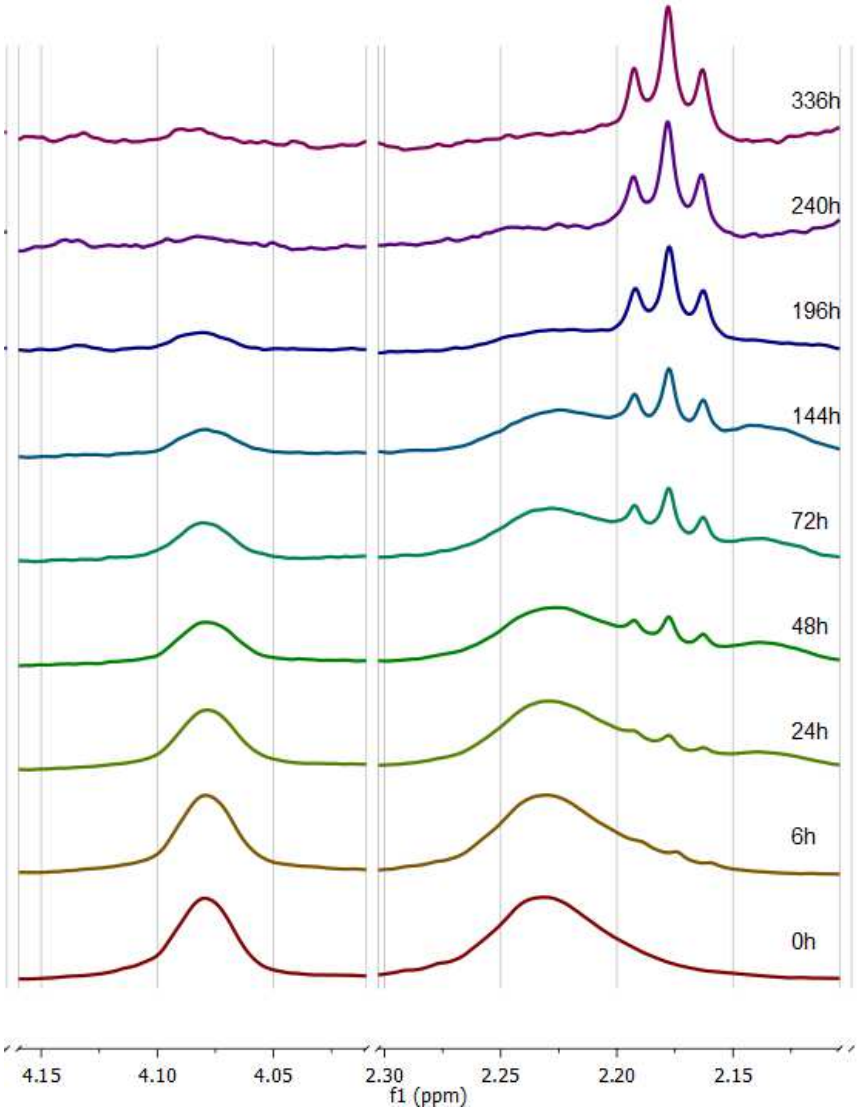

Figure S4. Relevant NMR signals for determining the rate of degradation in DMSO-d6: The signal at 4.07 ppm vanishes over time, indicating a cleavage of the inter-shell ester. The signal at 2.23 decreases

upon any ester cleavage and reappears either as a triplet at 2.18 ppm (cleavage of the inter-shell ester) or as a broad signal at 2.14 ppm (cleavage of core ester).

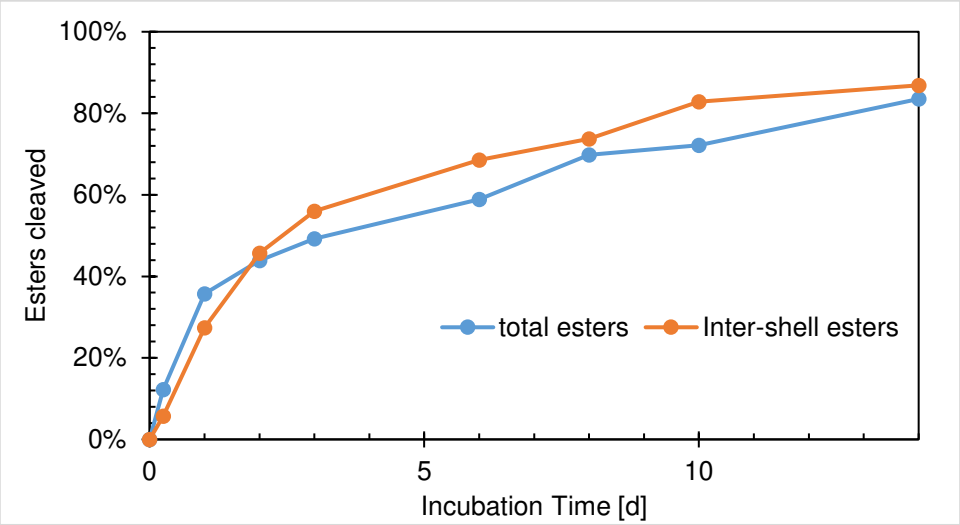

Figure S5. Degree of cleavage of total ester bonds (blue) and inter-shell ester bonds of CMS-E15 as determined by NMR (DMSO-d6).

6. Enzymatic degradation of CMS-A18

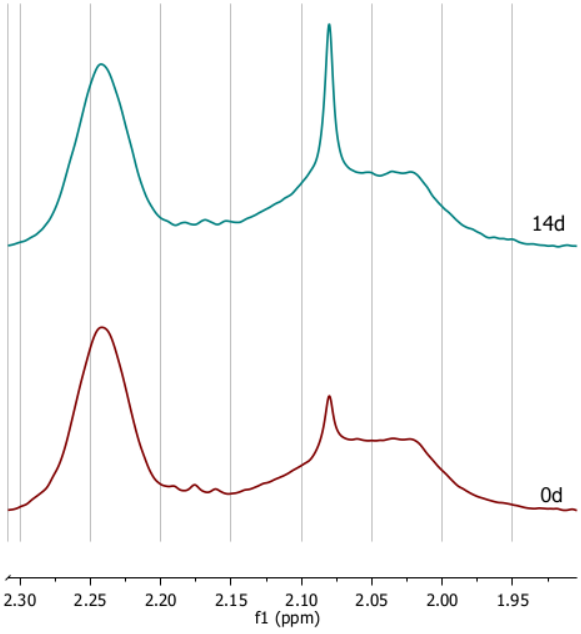

Figure S6. Comparison of the relevant peaks to determine the degree of degradation in DMSO-d6 at the start (bottom) and after 14 days (top): The peak at 2.24 ppm can be assigned to the ester α-protons and

the triplet at 2.18 ppm to the α-protons of the acid. The broad peak between 2.12 ppm and 1.97 ppm is assigned to the amide α-protons and is overlapped by an impurity at 2.08 ppm. There is no decrease of the amide or ester peaks over time in favor of the signal of the acid protons over time.

7. Release mediated by enzymatic cleavage

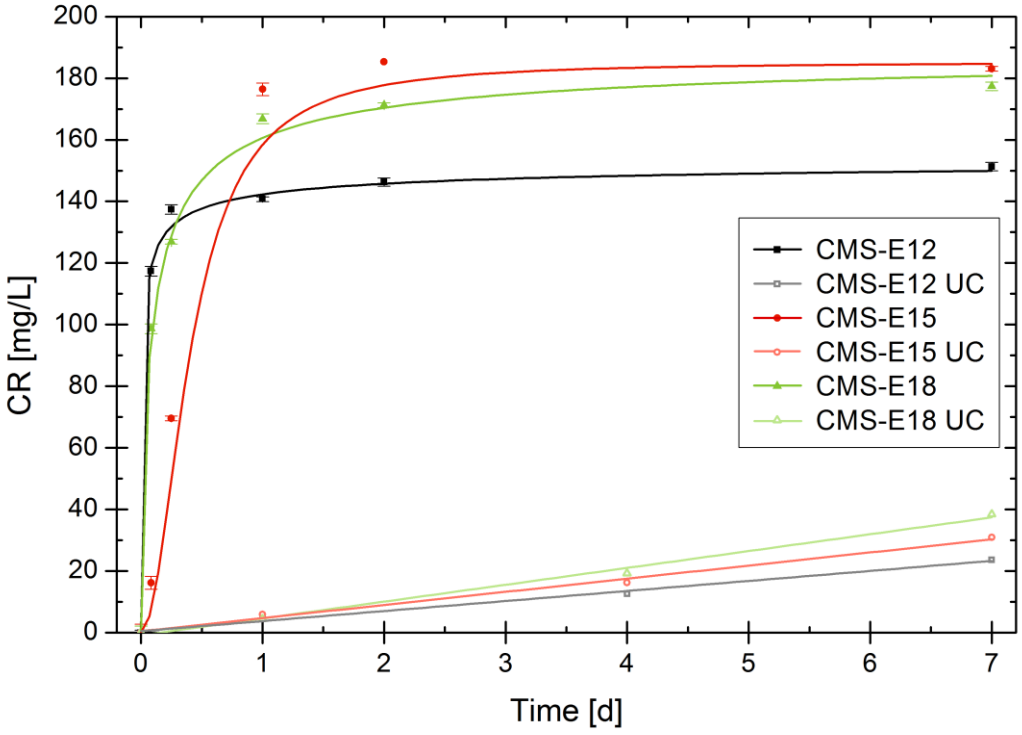

Figure S7. Cumulative Release (CR) of the absolute amounts of dexamethasone from the solutions of loaded carriers (polymer concentration 10 g/L) in comparison to the untreated control (UC) without enzyme, n=3.

3.2 Tailored dendritic core-multishell nanocarriers for efficient dermal drug delivery: A systematic top-down approach from synthesis to preclinical testing

This chapter was published in:

Stefan Hönzke, Christian Gerecke, Anja Elpelt, Nan Zhang, Michael Unbehauen, Vivian Kral, Emanuel Fleige, Florian Paulus, Rainer Haag, Monika Schäfer-Korting, Burkhard Kleuser, Sarah Hedtrich, Journal of Controlled Release 242 (2016) 50–63.

DOI: https://doi.org/10.1016/j.jconrel.2016.06.030

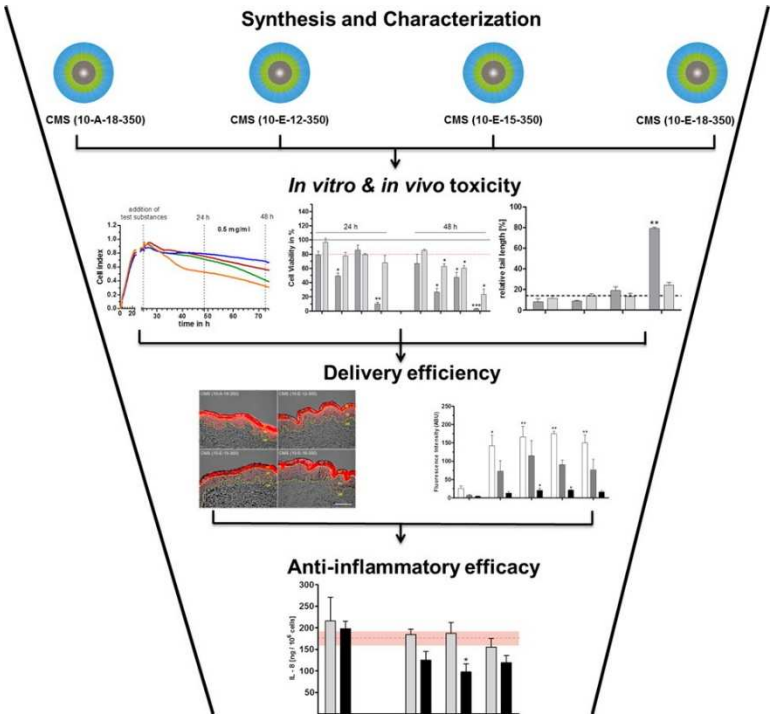

Author contributions:

- Synthesis of CMS nanocarrier CMS-E18 and building block C_{18}-PEG_{350},
- Loading of Nile red into CMS-E18 and CMS-A18 and determination of guest concentration
- Encapsulation of Dexamethasone into CMS-E18 and CMS-A18
- Writing and proof-reading of the manuscript

3.3 Characterization of hyperbranched core-multishell nanocarriers as an innovative drug delivery system for the application at the oral mucosa

This chapter was published in:

J. Jager, K. Obst, S. B. Lohan, J. Viktorov, S. Staufenbiel, H. Renz, M. Unbehauen, R. Haag, S. Hedtrich, C. Teutloff, M. C. Meinke, K. Danker, H. Dommisch, Journal of Periodontal Research 2018, 53, 57–65.

DOI: https://doi.org/10.1111/jre.12487

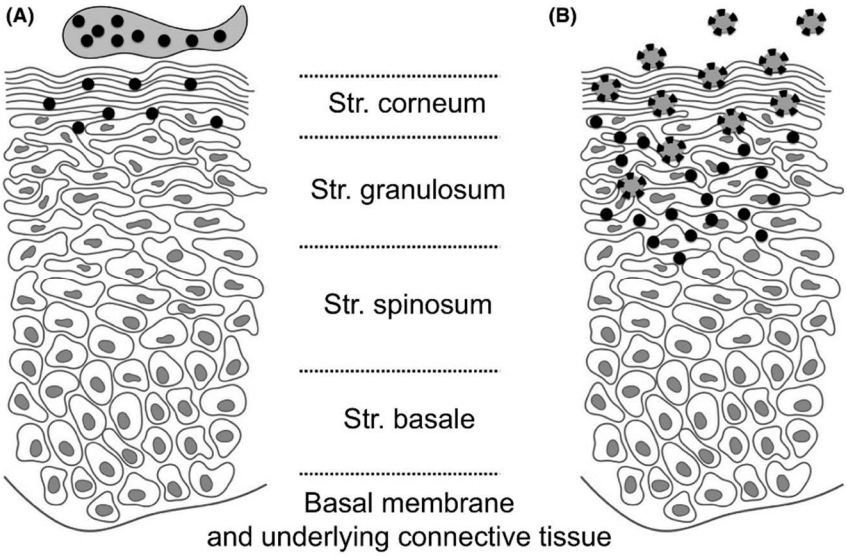

Reproduced with permission from John Wiley and Sons.

Author contributions:

- Synthesis of CMS-ICC and preparation of samples
- Spin-labeling of dexamethasone
- Loading of spin-labeled dexamethasone into CMS-E15 and characterization of samples
- Conception of experiments
- Writing and proof-reading of the manuscript

3.4 Anionic Core-multishell Nanocarriers for the Delivery of Analgesics to Inflamed Tissue

This chapter is the pre-print version of a journal article published in:

Michael L. Unbehauen, Dominika Łabuz, Richard Schwarzl, Sam Moré, Robert Bittl, Christoph Stein, Halina Machelska, Rainer Haag, Advanced Therapeutics. Copyright Wiley-VCH Verlag GmbH & Co. KGaA. Reproduced with permission.

DOI: 10.1002/adtp.201900007

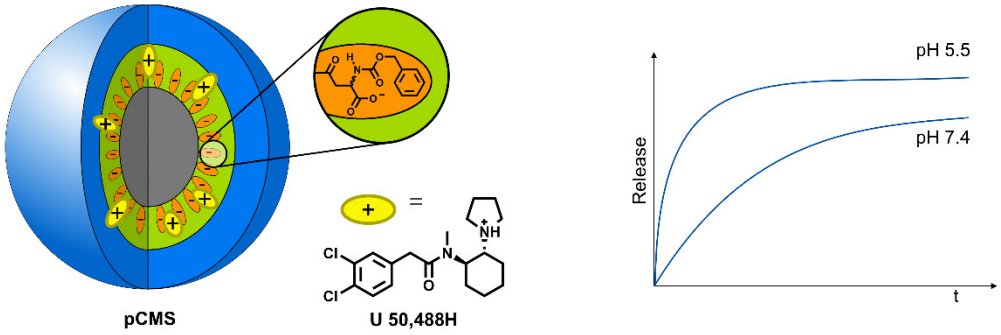

Author contributions:

- Synthesis of pCMS architectures
- Measurements of pH dependent ζ-potential and hydrodynamic radii
- Determination of loading capacity via HPLC
- Conception and realization of release experiments
- Preparation of samples for the *in vivo* studies
- Writing of the manuscript

Full paper

Anionic Core-multishell Nanocarriers for the Delivery of Analgesics to Inflamed Tissue

*Michael L. Unbehauen, Dominika Łabuz, Richard Schwarzl, Sam Moré, Robert Bittl, Christoph Stein, Halina Machelska, Rainer Haag**

Michael L. Unbehauen, Prof. Dr. Rainer Haag
Institute for Chemistry and Biochemistry, Freie Universität Berlin, Berlin, Germany
E-mail: haag@chemie.fu-berlin.de
Dr. Dominika Łabuz, Prof. Dr. Christoph Stein, Prof. Dr. Halina Machelska,
Charité – Universitätsmedizin Berlin, corporate member of Freie Universität Berlin, Humboldt-Universität zu Berlin, and Berlin Institute of Health, Department of Anesthesiology and Critical Care Medicine, Campus Benjamin Franklin, Berlin, Germany
Richard Schwarzl, Prof. Dr. Robert Bittl
Institute of Physics, Freie Universität Berlin, Berlin, Germany
Dr. Sam Moré
DendroPharm GmbH, Arnimallee 14, 14195 Berlin, Germany

U 50,488H (U50) is a κ-opioid receptor agonist exerting effective analgesia in animal pain models. Yet, side effects such as sedation and depression-like symptoms mediated in the brain limit its therapeutic potential. In this study, we present tailor-made core-multishell nanocarriers containing U50 that, despite their small size, exhibit a pH-dependent retention effect via non-covalent interactions with the drug. The nanocarriers and their non-functionalized counterparts are characterized regarding their release properties *in vitro*, including a theoretical modeling of the release parameters. Finally, the U50-containing nanocarriers are tested *in vivo* in a rat model of inflammatory pain.

1. Introduction

Pain is the most common symptom for which patients seek medical treatment and it is a health problem of high socio-economic importance.[1,2] Current pain management relies on nonsteroidal anti-inflammatory drugs (NSAIDs) and opioids. NSAIDs are often ineffective in severe pain and limited by serious side effects, including gastrointestinal ulcers and bleeding, stroke and myocardial infarction.[3,4] Opioids are the strongest painkillers, which exert their action via three types of opioid receptors, μ, δ, and κ. The most widely used opioids include morphine and fentanyl, which act via μ receptors. However, in addition to pain relief, they

produce side effects such as sedation, constipation, respiratory depression, euphoria, misuse, and addiction, which resulted in the opioid crisis.[5–7] In contrast, κ-opioid receptor agonists lack the abuse potential of μ-opioids, which made them promising candidates for pain treatment. A prototypic κ-receptor selective agonist is U 50,488H (U50), which has been shown to exert effective analgesia in animal pain models. Nevertheless, due to the permeation of the blood-brain barrier (BBB), U50 and related compounds can produce psychotic effects (e.g., disorientation, confusion, hallucinations), sedation, and depression-like symptoms, mediated by κ-receptors in the brain.[8,9]

Importantly, apart from the brain, opioid receptors are also expressed in peripheral sensory neurons (nociceptors) innervating peripheral tissue (skin, muscles, joints, bones, viscera), and majority of painful syndromes are associated with such tissue inflammation, including postoperative, arthritis, neuropathic, and cancer pain. Under such conditions, the synthesis, signaling and agonist accessibility of opioid receptors in peripheral sensory neurons is increased. Additionally, functional opioid receptors are expressed in immune cells accumulating in injured tissue. As a result, locally applied opioids, including U50, in small, systemically inactive doses have been shown to produce effective analgesia devoid of centrally-mediated side effects.[10–15] Previous attempts to achieve the restriction of κ-agonists to peripheral opioid receptors included incorporation of quaternary or non-quaternary polar hydrophilic structures, moderate hydrophilic substituents, or amphiphilic molecules. However, these modifications often decreased agonist affinity to receptors, which required the use of relatively high doses and did not warrant complete BBB impermeability, and paradoxically enhanced pain in some cases.[8,13,16]

Particularly in recent years, formulations such as nanoparticles, nanocapsules, or nanofibers have gained much interest.[17,18] Materials used for these structures are usually polyesters like PCL, PLA, or PLGA, and contain the local anesthetic either incorporated directly, or, in the case of the nanocapsules, dissolved in an oily core surrounded by the polymer.[19–21] Thus, the mechanism of action usually involves erosion of the matrix material and diffusion of the drug out of the material.[22] Along with these nanostructures, liposomal formulations have been tested for the delivery of anesthetics. A structure inspired by the liposome is the so-called core-multishell (CMS) nanocarrier previously published by our group,[23] which consists of a hyperbranched polymer as a core to which amphiphilic chains are attached. This architecture has been proven to encapsulate and solubilize guest molecules and other nanoparticles in hydrophilic and hydrophobic solvents.[24] This encapsulation effect has also been used for the

transport of model drugs into skin and for the accumulation of the dye ITCC in tumor tissue via the enhanced permeability and retention (EPR) effect.[25,26] In the past years, this parent structure has been altered to include new materials and types of bonds used to construct CMS nanocarriers.[27–29] For example, hyperbranched polyglycerol and oligoesters were used in this architecture to reduce toxicity and enable cleavability and biodegradability. Furthermore, the CMS nanocarriers were subject to simulations regarding its structure, aggregation behavior, and release kinetics.[30,31] Also, the inner shell has been modified to transport copper ions across the BBB.[32] Similar to this approach, ionic interactions can be used to bind the pharmacophore to a nanoparticle. Examples here are photosensitizer or cis-platin-loaded PMMA nanoparticles and antioxidants loaded into functionalized hPG.[33–35]

In this paper, we describe the development of two nanocarrier architectures (see **Figure 1**) with a pH-sensitive binding patch suitable for the interaction with U50 based on ionic interactions, hydrogen bonds, and π-π stacking. The major goal was to obtain a U50-containing nanocarrier, which following intravenous (i.v.) injection produces analgesia exclusively in peripheral inflamed tissue. Importantly, inflammation is associated with angiogenesis, enhanced permeability of the vascular endothelium, and local tissue acidosis (low pH).[36,37] Thus, the rationale was that due to high molecular mass and pH-sensitivity, the U50-containing nanocarrier will not cross the BBB, but will be able to diffuse through the permeable vascular endothelium in inflamed tissue where in a pH-sensitive manner will liberate U50 to locally ameliorate pain. To this end, the potential of the patch-functionalized CMS (pCMS) nanocarriers were quantified regarding their loading capacity and retention which then was further analyzed in a mathematical model. Finally, the analgesic effects of the most promising U50-containing nanocarriers were evaluated in the clinically relevant model of inflammatory pain in rats.

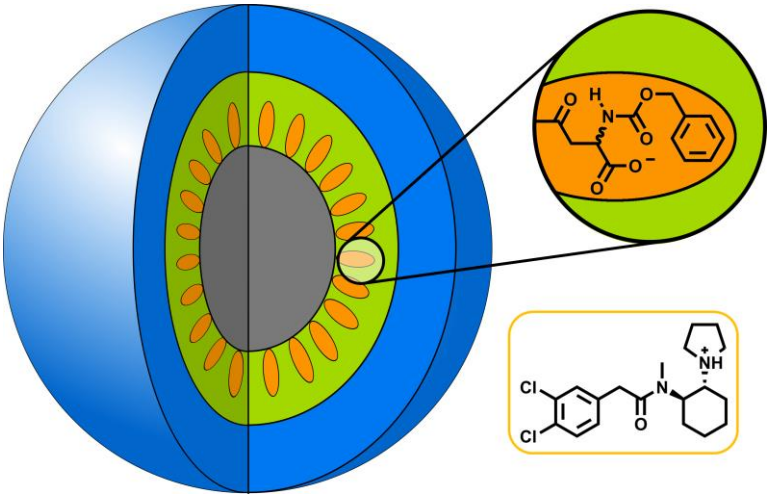

Figure 1. Schematic structure of the patch-functionalized core-multishell (pCMS) nanocarrier and the drug U50 in its protonated form.

2. Experimental Section

All chemicals were used as bought without any further purification. Polyethylene glycol monomethyl ether (mPEG) 350, (±)-trans-U-50488 methanesulfonate salt, N-Z-L-aspartic anhydride, N,N-diisopropylethylamine (DIPEA), methanol, and benzoylated dialysis tubing (2 kDa, 32 mm) were bought from Sigma-Aldrich, Munich, Germany. hPG (MW = 10 kDa), hPG-NH_2 (MW = 10 kDa, 70% amines), and CMS-A were produced by previously published methods.[27,38,39] CMS-E (brand name DendroSol®) and 15-methoxy poly(ethylene glycol)-15-oxo pentadecanoic acid ($mPEG_{350}$-C_{15}) were received from Dendropharm, Berlin, Germany.

Dry pyridine and dry DMSO were bought from Acros, Geel, Belgium and pyridine stored over calcium hydride (Acros). Dry DCM was taken from a solvent purification system (SPS-800) by MBRAUN (Stratham, NH, USA) and stored over a molecular sieve (4 Å, Roth). Acetonitrile HPLC gradient grade was bought from Fisher Scientific, Schwerthe, Germany. MilliQ water was taken from a Millipore Advantage A10 system (Merck) and thionyl chloride was purchased from Merck, Darmstadt, Germany.

Isolation of U50: Isolation of free-base U50 was performed by dissolving the respective methanesulfonate salt in water and adding a few drops of conc. aqueous ammonia. After centrifugation (4000 RPM, 10 min, Biofuge Primo, Heraeus, Hanau, Germany), the supernatant was taken off and the colorless solid dried under low pressure (< $0.5 \cdot 10^{-2}$ mbar) for several hours. The absence of methanesulfonate was proven via IR spectroscopy.

NMR spectroscopy: NMR spectra were recorded either on a Jeol Eclipse 500 MHz (Tokyo, Japan) or a Bruker AVANCE III 700 MHz spectrometer (Billerica, MA, USA). Proton and

carbon NMR were recorded in ppm and were referenced to the indicated solvents.[40] NMR data were reported including chemical shift, multiplicity (s = singlet, d = doublet, t = triplet, m = multiplet), integration, and coupling constants (s) in Hertz (Hz). Multiplets (m) were reported over the range (ppm) in which they appeared in the spectrum. All spectra were recorded at 300 K.

Dynamic Light Scattering (DLS): For the determination of hydrodynamic sizes, dynamic light scattering (DLS) measurements were performed on a Malvern Zetasizer Nano (Herrenberg, Germany) equipped with a laser at 532 nm using backscattering mode (detector angle 173°). The samples were filtered through 0.45 μm-regenerated cellulose syringe filters prior to DLS measurement and 100 μL of the resulting solution added to a disposable micro-cuvette. Autocorrelation functions were analyzed using Zetasizer DTS software (Malvern, Herrenberg, Germany) to determine the size distribution by intensity or number. The fraction (%) indicates the proportion of measured size relative to the total signal scattered by the CMS nanocarriers. For the pH-dependent measurements, a titrator was used. The initial pH was 11 and it was titrated with 1 M HCl. Measurements were performed at 25 °C.

Gel Permeation Chromatography: A Shimadzu (Kyoto, Japan) liquid chromatography (LC) system was employed for the gel permeation chromatography (GPC) measurements. Three PolarSil columns (PSS Polymer Standards Service GmbH, Germany; PolarSil 8 × 300 mm, 100 Å, 1000 Å, 3000 Å with 5 μm particle size) and a refractive index detector (RI) were used to separate and analyze polymer samples. As the mobile phase DMF (0.3 wt% LiBr and 0.6 wt% acetic acid) was used at a flow rate of 1 mL·min−1. Columns and RI detector were heated to 40 °C. The system was calibrated against polystyrene calibration standards (PSS, Germany). Samples were measured at a concentration of 10 mg·mL−1. LC solution software from Shimadzu was used for data analysis.

Film Encapsulation Method: The film uptake method was chosen for the encapsulation procedure. To form a film, 50 wt% of U50 488 free base was dissolved in a vial and the solvent removed on a rotavap. A stock solution of the respective CMS nanocarrier (5 mg·mL^{-1}) was filled onto the film and the suspension stirred for 22 h at room temperature. Excess guest was removed via filtration through a 450 nm regenerated cellulose syringe filter.

HPLC Analysis: The concentration of U50 was determined via high performance liquid chromatography (HPLC, Fertigsäule 125x4mm, RSC-Gel C18ec, 5µm, R. Sauerbrey Chromatographie, Reinhardshagen, Germany, acetonitrile/phosphate buffer 10 mM, pH 2.9

(35/65, v/v) using a UV detector set to λ = 232 nm. For the preparation of the sample, the samples were diluted 1:1 with a mixture of 70 vol% acetonitrile and 30 vol% phosphate buffer 43.3 mM, pH 2.9. Therefore the final sample had a solvent composition equal to the eluent.

Dialysis-based Release Kinetics: To obtain data for the release kinetics, 1 mL of a donor solution was filled inside a dialysis tube (Pur-A-Lyzer Maxi, MWCO 6000-8000 g mol^{-1}), which was placed in a reaction tube filled with 20 mL of stirred acceptor solution. At time points of 0, 1, 2, 4, 8, 24, and 48 h, 175 µL of the acceptor solution were transferred into a 96-well plate (UV-Star® half area, Greiner Bio-One, Germany). The concentration of U50 was determined in by UV-spectrometry in a plate reader (Tecan Infinite 200 PRO) at 232 nm using fresh acceptor solution as a blank. As acceptor media, phosphate buffer (pH 7.4) or acetate buffer (pH 5.5) was used, when indicated, sodium chloride was added. The donor solutions were prepared either by diluting the encapsulated U50 in several nanocarriers or by mixing solutions of U50 mesylate salt and the respective nanocarrier. The concentration of the drug was kept at 2.71 mM, which corresponds to 1 g L^{-1} mesylate salt. This resulted in nanocarrier concentrations of 5.5 g L^{-1} for CMS-E, pCMS-A and pCMS-E and 7.4 g L^{-1} for CMS-A.

Synthesis of $C_{18}mPEG_{350}$ and NHS-C_{18}-$mPEG_{350}$: The synthesis and the activation of this double-shell building block was performed as already described by our group.[41] In brief, an excess of 1,18-octdecandioic acid and methyl-polyethyleneglycol with a MW of 350 were heated up to 180 °C under low pressure ($0.5 \cdot 10^{-2}$ mbar) for 2h. Then, the reaction mixture was purified by hot filtration from toluene and the crude product by HPLC. The product was then activated to its NHS-ester by reacting it with NHS and DCC in THF overnight with subsequent purification by filtration in DCM.

Synthesis of pCMS-A: 10 mL of dry DMSO was added to hPG-NH_2 (130 mg, 1.04 mmol, 20 g L^{-1} stock solution in methanol) and the methanol was removed under low pressure (<$0.5 \cdot 10^{-2}$ mbar) to give a clear, slightly yellow solution. DIPEA (47.6 mg, 62.7 µL) was added and the solution heated to 50°C. N-Z-L-aspartic anhydride (61.2 mg, 0.25 mmol) was dissolved in 5 mL of dry DMSO and added dropwise. The reaction was left at 50°C for 2 hours. A sample of 2.3 mL (hPG-NH-AA) was taken and dialyzed against water (1L, 3 changes of dialysate) and methanol (1L, 2 changes). Then the solvent was exchanged to D_2O by repetitive partial removal of solvent, addition of D_2O, and measurement of an NMR spectrum until the disappearance of the methanol signal. This spectrum was then used to determine the degree of functionalization.

Then, NHS-C_{18}-PEG_{350} (849 mg, 1.14 mmol) in 5 mL of dry DMSO was added and the reaction mixture stirred overnight. The next morning, the solution was dialyzed against methanol (4x2 L, 2 kDa). Then, the solvent was removed to yield a slightly brown film (456.2 mg, yield = 83%).

^{1}H NMR: hPG-NH-AA (500 MHz, D_2O) 8.14 (m, -N*H*-CO-, 0.18H), 7.44 (m, aromat. H, 0.9H), 5.17 (m, Ph-C*H*$_2$-, 0.36H), 4.50-2.90 (hPG backbone, 5H), 2.88-2.43 (-OC-CHNR-C*H*$_2$-CO-, 0.36H); pCMS-A (700 MHz, methanol-d4, TMS): δ (ppm) = 8.13 (m, -N*H*-CO-, 0.7H), 7.35 (m, aromat. H, 0.9H), 5.09 (s (br), Ph-C*H*$_2$-, 0.36H), 4.21 (s, –C*H*$_2$–OCO–, 1.04H), 4.56–3.39 (m, mPEG repeating unit, hPG backbone and -OC-CHNR-C*H*$_2$-CO-, 19.3H), 3.36 (s, –O–C*H*$_3$, 1.56H), 2.33 (m, 1.04H, –C*H*$_2$–CONH–), 2.23 (m, 1.04H, –C*H*$_2$–COO–), 1.61 (m, 2.08H, –C*H*$_2$–CH$_2$–CO–), 1.31 (m, 12.48H, –(C*H*$_2$)$_{12}$–).

^{13}C NMR: hPG-NH-AA (176.09 MHz, D_2O): δ (ppm) = 171.0, 129.3-127.5, 72.9-65.9; pCMS-A (176.09 MHz, methanol-d4): δ (ppm) = 176.3, 175.2, 129.9-128.9, 73.0, 72.2-71.3, 70.2, 64.6, 59.2, 37.3, 35.06, 31.4-30.0, 27.2, 26.2

Synthesis of pCMS-E: hPG (67.3 mg, 0.91 mmol) was dried by dissolving it in 1 mL of dry pyridine in a Schlenk flask and removing the solvent under low pressure ($0.5 \cdot 10^{-2}$ mbar) three times. Then, it was dissolved in 10 mL of dry pyridine, and N-Z-L-aspartic anhydride (45.3 mg, 0.18 mmol) was added. The solution was stirred overnight at RT. Then, 1 mL was taken and the solvent removed under low pressure. It was redissolved in deuterated methanol and an NMR sample was submitted to determine the degree of functionalization of the anchor molecule on the hPG core. A three-neck flask was then equipped with a reflux-cooler (center), an olive, and a septum. The olive was used for the additional cryotrap and a three-way faucet for ventilation in between. To the reflux cooler, a device with two faucets was attached, one connected to an Ar inlet, another one employed as an outlet leading to a gas washing bottle containing 1 M NaOH. In this setup, C_{15}-$mPEG_{350}$ (1035 mg, 1.66 mmol, previously dried under HV overnight) was dissolved in 3.5 mL of dry dichloromethane. Thionyl chloride (300 µL, 2.5 mmol) was then added at 0°C, the temperature kept for another 5 min and then refluxed for 1.5 hours. Thionyl chloride and dichloromethane were evaporated *in vacuo* and 5 mL of dry DCM was added and the solution cooled to 0°C. Dry pyridine (6 mL) was added to the hPG and the solutions cooled down to 0°C. Upon rapid stirring, the diluted solution of Cl-C_{15}-PEG_{350} in DCM was added drop-wise and the reaction mixture stirred overnight. The

solvent was evaporated and the crude product redissolved in 10 mL of methanol and subsequently dialyzed against methanol (3x2 L) yielding the product as a viscous oil (463.8 mg, 86% yield).

^{1}H NMR: hPG-NH-AA (500 MHz, methanol-d4) 7.35 (m, aromat. *H*, 0.9H), 5.10 (m, Ph-C*H*$_2$-, 0.36H), 4.70-3.4 (hPG backbone, -OOC-C*H*NR-CH$_2$-COO-, 5.18H), 2.87 (m, -OC-CHNR-C*H*$_2$-CO-, 0.36H); pCMS-E (700 MHz, methanol-d4): δ (ppm) = 7.38 (m, aromat. H, 0.9H), 5.12 (m, Ph-C*H*$_2$-, 0.36H), 4.72-4.59, (m, -OOC-C*H*NR-CH$_2$-COO-, 0.18H) 4.21 (s, –C*H*$_2$–OCO–, 1.62H), 4.50–3.39 (m, mPEG repeating unit, hPG backbone, 27.1H), 3.36 (s, –O–C*H*$_3$, 2.43H), 3.04-2.81 (m, -OOC-CHNR-C*H*$_2$-COO-, 9.36H) 2.34 (m, 1.62H, –C*H*$_2$–COO–), 1.62 (m, 3.24H, –C*H*$_2$–CH$_2$–CO–), 1.32 (m, 14.6H, –(C*H*$_2$)$_9$–).

^{13}C NMR: hPG-AA (125.77 MHz, methanol-d4): δ (ppm) = 129.8-128.6, 74.3-72.0; pCMS-A (176.09 MHz, methanol-d4): δ (ppm) = 175.1, 174.5, 129.7,129.2, 73.0, 71.6, 71.4, 70.2, 64.6, 59.2, 35.1, 31.3-30.1, 26.2.

Animals: All experiments were approved by the State animal care committee (Landesamt für Gesundheit und Soziales, Berlin) and performed according to the ARRIVE guidelines.[42] Male Wistar rats (250-300 g; Janvier Laboratories, France) were kept on a 12 h light/dark schedule, in groups of two in cages lined with ground corncob bedding, with free access to standard laboratory food and tap water. Room temperature was 22 ± 0.5°C and humidity 60-65%. Rats were handled once per day for 1-2 min, starting 4 days prior to experiments. After completion of experiments, animals were killed with an overdose of isoflurane (AbbVie, Germany). All efforts were made to minimize animal numbers and their suffering.

Inflammatory Pain Model: Rats received an intraplantar (i.pl.) injection of a complete Freund's adjuvant (CFA; 150 µl; Calbiochem, La Jolla, CA, USA) into the right hind paw under brief isoflurane anesthesia.[43] Experiments were performed at 4 days after inoculation with CFA.

Mechanical Hyperalgesia (Paw Pressure Test): Rats were gently restrained under paper wadding and incremental pressure was applied via a wedge-shaped, blunt piston onto the dorsal surface of the hind paws by means of an automated gauge (Ugo Basile, Comerio, Italy), as previously.[37,44] The paw pressure threshold (cut-off at 250 g) required to elicit paw withdrawal was determined by averaging three consecutive trials separated by 15-s intervals. The sequence of paws was alternated between animals to avoid order effect.

Drugs and Experimental Plan: Rats received injection (1 ml) into the tail vein of U50 (1-10 mg kg^{-1}), U50@CMS-E and U50@pCMS-E (both at 5-50 mg kg^{-1} polymer and 1-10 mg kg^{-1} U50) under brief, general isoflurane anaesthesia. U50 was dissolved in sterile water, whereas U50@CMS-E and U50@pCMS-E were dissolved in PBS. Control groups were treated with empty (without U50) CMS-E or pCMS-E (both at 50 mg kg^{-1}, i.e., equivalent of carrier containing 10 mg kg^{-1} U50) dissolved in PBS. To obtain final concentrations, all substances were diluted with 0.9% NaCl. Each group consisted of 8 rats. To reduce the number of animals, one control group was used for all treatments, which consisted of four rats treated with empty CMS-E and the other four rats with empty pCMS-E. There were no differences between the two treatments. Nociceptive thresholds were evaluated before and 10-60 min following injections. The doses of all agonists were determined in pilot experiments. The experimenter was blind to the drugs and their doses. A colleague not involved in experiments prepared each substance/dose in coded, separate vials (one per animal), which allowed randomization and blinding. The codes were broken after experiment completion.

Statistical Analyses: For *in vivo* behavioral experiments, the animal numbers were estimated *a priori* using the G*Power 3.1.2 program, under consideration of α of 5%, power of 80%, variance of 25%, and the biologically relevant difference of 50%, which resulted in 8 animals per group. The data are expressed in raw values and AUC, and were assessed for normal distribution and equal variances by the D'Agostino-Pearson test. Two-sample comparisons were made using Wilcoxon test. Two-way repeated measures analysis of variance (ANOVA) and the Bonferroni test were used to compare two groups over time. The AUC values were obtained by calculating the area between the X-axis and the curve of the PPT time course from the baseline to 60 min after each treatment (control, and each dose of U50, U50+CMS-E, and U50+pCMS-E). The AUC data were analyzed by Kruskal-Wallis one-way ANOVA followed by the Dunn's test. Differences were considered significant if $P < 0.05$. Prism 5 (GraphPad, San Diego, USA) was used for all statistical tests and all data were expressed as means ± standard error of the mean (SEM).

3. Results

3.1. Synthesis of the functionalized nanocarriers

To obtain modified CMS nanocarriers, the syntheses of two previously published CMS nanocarriers were modified (See Scheme 1).[27,41] In the initial syntheses, the diacid was reacted first with the PEG outer shell before the double shell was attached to the core. Into this strategy, an intermediate step was inserted. Before the attachment of the shell, the core was

functionalized with a Z-protected aspartic acid. In the case of pCMS-E, this could be achieved via the addition of the respective anhydride to hPG in pyridine. For the amide-based nanotransporter pCMS-A, a zwitterionic nanoparticle with a low solubility was the result of this functionalization. To prevent precipitation, the non-nucleophilic base diisopropylethylamine (DIPEA) was added and the temperature increased to 50 °C. DIPEA acted as a proton interceptor and ensured the negative charge of the functionalized core as well as the nucleophilicity of the amine functions, which was necessary for the subsequent reaction with the activated NHS-ester shell.

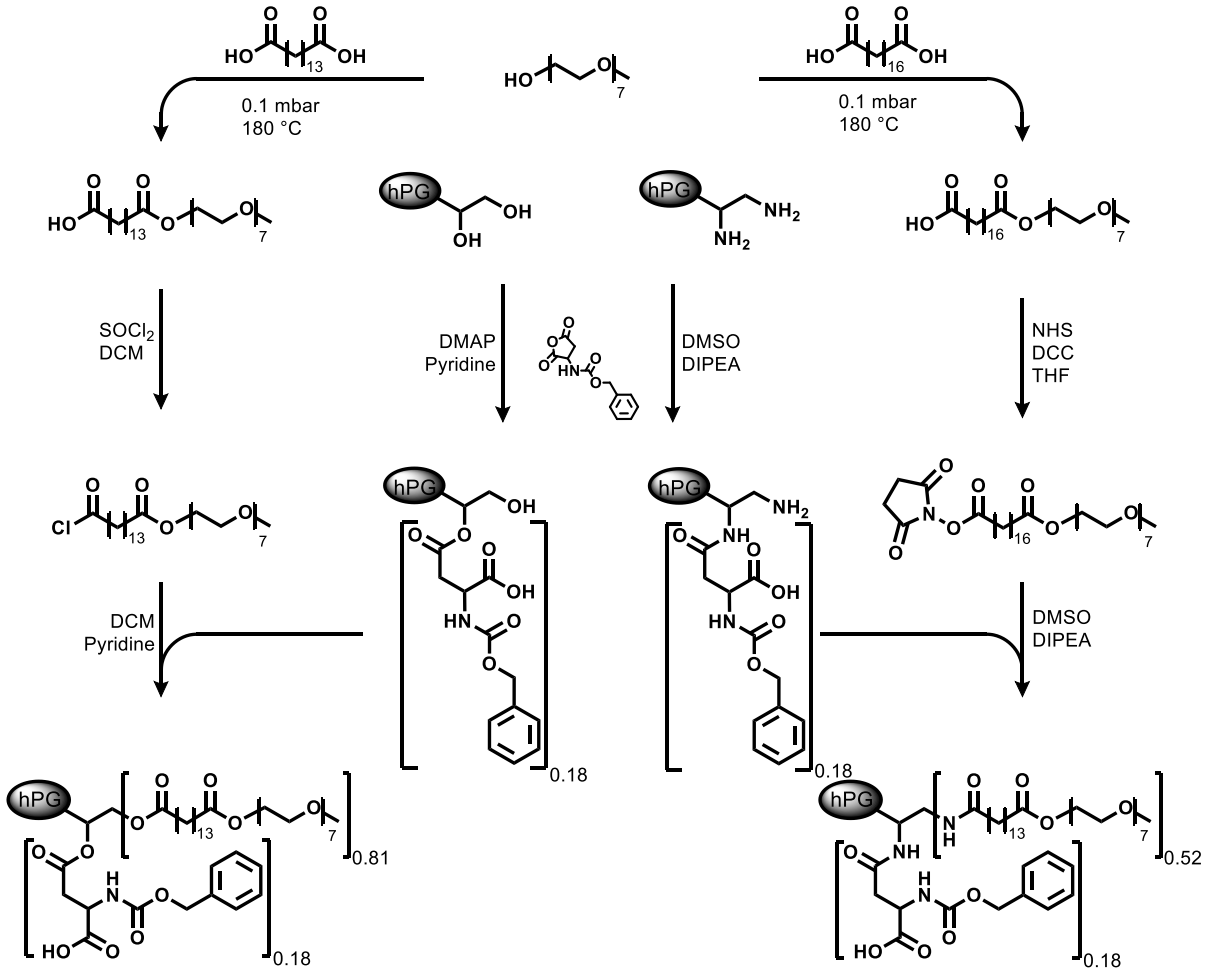

Scheme 1. Synthesis of aspartic acid-modified nanocarriers.

The degree of functionalization (DF) was determined via the quantitative analysis of ^{1}H-NMR integrals with the typical accuracy in the range of 5%. In the case of the unfunctionalized CMS-nanocarriers, this was done by comparing the aliphatic signal of the inner shell to the combined signal of the PEG/hPG-backbone as previously described.[45] In the case of pCMS, the DF for the anchor molecule AA was calculated by first relating the signals assigned to the aromatic protons to the integral of the signals originating to the hPG backbone. As a second step, the

aromatic integral was used as a reference for the signal of the aliphatic protons in the inner shell. The obtained values are compiled in Table 1. All the carriers exhibited a high degree of total functionalization while the percentage to which the aspartic acid was attached was equal in both functionalized carriers. The M_n was determined by GPC analysis against a linear standard. This comparison leads to a smaller molecular mass of the CMS nanotransporters than expected from the NMR data.

Table 1. Degree of functionalization determined by NMR spectroscopy and molecular weights determined by GPC analysis.

Nanocarrier	DF AA	DF shell	DF total	*Mn*	PDI
CMS-E	-	90%	90%	43.1	1.8
pCMS-E	18%	81%	99%	19.9	1.5
CMS-A	-	70%	70%	26.6	1.1
pCMS-A	18%	52%	70%	29.7	2.1

The chemical structure of the potent analgesic U50 contains a tertiary amine functionality (see **Figure 2**). To remove any salts that might interfere with the ionic interaction between CMS nanocarrier and U50, it was transferred into its respective base by basic precipitation with aqueous ammonia (see experimental). The free base of U50 was then used for encapsulation experiments into different CMS-nanocarrier types via the film uptake method. In this procedure, a film was prepared by adding stock solution of the guest molecule in an organic solvent into a vial, followed by subsequent evaporation. Then a nanocarrier solution was added on top of the film and the mixture stirred for 22 h. Excess guest was removed via filtration.

The concentration of U50 in solution was then determined via HPLC, the loading capacities (LC) and encapsulation efficiencies (EE) are plotted in **Figure 2**. While the LC describes the mass ratio between encapsulated guest (w_{guest}) and polymer ($w_{polymer}$, Equation 1), the EE relates the amount of the guest that has been encapsulated (w_{guest}) to the amount of drug in the feed (w_{feed}) (see Equation 2).

$$LC = \frac{w(guest)}{w(carrier)} \quad (1)$$

$$EE = \frac{w(guest)}{w(guest,feed)} \quad (2)$$

The results indicated that all tested carriers increased the solubility of the U50 free base by at least a factor of ten. Furthermore, comparing the two amide-based carriers, it becomes evident that attaching an additional anchoring point is beneficial for the loading of U50. At a feed of 16%, the encapsulation efficiencies are rather high (between 60 and 90%), which indicates that the loading in the nanocarriers had not reached its saturation. This is in accordance with the data at 48 wt% of drug in the feed. The loading of all nanocarriers increased when the feed was raised from 16 to 48 wt%. Especially the pCMS nanotransporters showed a trend towards higher loading. These data indicate that the ester-bond was beneficial for the solubilization of the hydrophobic U50 free base and the additional binding patch increased the loading even further.

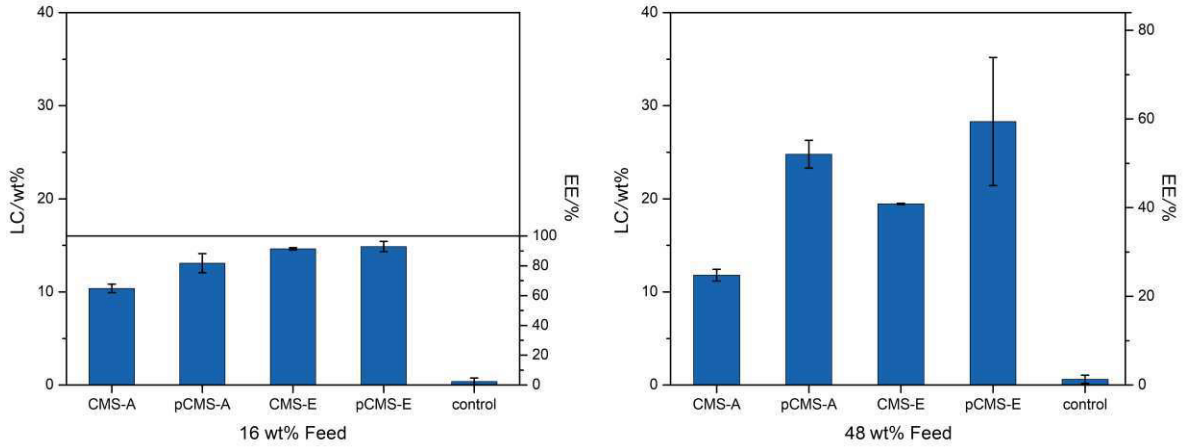

Figure 2. Loading capacities (LC) as well as encapsulation efficiencies (EE) of U50 in the different carrier architectures. Error bars represent SD, *n*=3.

3.2. pH-dependent size and ζ-potential

In contrast to the neutral unfunctionalized CMS nanotransporters, the additional binding site can bear a charge due to the deprotonation of the acid group. To determine the pH-dependent behavior, the functionalized particles were dissolved in 1 mM NaOH (pH≈11) and titrated with 1 M HCl. Both, hydrodynamic radius and ζ-potential were determined at different pH values (**Figure 3**). Furthermore, the apparent pKa (pK_{app}) of the functional group was determined. As expected, the pCMS-E exhibits a neutral ζ-potential at a pH below 4. At higher pH values, between 4 and 7, the carboxylic acid of the functional group is gradually deprotonated, which results in a negative surface-charge of the particle at a basic pH. The apparent pK_{app} of this nanocarrier is determined to be at 5.4. At higher pH values, the nanocarriers are in a charged state, resulting in separate, single particles of a hydrodynamic radius of around 10 nm, which corresponds to the values reported in literature.[45] Below that value, the nanocarriers begin to

form aggregates of 10 to 50 nm due to the lack of electrostatic repulsion. pCMS-A shows a very similar behavior regarding pH dependence. The particles are negatively charged at pH-values above the pK_{app} and neutral below. In the same way, the particles aggregate in neutral state and deaggregate when deprotonated. One significant difference between the systems is the pK_{app}. It was higher in the case of pCMS-E than in the case of pCMS (4.4). The second difference is the presence of a second protonation step at a pK_{app} of 9.6, which indicated some unreacted free amines at the hPG amine core. Accordingly, the nanoparticle was not neutral at a pH below the pK_{app}, but had a slightly positive charge.

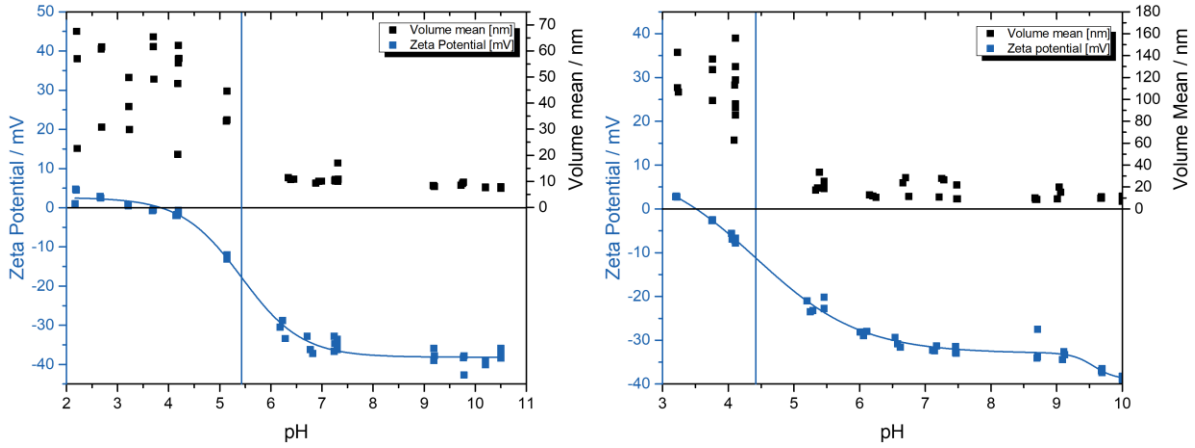

Figure 3. pH-dependent hydrodynamic radii and zeta potential of the functionalized, ester-based (left) and amide-based (right) carrier measurements were started at a conc. of 1 g L^{-1}. See experimental section for more details.

3.3. Release kinetics of U50 from different nanocarriers

After having estimated the surplus value of the patch moieties regarding loading capacity, its role for a retention of U50 by the nanocarrier was determined. To measure this, a dialysis-based setup was used. A Pur-A-Lyzer dialysis container filled with donor solution was placed inside a reaction tube filled with 20 mL receptor medium. Then, samples were taken at different time points and the concentration determined via UV/Vis spectrometry. A simplified version (see Equations S1 and S2) of the theoretical model published earlier was used to fit the obtained data.[31] The fitting functions are plotted together with the original data in Figure 4, 5 and S3. In **Figure 4** the release of U50 from either of the four nanocarrier architectures or as a mesylate salt is depicted. The data indicate that, as expected, the release without the presence of any carrier (Figure 4 left and right, black curve) was the fastest. Compared to that, the release from CMS-A only seemed to feature a weak retention effect, as the blue curve (Figure 4, right) did not differ from the black one very strongly and the error bars partially overlapped. The curves of all other carriers showed a strong difference from the curve without carrier, especially at

time points of only a few hours. While the ester-based carrier without binding patch (Figure 4 left, blue curve) showed some retaining behavior, the retention was increased by the binding patch (Figure 4 left, green curve). The highest effect was found for the carrier pCMS-A. Here the binding patch affects the affinity of U50 to the nanoparticle the most.

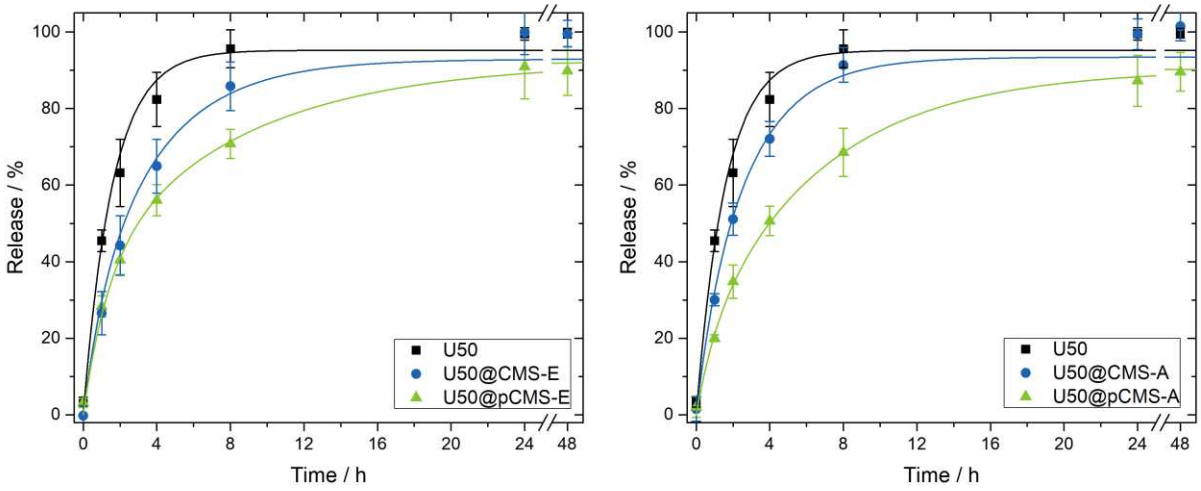

Figure 4. Release kinetics of U50 from functionalized and non-functionalized ester-based (left) and amide-based (right) nanocarriers at pH 7.4 (error bars represent SD, *n*=3).

As already shown in Figure 3, the binding patch caused the nanocarrier to exhibit a pH-dependent ζ-potential. To examine the influence of this effect on the release rate, the release experiment was repeated under various conditions. Along with the systemic pH, release studies from the nanocarrier architectures were performed at pH 5.5 (see **Figure 5**), which lay in the range of inflamed tissue. [44,46,47] Without any carrier (black and blue curves, Figure 5, left and right) there was no difference between pH 7.4 and 5.5. On the left, release without the presence of a nanocarrier is compared to the drug loaded into pCMS-E, on the right to pCMS-A. In this experiment, pCMS-A exhibited a retention effect at pH 7.4, but with an even lower pH of 5.5 this effect persisted within the range of error. In contrast, pCMS-E (left, green and orange curves) shows pH dependent behavior. The release at pH 7.4 was slower than at pH 5.5, without the overlap of the error bars at the data points of 1 h, 4 h, and 8 h. This indicates that protonation of the nanocarriers reduced the affinity towards the U50 and facilitated an enhanced release. To achieve a better understanding of why of two chemically similar carriers only one exhibited a pH-responsive release, we have to take a closer look at Figure 3. From these graphs, it becomes evident that pCMS-E has a ζ-potential of -38 mV at a pH of 7.4 and this changes to -19 mV at a pH of 5.5. In contrast, the ζ-potential of pCMS-A is around -32 mV at systemic pH and changes only marginally to -24 mV at 5.5. This rather small change of 8 mV (pCMS-A)

compared to 19 mV (pCMS-E) is reflected in the binding affinity and indicates the importance of electrostatic binding in this system.

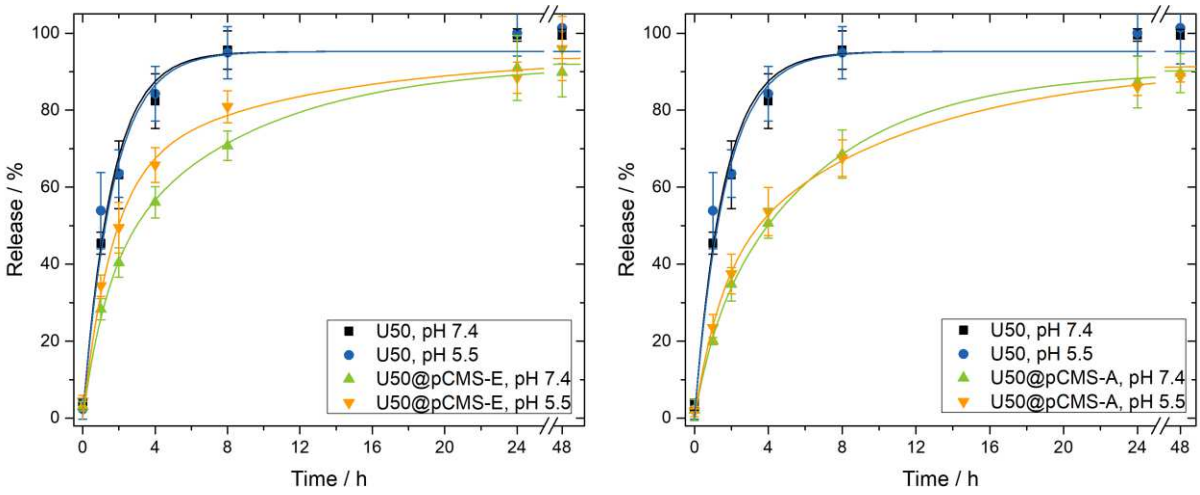

Figure 5. Release kinetics of U50 from the functionalized ester-based (left) and amide-based (right) nanocarriers (error bars represent SD, *n*=3).

As electrostatic interactions play an important role in this setup, it was elucidated if other parameters than pH interfere with these interactions. The two parameters that were chosen for this experiment were physiological salt concentration and the usage of the mesylate of U50 co-dissolved with the nanocarriers instead of the free base encapsulated into them. The results of these experiments are depicted in **Figure S3**. On the left, the release kinetics of U50 mesylate salt without a carrier are compared with the ones of the free base encapsulated into pCMS-E and the mixture of mesylate salt and pCMS-E. As already shown, the encapsulated drug was retained by the nanocarrier and its release rate lowered. No different behavior was found for the sample of co-dissolved U50 mesylate and pCMS-E within the range of error. This result indicates that the mesylate counterions did not disturb the attractive interactions in a measurable way.

The diagram on the right side of Figure S3 depicts the release behavior of U50 as a free drug in the presence of a NaCl concentration similar to the physiological one and encapsulated into pCMS-E with and without physiological salt. As shown already in Figure 4, pCMS-E retained the drug within the dialysis bag and lowered the release rate. The data indicate that in the presence of NaCl in physiological concentration, the release behavior was not altered. Thus, at this concentration, NaCl did not have a release-promoting effect.

Using the fitting functions, the effectiveness of the different carriers over the course of time could be visualized. To achieve this, Equation S3 was used, which related the amount of

released U50 from a nanocarrier to the respective amount in the control experiment. The results are plotted in Fig. S5 and indicate that in most carriers under various conditions, the observed effect lasts in the range of 4 to 12 h, which is in the necessary range for the animal experiments. Furthermore, the fitting functions were used to extract the RT_{50}-value (see SI). This value is the necessary time for 50% of the drug to enter the acceptor compartment (see also Eqation S5), which reduces a release experiment to one single value. The RT_{50} was calculated for all carriers and conditions investigated and plotted in Fig. S6, which nicely summarizes all carriers and conditions investigated in the release studies. This comparison indicates a low value for release experiments without carrier (1-1.5 h), while those with unfunctionalized nanocarriers (CMS-A and CMS-E) exhibited a value around 2 h. The usage of patch nanocarriers (pCMS) however led to much higher RT_{50} values (3-4 h), because of these nanocarriers' retention. The only exception to this was pCMS-E at a pH 5.5, which featured an RT_{50} similar to the unfunctionalized carriers. This indicates once more that the beneficial properties of the additional functionalization were lost due to the lowered pH and thus enhanced release under these conditions was facilitated. For this reason, we chose pCMS-E to be the nanocarrier to be tested *in vivo* in the inflammatory pain model.

3.4. Effects of intravenous U50, U50+CMS-E, and U50+pCMS-E on inflammatory pain

Four days after induction of unilateral hindpaw inflammation, rats developed mechanical hyperalgesia (reduced paw pressure threshold, PPT) in inflamed compared to contralateral, non-inflamed paws (**Figure 6**). Intravenous injection of U50 (1-10 mg kg^{-1}), U50+CMS-E and U50+pCMS-E (5-50 mg kg^{-1} polymer, and 1-10 mg kg^{-1} U50) significantly elevated PPT in inflamed paws compared to control treatment (empty CMS-E or pCMS-E; 50 mg kg^{-1}, i.e., equivalent amount of carrier containing 10 mg kg^{-1} U50). The analgesic effects peaked at 10 min and, in case of the highest, most effective dose, remained significantly increased until 45-60 min following injection (Figure 6, left panel). At the two highest doses, all agonists significantly increased PPT also in contralateral, non-inflamed paws with the peak effect at 10-15 min, and returned to baseline levels at 30-60 min (Figure 6, right panel). Control empty carriers did not significantly alter PPT either in inflamed or non-inflamed paws (Figure 6).

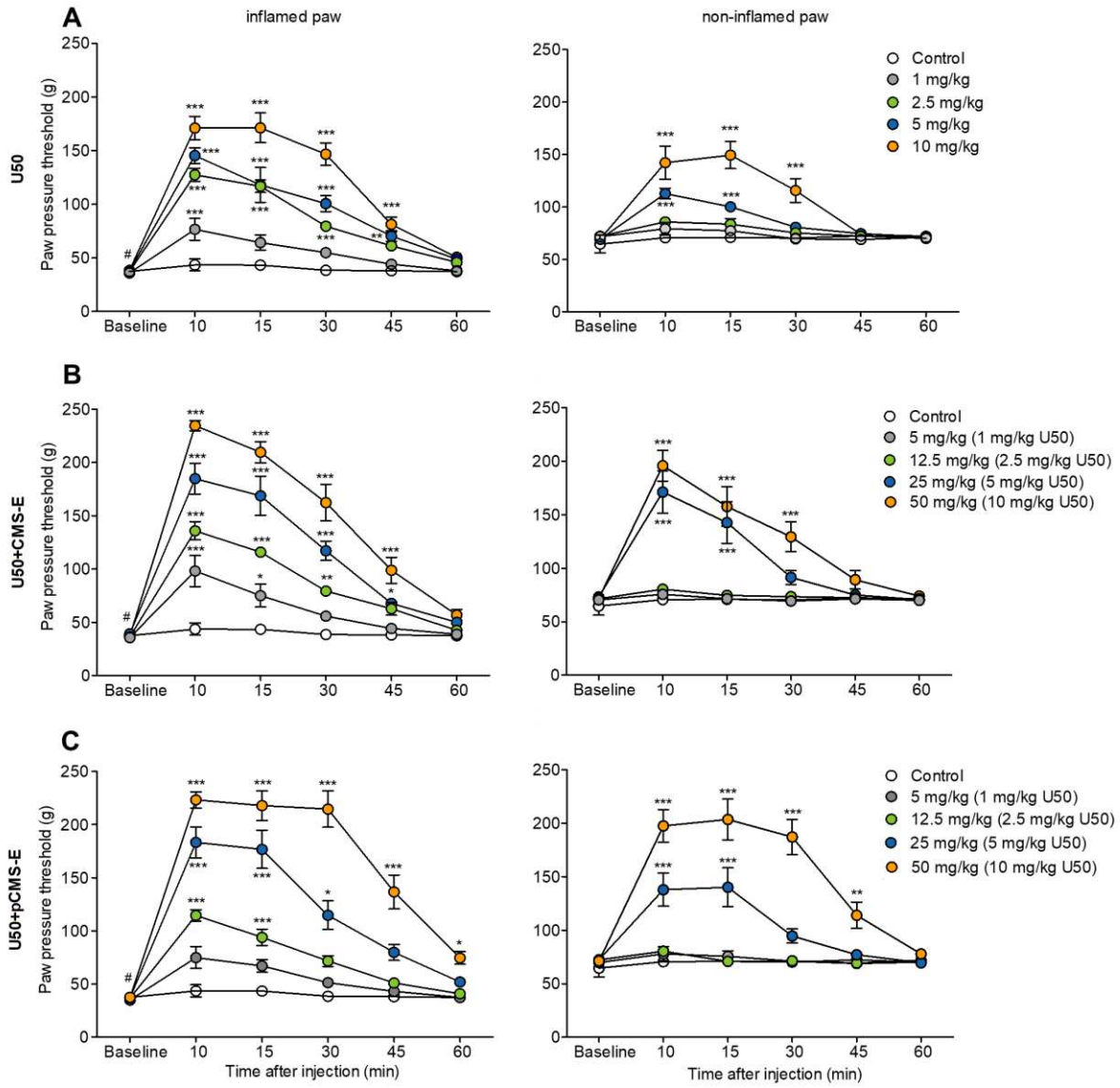

Figure 6. Analgesic effects after intravenous injection of U50 (A), U50+CMS-E (B) and U50+pCMS-E (C) in rats with unilateral hind paw inflammation. The effects on mechanical pain thresholds in inflamed (left panel) and contralateral, non-inflamed (right panel) hind paws were measured using the paw pressure test before (baseline) and 10-60 min after injection, at 4 days following induction of inflammation. In B and C, the doses given in brackets represent the U50 equivalent doses. To reduce animal numbers, one control group was used for all agonists, and it was treated with empty CMS-E (4 rats) or pCMS-E (4 rats) (50 mg kg^{-1}). #P < 0.05 vs. contralateral, non-inflamed paws, Wilcoxon test. *P < 0.05, **P < 0.01, ***P < 0.001 vs. control; two-way repeated measures ANOVA and Bonferroni test. Data are expressed as means ± SEM; n = 8 rats per group.

As evaluated by the area under the curve (AUC), the analgesic effect of U50+pCMS-E in the highest dose was significantly greater compared to U50 in the equivalent dose, in both inflamed

and non-inflamed paws (**Figure 7**). Additionally, both U50+CMS-E and U50+pCMS-E (in the two highest doses), but not U50, appeared to produce slight sedation-type behaviour (up to 30 min after injection). The sedative behaviour and analgesic effects in non-inflamed paws suggest that U50 derived from the carriers could cross the BBB and act centrally. However, the prolonged and enhanced analgesia indicates the retarded release of U50 from pCMS-E.

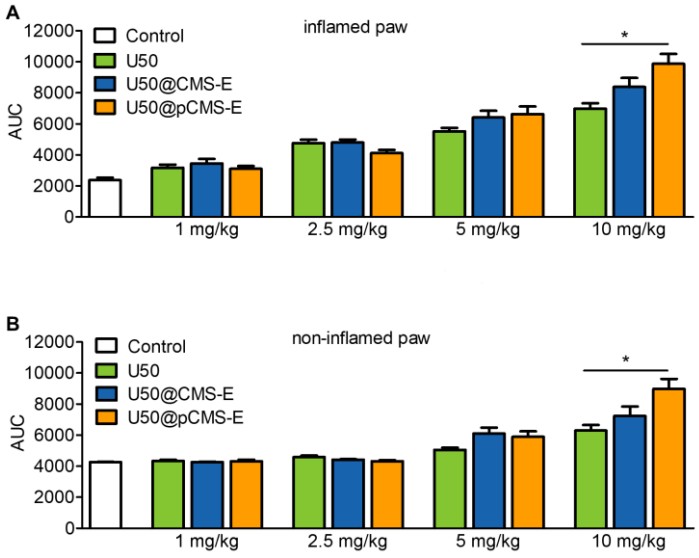

Figure 7. Analgesic effects after intravenous injection of U50, U50+CMS-E, and U50+pCMS-E in inflamed (A) and contralateral, non-inflamed paws (B) in rats with unilateral hind paw inflammation, expressed as area under the curve (AUC). The AUC values were calculated from the data depicted in Figure 7: The doses represent the U50 equivalent doses; the polymer doses were 5-50 mg kg^{-1}, respectively. The control group was treated with empty CMS-E (4 rats) or pCMS-E (4 rats) (50 mg kg^{-1}). *P < 0.05; Kruskal-Wallis one-way ANOVA and Dunn's test. Data are expressed as means ± SEM; n = 8 rats per group.

4. Conclusion

In this study, we presented the synthesis of two novel pCMS nanocarriers, pCMS-E and pCMS-A, that were able to encapsulate the analgesic drug U50 in high percentages. In subsequent release experiments, both pCMS exhibited a retarded release of U50, pCMS-E in a slightly pH-dependent manner. U50+pCMS-E was then selected to be tested in comparison to U50+CMS-E and U50 *in vivo* in the clinically relevant inflammatory pain model. Surprisingly, both U50-containing nanocarriers exerted analgesia in both inflamed and non-inflamed tissue, suggesting U50 systemic absorption and action in the central nervous system. Along with these effects, a prolonged and enhanced analgesia was observed when U50 was incorporated into the pCMS-E nanocarrier. These results suggest an increased blood circulation time of U50 carried by this type of nanoparticle and thus renders non-covalent binding of an analgesic a potential strategy

for the longer-lasting pain relieve. Future studies will be required to restrict the delivery of U50 to peripherally inflamed tissue and to further prevent unspecific leaching.

Supporting Information
Supporting Information is available from the Wiley Online Library or from the author.

Acknowledgements

This study was supported by Freie Universität Berlin (Focus Area DynAge) and Helmholtz Virtual Institute ("Multifunctional Biomaterials for Medicine"). The authors acknowledge Dr. Pamela Winchester for proof-reading the manuscript.

References

[1] H. Breivik, B. Collett, V. Ventafridda, R. Cohen, D. Gallacher, *Eur. J. Pain* **2006**, *10*, 287.

[2] I. Melnikova, *Nat. Rev. Drug Discov.* **2010**, *9*, 589.

[3] N. Bhala, J. Emberson, A. Merhi, S. Abramson, N. Arber, J. A. Baron, C. Bombardier, C. Cannon, M. E. Farkouh, G. A. FitzGerald, et al., *Lancet* **2013**, *382*, 769.

[4] K. B. Sondergaard, P. Weeke, M. Wissenberg, A.-M. Schjerning Olsen, E. L. Fosbol, F. K. Lippert, C. Torp-Pedersen, G. H. Gislason, F. Folke, *Eur. Hear. J. - Cardiovasc. Pharmacother.* **2017**, *3*, 100.

[5] S. P. Novak, A. Håkansson, J. Martinez-Raga, J. Reimer, K. Krotki, S. Varughese, *BMC Psychiatry* **2016**, *16*, 274.

[6] A. Schuchat, D. Houry, G. P. Guy, *JAMA* **2017**, *318*, 425.

[7] N. Volkow, H. Benveniste, A. T. McLellan, *Annu. Rev. Med.* **2018**, *69*, 451.

[8] A. Barber, R. Gottschlich, *Expert Opin. Investig. Drugs* **1997**, *6*, 1351.

[9] L. Lalanne, G. Ayranci, B. L. Kieffer, P.-E. Lutz, *Front. Psychiatry* **2014**, *5*, 170.

[10] C. Stein, M. J. Millan, T. S. Shippenberg, K. Peter, A. Herz, *J. Pharmacol. Exp. Ther.* **1989**, *248*.

[11] C. Stein, K. Comisel, E. Haimerl, A. Yassouridis, K. Lehrberger, A. Herz, K. Peter, *N. Engl. J. Med.* **1991**, *325*, 1123.

[12] D. Labuz, Y. Schmidt, A. Schreiter, H. L. Rittner, S. A. Mousa, H. Machelska, *J. Clin. Invest.* **2009**, *119*, 278.

[13] C. Stein, H. Machelska, *Pharmacol. Rev.* **2011**, *63*, 860.

[14] D. Labuz, H. Machelska, *J. Pharmacol. Exp. Ther.* **2013**, *346*, 535.

[15] M. Ö. Celik, D. Labuz, K. Henning, M. Busch-Dienstfertig, C. Gaveriaux-Ruff, B. L. Kieffer, A. Zimmer, H. Machelska, *Brain. Behav. Immun.* **2016**, *57*, 227.

[16] H. Machelska, M. Pflüger, W. Weber, M. Piranvisseh-Völk, J. D. Daubert, R. Dehaven, C. Stein, *J. Pharmacol. Exp. Ther.* **1999**, *290*, 354.

[17] E. de Paula, C. M. S. Cereda, L. F. Fraceto, D. R. de Araújo, M. Franz-Montan, G. R. Tofoli, J. Ranali, M. C. Volpato, F. C. Groppo, *Micro and Nanosystems for Delivering Local Anesthetics.*, Taylor & Francis, **2012**.

[18] Y.-Y. Tseng, S.-J. Liu, *Nanomedicine* **2015**, *10*, 1785.

[19] T. Görner, R. Gref, D. Michenot, F. Sommer, M. Tran, E. Dellacherie, *J. Control. Release* **1999**, *57*, 259.

[20] N. Wakiyama, K. Juni, M. Nakano, *Chem. Pharm. Bull. (Tokyo).* **1981**, *29*, 3363.

[21] C. M. Moraes, A. P. de Matos, E. de Paula, A. H. Rosa, L. F. Fraceto, *Mater. Sci. Eng. B* **2009**, *165*, 243.

[22] A. Kumari, S. K. Yadav, S. C. Yadav, *Colloids Surfaces B Biointerfaces* **2010**, *75*, 1.

[23] M. R. Radowski, A. Shukla, H. von Berlepsch, C. Böttcher, G. Pickaert, H. Rehage, R. Haag, *Angew. Chem. Int. Ed. Engl.* **2007**, *46*, 1265.

[24] I. N. Kurniasih, J. Keilitz, R. Haag, *Chem. Soc. Rev.* **2015**, *44*, 4145.

[25] N. Alnasif, C. Zoschke, E. Fleige, R. Brodwolf, A. Boreham, E. Rühl, K.-M. Eckl, H.-F. Merk, H. C. Hennies, U. Alexiev, et al., *J. Control. Release* **2014**, *185*, 45.

[26] M. A. Quadir, M. R. Radowski, F. Kratz, K. Licha, P. Hauff, R. Haag, *J. Control. Release* **2008**, *132*, 289.

[27] S. Küchler, M. R. Radowski, T. Blaschke, M. Dathe, J. Plendl, R. Haag, M. Schäfer-Korting, K. D. Kramer, *Eur. J. Pharm. Biopharm.* **2009**, *71*, 243.

[28] F. Du, S. Hönzke, F. Neumann, J. Keilitz, W. Chen, N. Ma, S. Hedtrich, R. Haag, *J. Control. Release* **2016**, *242*, 42.

[29] K. Walker, J.-F. Stumbé, R. Haag, *Polymers (Basel).* **2016**, *8*, 192.

[30] C. Rabe, E. Fleige, K. Vogtt, N. Szekely, P. Lindner, W. Burchard, R. Haag, M. Ballauff, *Polymer (Guildf).* **2014**, *55*, 6735.

[31] R. Schwarzl, F. Du, R. Haag, R. R. Netz, *Eur. J. Pharm. Biopharm.* **2017**, *116*, 131.

[32] S. Nowag, C. Frangville, G. Multhaup, J.-D. Marty, C. Mingotaud, R. Haag, *J. Mater. Chem. B* **2014**, *2*, 3915.

[33] G. Varchi, V. Benfenati, A. Pistone, M. Ballestri, G. Sotgiu, A. Guerrini, P. Dambruoso, A. Liscio, B. Ventura, *Photochem. Photobiol. Sci* **2013**, *12*, DOI 10.1039/c2pp25393c.

[34] E. Monti, M. B. Gariboldi, R. Ravizza, R. Molteni, K. Sparnacci, M. Laus, E. Gabano, M. Ravera, D. Osella, *Inorganica Chim. Acta* **2009**, *362*, 4099.

[35] S. Pocoví-Martínez, U. Kemmer-Jonas, J. Pérez-Prieto, H. Frey, S.-E. Stiriba, *Macromol. Chem. Phys.* **2014**, *215*, 2311.

[36] H. Nehoff, N. N. Parayath, L. Domanovitch, S. Taurin, K. Greish, *Int. J. Nanomedicine* **2014**, *9*, 2539.

[37] V. Spahn, G. Del Vecchio, D. Labuz, A. Rodriguez-Gaztelumendi, N. Massaly, J. Temp, V. Durmaz, P. Sabri, M. Reidelbach, H. Machelska, et al., *Science* **2017**, *355*, 966.

[38] A. Sunder, R. Hanselmann, H. Frey, R. Mülhaupt, *Macromolecules* **1999**, *32*, 4240.

[39] S. Roller, H. Zhou, R. Haag, *Mol. Divers.* **2005**, *9*, 305.

[40] G. R. Fulmer, A. J. M. Miller, N. H. Sherden, H. E. Gottlieb, A. Nudelman, B. M. Stoltz, J. E. Bercaw, K. I. Goldberg, *Organometallics* **2010**, *29*, 2176.

[41] M. Unbehauen, E. Fleige, F. Paulus, B. Schemmer, S. Mecking, S. Moré, R. Haag, *Polym. 2017, Vol. 9, Page 316* **2017**, *9*, 316.

[42] C. Kilkenny, W. J. Browne, I. C. Cuthill, M. Emerson, D. G. Altman, *PLoS Biol.* **2010**, *8*, e1000412.

[43] C. Stein, M. J. Millan, A. Herz, *Pharmacol. Biochem. Behav.* **1988**, *31*, 445.

[44] S. González-Rodríguez, M. A. Quadir, S. Gupta, K. A. Walker, X. Zhang, V. Spahn, D. Labuz, A. Rodriguez-Gaztelumendi, M. Schmelz, J. Joseph, et al., *Elife* **2017**, *6*, 1.

[45] M. L. Unbehauen, E. Fleige, F. Paulus, B. Schemmer, S. Mecking, S. D. Moré, R. Haag, *Polymers (Basel).* **2017**, *9*, DOI 10.3390/polym9080316.

[46] C. Häbler, *Klin. Wochenschr.* **1929**, *8*, 1569.

[47] Y. Woo, Cheol, S. S. Park, A. R. Subieta, T. J. Brennan, *Anesthesiol. J. Am. Soc. Anesthesiol.* **2004**, *101*, 468.

Full paper

Anionic Core-multishell Nanocarriers for the Delivery of Analgesics to Inflamed Tissue

*Michael L. Unbehauen, Dominika Łabuz, Richard Schwarzl, Sam Moré, Robert Bittl, Christoph Stein, Halina Machelska, Rainer Haag**

Michael L. Unbehauen, Prof. Dr. Rainer Haag
Institute for Chemistry and Biochemistry, Freie Universität Berlin, Berlin, Germany
E-mail: haag@chemie.fu-berlin.de
Dr. Dominika Łabuz, Prof. Dr. Christoph Stein, Prof. Dr. Halina Machelska,
Charité – Universitätsmedizin Berlin, corporate member of Freie Universität Berlin, Humboldt-Universität zu Berlin, and Berlin Institute of Health, Department of Anesthesiology and Critical Care Medicine, Campus Benjamin Franklin, Berlin, Germany
Richard Schwarzl, Prof. Dr. Robert Bittl
Institute of Physics, Freie Universität Berlin, Berlin, Germany
Dr. Sam Moré
DendroPharm GmbH, Arnimallee 14, 14195 Berlin, Germany

1. NMR-Spectra

1.1. pCMS-A

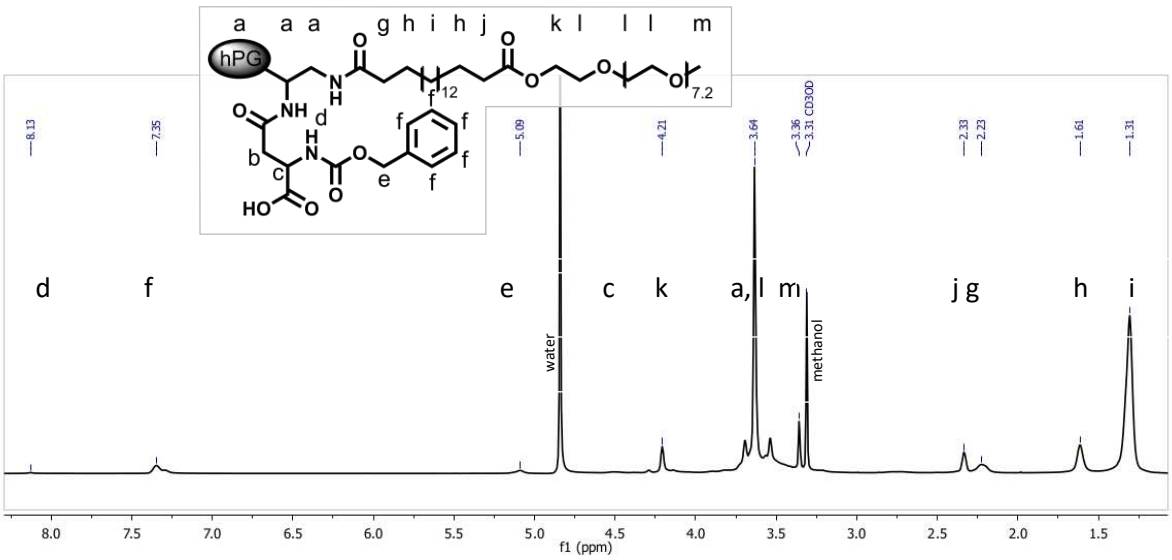

Figure S1. Chemical structure (box) and 1H-NMR spectrum of pCMS-A in methanol.

1.2. pCMS-E

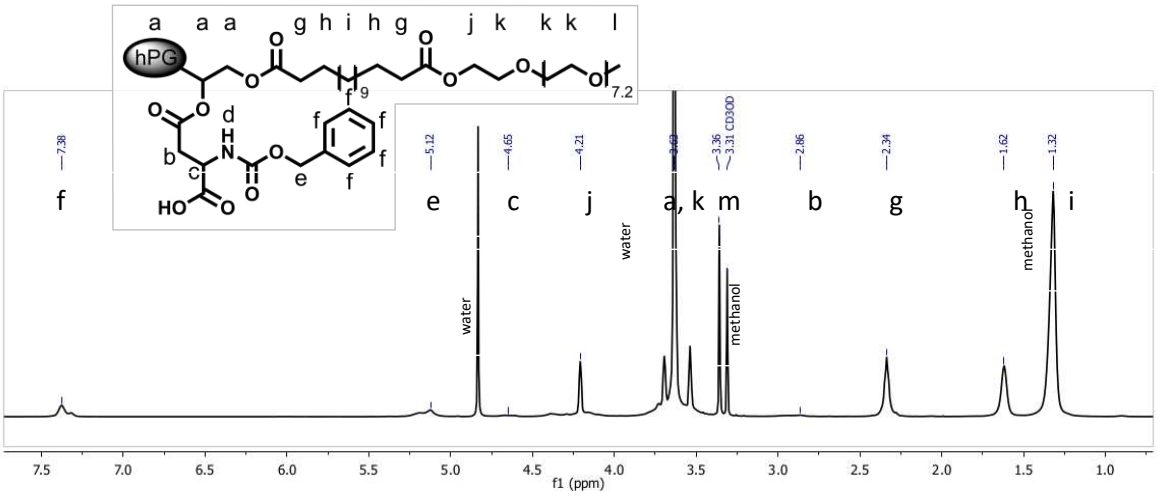

Figure S2. Chemical structure (box) and 1H-NMR spectrum of pCMS-E in methanol.

2. Release Kinetics of U50 from pCMS-E under various conditions

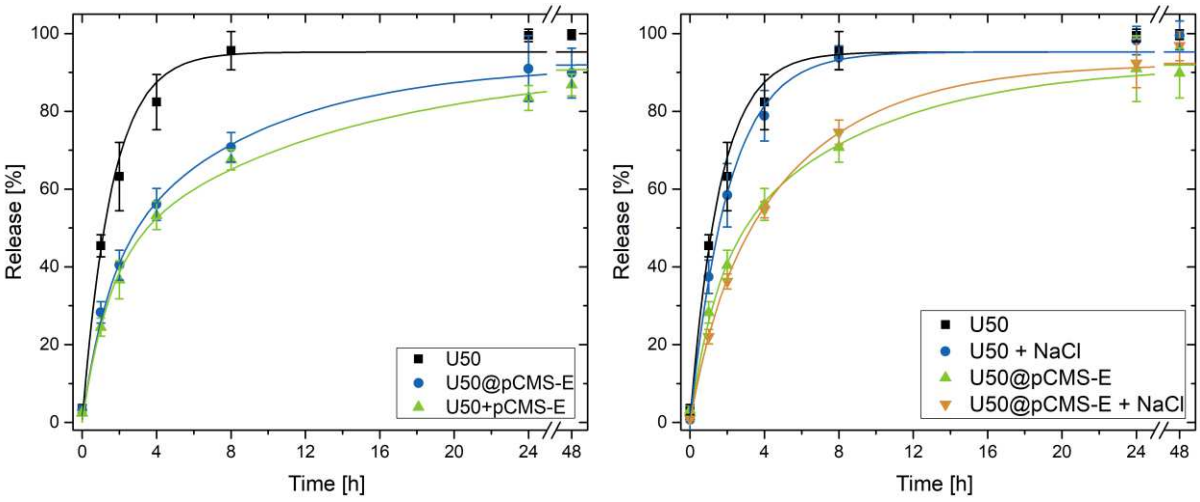

Figure S3. Release kinetics of U50 from pCMS-E under various conditions. Left: U50 without carrier (black), U50 encapsulated into pCMS-E (blue), and U50 co-dissolved as mesylate salt with pCMS-E (green). Right: U50,488 without carrier (black) and with 140 mM NaCl (blue), U50 encapsulated into pCMS-E with 140 mM NaCl (orange) and without (green), n=3.

3. Fitting functions for modelling

Equal to a previously developed mathematical model,[1] fitting Equation S1 describes the fraction of drug in the receptor medium. It was used to calibrate the system without carrier. Then the model was expanded by the presence and influence of the nanocarrier expressed by

the parameters s_3, as well as the diffusion rates from the nanocarrier into the donor solution and back (r_{NI} and r_{IN}), which yielded Equation S2.

$$\Phi_0(t) = r_{IM} r_{MI} \frac{s_1 - s_2 + s_2 e^{s_1 t} - s_1 e^{s_2 t}}{s_1 s_2 (s_1 - s_2)} \tag{S1}$$

$$\Phi_0(t) = r_{IM} r_{MI} \left[\frac{e^{s_1 t}(r_{NI} + s_1 \Phi_l^0)}{s_1(s_1 - s_2)(s_1 - s_3)} + \frac{e^{s_2 t}(r_{NI} + s_2 \Phi_l^0)}{s_2(s_2 - s_1)(s_2 - s_3)} + \frac{e^{s_3 t}(r_{NI} + s_3 \Phi_l^0)}{s_3(s_3 - s_1)(s_3 - s_2)} - \frac{r_{NI}}{s_1 s_2 s_3} \right] \tag{S2}$$

4. Normalised Release (NR)

The impact of the retention effect changes over time. To quantify the influence over the course of time, it was normalised. This was done by relating it to its control experiment which was conducted under the same conditions but without nanocarrier (see exemplarily Equation S3).

$$NR_{\mathrm{U50@CMS-A,pH\ 7.4}}(\mathrm{t}) = \frac{\Phi_{O;U50,pH\ 7.4}(t)}{\Phi_{O;\mathrm{U50@CMS-A,pH\ 7.4}}(t)} \tag{S3}$$

The results are depicted in Figure S4.

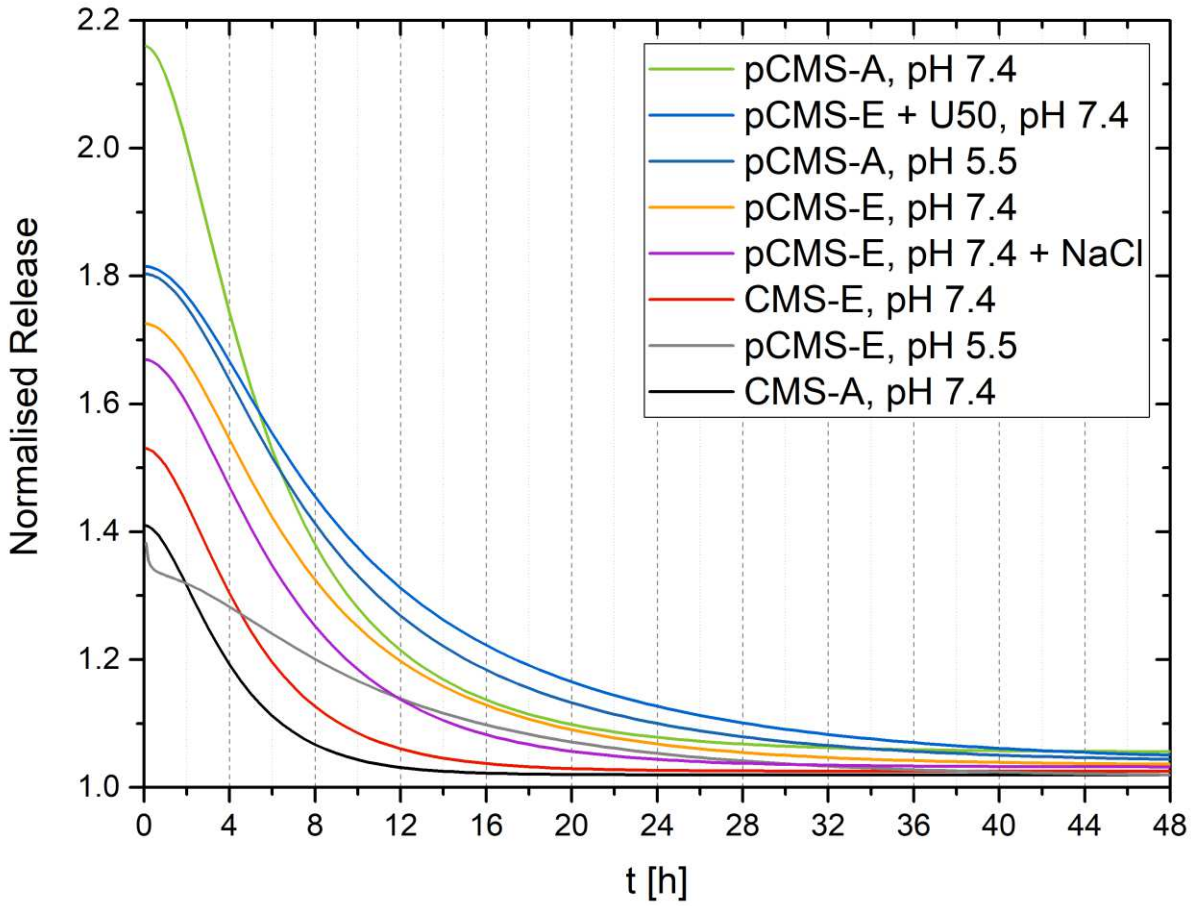

Figure S4. Normalized release of all investigated nanocarriers. The released amount without carrier was up to 2.2-fold higher than the one from the respective nanocarrier. The effect lasted between 4 and 12 hours.

5. Release time 50 (RT_{50})

The release time 50 is the time necessary for 50% of the U50 to reach the acceptor medium. Thus, it is used to reduce the measured retention to a single value. It was numerically determined based on the fitting functions obtained by the modelling of the measured data (see Section 3) and by employing Equation S5.

$$\Phi_O(\mathrm{t} = RT_{50}) = 0.5 \qquad \text{(S5)}$$

The values of each set of the release experiments are plotted in Figure S5.

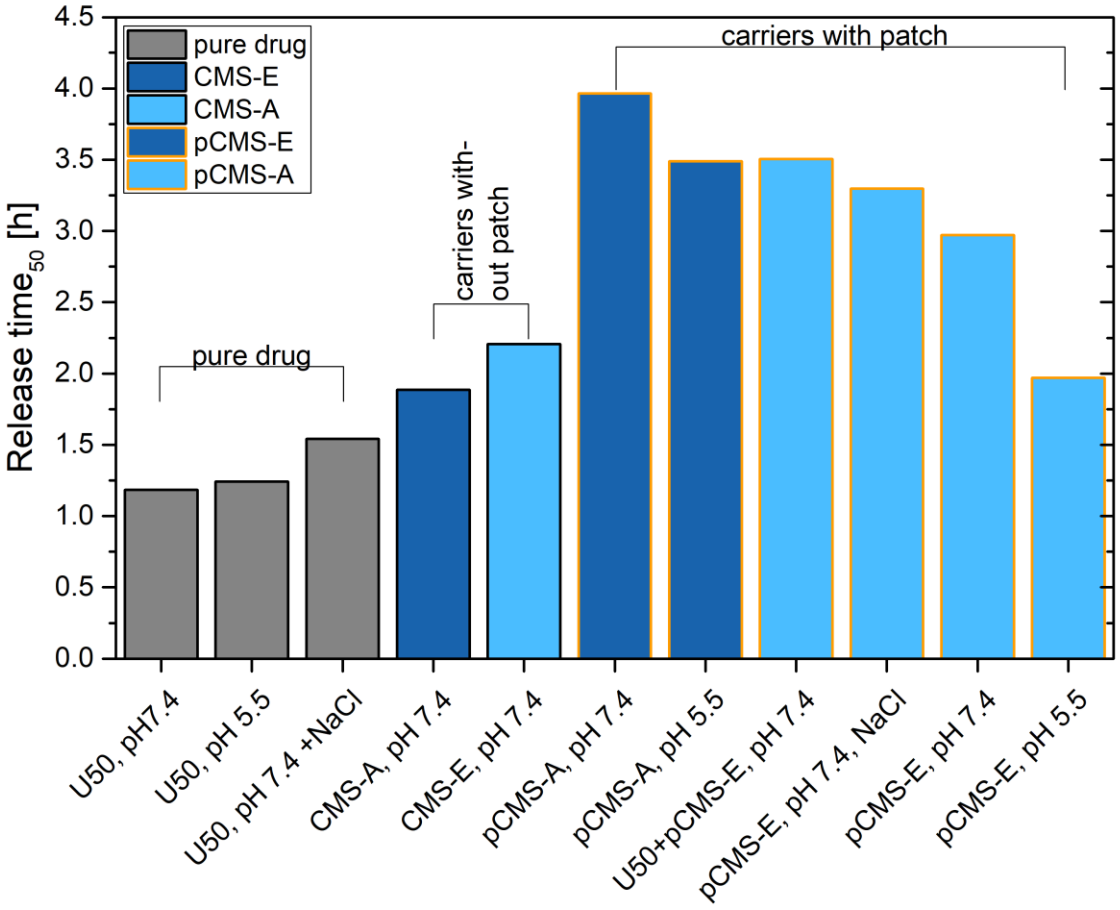

Figure S5. RT50 values for all investigated nanocarriers and the respective controls. The experiments were either carried out at pH 5.5 of 7.4, with (blue bars) or without a nanocarrier (grey bars) and with or without physiological salt concentration. The nanocarriers were either ester-based (light blue bars) or amide-based (dark blue bars) and optionally had an anchor group (orange border).

References

[1] R. Schwarzl, F. Du, R. Haag, R. R. Netz, *Eur. J. Pharm. Biopharm.* **2017**, *116*, 131.

4 Kurzzusammenfassung

In dieser Arbeit wurde das Design zwei verschiedener Nanocarrierarchitekturen realisiert mit dem Ziel, entweder niedermolekulare, hydrophobe Wirkstoffe zu verkapseln und deren Penetration in die Haut zu erhöhen, oder ein kationisches Analgesikum zielgerichtet in entzündetes Gewebe zu transportieren.

Im ersten Teil wurde von der bisher genutzten, Amid-basierten Synthesestrategie, zu einer Ester-basierten gewechselt, um erstens den potentiell toxischen Kernbaustein hPG-NH_2 zu vermeiden und zweitens, um die Bioabbaubarkeit zu verbessern. Des Weiteren wurden langkettige α-ω-Dicarbonsäuren mit verschiedenen Kettenlängen als Bausteine für die innere, lipophile Schale verwendet, und der Einfluss der Struktur dieses Bausteins auf Beladungskapazität, Schmelztemperatur und Abbau- bzw. Freisetzungskinetik untersucht. Während die Schmelztemperatur mit der Kettenlänge der inneren Schale stieg, sank sie mit zusätzlicher Verzweigung. Eine Amidgruppe hatte ebenfalls einen steigernden Effekt auf die Schmelztemperatur. Bei der Verkapselung des relativ rigiden Wirkstoffs Dexamethason (DXM) wurde kein starker Zusammenhang zwischen den verschiedenen Strukturen der inneren Schale und der Beladungskapazität beobachtet. Im Gegensatz dazu ergab sich bei dem eher flexiblen Makrozyklus Tacrolimus ein Maximum der Beladungskapazität bei einer mittleren Kettenlänge von C_{15}. Es konnte ferner gezeigt werden, dass unbeladene CMS nanocarrier von Lipasen innerhalb von 14 Tagen zu mehr als 70% abgebaut werden können, und dass DXM-beladene CMS Nanotransporter durch den Abbau ihre Ladung freisetzen.

Des Weiteren wurden einige der synthetisierten Systeme bezüglich ihrer Toxizität und Penetrationsverstärkung hin untersucht. Während sich CMS-E18 und vor allem der Doppelschalebaustein C_{18}-PEG_{350}, vermutlich aufgrund seiner Interaktion mit Zellmembranen als relativ toxisch erwies, konnte CMS-E15 als besonders biokompatibel identifiziert werden. Nachfolgende Tests mit Nilrot-beladenen CMS Nanocarriern auf exzidierter Humanhaut zeigten, dass Kettenlänge und Art der chemischen Bindung zum Kern keinen großen Einfluss auf die Penetrationsverstärkung hatten, alle untersuchten Architekturen jedoch einer Basiscreme überlegen waren. Untersuchungen mit DXM-beladenen CMS-E15 auf einem Entzündungshautmodell zeigten zudem, dass DXM im Vergleich zu einer

gleichkonzentrierten Creme eine höhere entzündungshemmende Wirkung entfalten konnte.

Weiterführende Studien auf Mundschleimhaut bestätigten die penetrations-verstärkende Wirkung von CMS Nanocarriern. Verkapseltes, spingelabeltes DXM konnte hier leichter in das Gewebe eindringen, als solches, das in einer Creme formuliert war. Außerdem drangen fluoreszenzmarkierte Nanocarrier verstärkt in die viable Epidermis ein, als dass auf normaler Haut gemessen wurde.

Der zweite Teil der Arbeit befasste sich mit der Aufnahme und der kontrollierten Freisetzung des kationischen aromatischen Analgesikums U 50,488 (U50). Zusätzliche Ankergruppen wurden am Kern befestigt, sodass U50 über ionische und aromatische Wechselwirkungen sowie Wasserstoffbrückenbindungen stärker an die CMS Nanocarrier gebunden wurde. Die mit Bindungspatches funktionalisierten CMS (pCMS) wurden hinsichtlich ihres pK_{app} charakterisiert, welcher wichtig für die Freisetzung ist. Bei der Bestimmung der Beladungskapazität mit U50 (freie Base) zeigten sich die pCMS den unfunktionalisierten Nanopartikeln überlegen. Dies wurde auch durch die anschließenden Freisetzungsstudien bestätigt. Während U50 aus CMS ohne Ankermolekül relativ schnell herausdiffundierte, war die Freisetzung aus pCMS wesentlich langsamer. Auch spielte es keine Rolle, ob Kochsalz in physiologischen Konzentrationen vorhanden war oder ob U50 als freie Base verkapselt oder in gleicher Konzentration als Methylsulfonat hinzugegeben wurde. Als einzige Architektur zeigte pCMS-E einen Unterschied im Freisetzungsverhalten bei pH 5.5 und pH 7.4. Dieses System wurde daraufhin in einem in vivo Rattenmodell getestet. Auch wenn hier kein erhöhter Transport ins entzündeten Gewebe nachgewiesen worden ist, zeigte sich eine verzögerte Freisetzung aus dem Nanocarrier, welche sich durch eine verstärkte und länger andauernde Analgesie ausdrückte.

5 Summary and Conclusion

This work explored the possibilities to design CMS nanocarriers for two different types of problems, the encapsulation of small hydrophobic drugs and subsequent transport into skin or the retention and targeted release of a cationic analgesic. The aim of the first part was to design a set of nanocarriers for the encapsulation and penetration enhancement of these drugs and thereby fulfilling the following criteria: Ease of synthesis, non-toxic products and building blocks, good loading capacity, degradability, and degradation-based release and high penetration enhancement.

To simplify the synthesis, the dendritic building block, which poses the focal point in the nanocarrier architecture, was exchanged. Instead of hPG-NH_2, unfunctionalized hPG was used. This change in the synthesis process had two main impacts. First, this strategy spared three synthetic steps thereby making the procedure less time consuming. Secondly, the potentially toxic building block hPG-NH_2 was avoided and thus could not harm the organism post-application as a degradation product. This change was the next step in decreasing the number of amine groups in the core and thus the toxicity ranging from PEI over hPG-NH_2 to hPG.[83,85] The inner shell's building block was varied in length to study the impact on encapsulation, melting temperature and penetration enhancement. Aliphatic diacids with a number of carbon atoms between 12 and 19 as well as a branched version of the one with 18 carbon atoms were used as inner shell building blocks. While, in previous studies, the length of the inner shell had already been altered with bigger steps (six C-atoms),[83] here the focus shifted more onto details and other structural features. The different systems showed an increase of the melting temperature (T_m), of the inner shell with increasing chain length. And while an amide bond in the structure significantly increased the T_m, the introduction of side arms led to its decrease. While the rigid molecule dexamethasone (DXM) showed no apparent correlation between chain length and loading capacity, the situation was different for the bulkier tacrolimus. Here, an optimum was found for a C_{15} inner shell. Interestingly, while the additional branching did not lead to results different from the linear ester-based architecture, the loading capacity plummeted when an amide-based nanocarrier was used.

All examined nanocarriers were degraded by a lipase to a degree of more than 70% in two weeks, which was similar to other ester-based nanotransporters.[124,125] The

degradation of DXM-loaded CMS nanotransporters led to the loss of their function as a solubilizer, more than 80% of the loading was released. Thus, the degradation can serve as a possible release mechanism.

Various assays were carried out to determine toxicity. Of the investigated ester-based CMS architectures, CMS-E15 showed the least cytotoxicity. The others caused a decrease in cell viability, at least to some extent. Of the building blocks, the aliphatic diacids were only toxic after prolonged exposition, but of the PEG-conjugated diacids, cytotoxicity increased from C12 to C18, which was attributed to interaction with the cell membrane. The most toxic building block was C18-PEG350, also with regard to genotoxicity. The CMS-E18 nanocarrier, the product of this building block, also exhibited some ROS generation and genotoxicity. The overall least toxic, ester-based nanocarrier was CMS-E15, which was selected for *in vivo* testing and was nontoxic when applied to the skin of Sprague Dawley rats.

After establishing the biocompatibility of the different candidates, the CMS nanocarriers were tested for skin penetration and penetration enhancement of several guest molecules on various skin models. Nile red-loaded and DXM-loaded CMS-nanocarriers were used to study the penetration enhancement on excised human skin. All nanocarriers proved to be superior over a formulation with base cream (NR) or LAW cream (DXM), which was in accordance with previous results.[85] The nanotransporters showed no dependence on inner shell chain length or type of bond for attachment. CMS-E15 was then loaded with dexamethasone and applied on an inflammatory skin model which had an upregulated interleukin 8 (IL-8) and IL-1β expression as part of their inflammatory condition. The application of the DXM-loaded nanocarriers reduced the expression of both ILs more effectively than a LAW cream with equal DXM content.

The CMS nanocarrier was not only tested for application on skin, but for oral mucosa as well. Here, biocompatibility was of even higher importance, because the constant flow of saliva eventually flushed the CMS nanocarriers into the GI tract if not taken up by the mucosa. Along the penetration experiment, toxicity of the CMS nanotransporters was determined for gingival epithelial cells and found to be only cytotoxic at very high concentrations. The penetration enhancement of PCA-labeled dexamethasone encapsulated in CMS-E15 and the penetration of ICC-labeled, amide

based CMS nanocarriers (CMS-ICC) was measured on buccal and masticatory mucosa. While penetration of unloaded CMS-ICC nanocarriers was limited to the stratum corneum on skin,[122] a small fraction also penetrated more deeply into viable tissues, in masticatory slightly more than in buccal mucosa. Although the conditions were not identical, this result might have indicated a higher penetrability for oral mucosa compared to skin, which might be related to a difference in the structure of both tissues. For the penetration enhancement of spin-labeled DXM (DXM-PCA) by CMS-E15, similar results were found as in skin. Even after a washing step, which simulated the flow of saliva in the oral cavity, penetration enhancement of the labeled drug was found. The CMS nanotransporters enhanced the penetration of DXM-PCA more than a cream formulation, and buccal mucosa generally seemed more penetrable than masticatory mucosa for DXM-PCA. Additionally, X-band electron paramagnetic resonance spectroscopy revealed that the guest molecule left its vehicle. This observation was in accordance with previous observations,[122] which indicated that nanocarrier and guest molecule penetrated up to different depths. Taken together, these three studies describe a step-wise selection process at which out of six different initial candidates, one was selected by criteria like ease of synthesis, drug loading capacity, and biocompatibility. The nanocarrier with the best overall performance and thus most promising for future applications was CMS-E15.

The aim of the second part of this work was to design a nanocarrier for the encapsulation and controlled release of the drug U 50,488H (U50), which is a strong analgesic for the post-operational pain treatment but elicits side effects when it crosses the blood brain barrier. A formulation into a nanocarrier can help to increase circulation time and facilitate targeted release. After surgery, the tissue is inflamed and thereby acidified and fenestrated. To use these conditions for the targeted release of U50, a nanocarrier was synthesized that offered the possibility to encapsulate U50 efficiently and release it in a pH-dependent manner.

As basic architectures, CMS-E15 and CMS-A18, which were the most promising candidates in previous studies, were used and extended by an anchor moiety. It was needed, because there was no possibility to bind the drug covalently to the nanocarrier. For this task, N-Z-L-protected aspartic acid was utilized, because it offered the possibility for ionic interactions, π-π stacking, and hydrogen bonds to U50. Further, it was possible to employ the carboxylic acid groups for a pH-dependent

release. While many approaches in literature used a hydrophobic segment that was ionized upon a pH change and thus,[126–128] a lipophilic guest is expelled, here, the opposite is the case. Ionic interactions are interrupted and thus the ionic drug can diffuse out of the nanocarrier.

After synthesis, the pK_{app} of the carboxylic acid groups was determined to be in the physiological range (4.4 for pCMS-A and 5.4 for pCMS-E) and the loading capacity (LC) and encapsulation efficiency (EE) for U50 free base was measured. While the EE at 16 wt% feed already exceeded 10% for all nanocarriers (> 60% EE), the feed was increased to 48 wt%. Under these conditions, the LC of all nanoarchitectures could be increased, especially for the pCMS, which reached up to 28% (> 50% EE). Subsequently, the release kinetics were studied under various conditions to determine the influence of the additional functionalization and factors like pH, the encapsulation of the free base or the methylsulfonate salt, or the presence of physiological salt concentration. While the latter two had no influence on the release kinetics, the functionalization with the binding patch was beneficial for the retention of U50. In the case of pCMS-A, there was no difference in this effect at pH 5.5 and 7.4, but for pCMS-E, a pH dependence was found. For this reason, pCMS-E was selected for an *in vivo* study in rats. Here, formulations of U50 with and without pCMS-E were compared regarding prolonged analgesia and reduced side effects. While the latter one was not the case, the formulation with additional pCMS-E resulted in the enhancement and the extension of the analgesic effect, which might indicate a longer blood circulation time caused by the nanocarrier. In a previous prodrug approach, morphine covalently attached to hPG was tested under similar conditions and the absence of a systemic side effect reported.[61] Taken together, these two studies indicated that to optimize post-operational pain treatment, nanocarrier architectures ideally have a sufficiently high molecular weight for a prolonged blood circulation time and bind the analgesic tightly enough to prevent premature release. If possible, this should be realized in a DDS approach, to make the drug interchangeable.

When first reported, the core-multishell nanocarrier was termed universal, because it was suitable for both hydrophilic and hydrophobic guest molecules in both aqueous and organic media. Subsequent studies confirmed that and reported the encapsulation of even inorganic nanoparticles and explored the fundamental effects, such as the aggregation of nanoparticles and guest molecules, which were also described

theoretically. In a more application-focused approach, many nanocarriers were designed for a certain guest, e.g., copper ions, or target, for instance, the endosome. Ideally both can be achieved, namely, the identification of a promising architecture and further insight into fundamental effects.

In this work, this was achieved. In the first part, it could be shown that there is an optimum chain length for the encapsulation tacrolimus and that the addition of one CH_2 group to the aliphatic chain can alter the nanocarrier's properties dramatically. There also was a dependence of cytotoxicity on the length of the hydrophobic part of the amphiphilic double shell, which altogether identified CMS-E15 as the most promising candidate. Addressing oral mucosa with CMS showed that this is an interesting field for DDS like CMS nanocarriers, because even more efficient penetration seems to be possible.

In the more application-focused second part, the pH-dependent retention effect that was measured for the best candidate pCMS-E. Even though the encapsulation of hydrophilic guest molecules remains a greater challenge than the formulation of hydrophobic ones, this showed that it was possible even for rather small nanocarrier systems (diameter ~10 nm) to bind a water-soluble drug. Additionally, it could be proven that the chemistry used to attach the anchor moiety influenced the pK_{app} and thus is crucial for the application. Different anchor molecules could be employed to further fine-tune the pH of release and the retention effect proven in this study might be improved by increasing the nanocarrier's sizes. One advantage of the DDS-approach is that pCMS are a potential nanocarrier suitable for any aromatic, hydrophobic drug molecule that bears a positive charge, e.g. by an amino group.

The past research conducted on CMS nanocarriers has shown that, starting from a universal nanocarrier, of which mainly fundamental effects have been studied, many subclasses and varieties have been realized to meet specific requirements. To be suitable for future applications, a universal nanocarrier will not be able to solve all the problems. It will be necessary to adapt the nanocarrier's architecture to the requirements of drug and physiological condition. And to achieve that, a library of CMS nanocarriers is needed to study fundamental effects and to select a potential candidate for an application. It is important to design new architectures, because the human body's complexity demands specialized DDS for specific applications. This work has

not only extended the library, but also identified certain novel nanocarriers as promising candidates.

6 Outlook

Based on the current findings, the following projects could yield interesting nanocarriers or approaches for applications:

Size has a substantial influence on the distribution of a DDS in the body, drug loading capacity, and release kinetics. Construction of a nanocarrier with a bigger and more accessible core can improve drug loading and limit diffusion out of the DDS. To obtain a low-PDI core, tecto-dendrimers, which are core-shell constructs of dendrimers, can be used. They are defined and are known to transport guest molecules, so the nanocarrier will not only have the shell, but also the core volume to encapsulate drug molecules.

As the pCMS showed the promising ability to encapsulate U50, other amine-containing hydrophobic drugs might also benefit from this tailored functionalization. Tofacitinib is currently in clinical trials for psoriasis treatment. Encapsulation in pCMS could increase skin penetration and thus the effect of this drug. Also, a pCMS-based formulation could improve the efficacy of micro-needle vaccinations.

In applications to the oral cavity, the flux of saliva usually poses a problem. A solution could be to employ a two-component system. CMS nanocarriers penetrate mucus relatively quickly and enter the stratum corneum, but are partially washed away by the flow of saliva. To prevent this, a mucus-binding macrogel could be used to formulate the CMS nanotransporters to improve residence time.

7 Literature

1. Strebhardt, K.; Ullrich, A. Paul Ehrlich's magic bullet concept: 100 years of progress. *Nat. Rev. Cancer* **2008**, *8*, 473–480, doi:10.1038/nrc2394.

2. *Fundamentals and Applications of Controlled Release Drug Delivery*; Siepmann, J., Siegel, R. A., Rathbone, M. J., Eds.; Springer US: Boston, MA, 2012; ISBN 978-1-4614-0880-2.

3. Haag, R.; Kratz, F. Polymere Therapeutika: Konzepte und Anwendungen. *Angew. Chemie* **2006**, *118*, 1218–1237, doi:10.1002/ange.200502113.

4. Hurwitz, E.; Levy, R.; Maron, R.; Wilchek, M.; Arnon, R.; Sela, M. The covalent binding of daunomycin and adriamycin to antibodies, with retention of both drug and antibody activities. *Cancer Res.* **1975**, *35*, 1175–81.

5. Caliceti, P.; Veronese, F. M. Pharmacokinetic and biodistribution properties of poly(ethylene glycol)–protein conjugates. *Adv. Drug Deliv. Rev.* **2003**, *55*, 1261–1277, doi:10.1016/S0169-409X(03)00108-X.

6. Ringsdorf, H. Structure and properties of pharmacologically active polymers. *J. Polym. Sci. Polym. Symp.* **1975**, *51*, 135–153, doi:10.1002/polc.5070510111.

7. Matsumura, Y.; Maeda, H. A new concept for macromolecular therapeutics in cancer chemotherapy: mechanism of tumoritropic accumulation of proteins and the antitumor agent smancs. *Cancer Res.* **1986**, *46*, 6387–92.

8. Jain, R. K. Transport of molecules across tumor vasculature. *CANCER METASTASIS Rev.* **1987**, *6*, 559–593, doi:10.1007/BF00047468.

9. Haag, R.; Kratz, F. Polymer therapeutics: Concepts and applications. *Angew. Chemie - Int. Ed.* **2006**, *45*, 1198–1215, doi:10.1002/anie.200502113.

10. Kobayashi, H.; Choyke, P. L. Super enhanced permeability and retention (SUPR) effects in tumors following near infrared photoimmunotherapy. *Nanoscale* **2016**, *8*, doi:10.1039/c5nr05552k.

11. Duncan, R.; Vicent, M. J. Polymer therapeutics-prospects for 21st century: The end of the beginning. *Adv. Drug Deliv. Rev.* **2013**, *65*, 60–70, doi:10.1016/J.ADDR.2012.08.012.

12. Fleige, E. Dendritic Core-Multishell Nanocarriers for the Delivery of Active Compounds, 2013.

13. Vicent, M. J.; Duncan, R. Polymer conjugates: nanosized medicines for treating cancer. *Trends Biotechnol.* **2006**, *24*, 39–47, doi:10.1016/J.TIBTECH.2005.11.006.

14. Ettinger, A. R. Pegaspargase (Oncaspar). *J. Pediatr. Oncol. Nurs.* **1995**, *12*, 46–48, doi:10.1177/104345429501200110.

15. Nowotnik, D. P.; Cvitkovic, E. ProLindac™ (AP5346): A review of the development of an HPMA DACH platinum Polymer Therapeutic. *Adv. Drug Deliv. Rev.* **2009**, *61*, 1214–1219, doi:10.1016/J.ADDR.2009.06.004.

16. Allen, T. M.; Cullis, P. R. Drug delivery systems: entering the mainstream. *Science* **2004**, *303*, 1818–22, doi:10.1126/science.1095833.

17. Fanciullino, R.; Ciccolini, J. Liposome-Encapsulated Anticancer Drugs: Still Waiting for the Magic Bullet? *Curr. Med. Chem.* **2009**, *16*, 4361–4373, doi:10.2174/092986709789712916.

18. Donati, G.; Kapetanios, A. D.; Pournaras, C. J. Principles of Treatment of Choroidal Neovascularization with Photodynamic Therapy in Age-Related Macular Degeneration. *Semin. Ophthalmol.* **1999**, *14*, 2–10, doi:10.3109/08820539909056057.

19. Arnold, J.; Barbezetto, I.; Birngruber, R.; Bressler, N. M.; Bressler, S. B.; Donati, G.; Fish, G. E.; Flaxel, C. J.; Gragoudas, E. S.; Harvey, P.; Kaiser, P. K.; Koester, J. M.; Lewis, H.; Lim, J. I.; Ma, C.; Meredith, T. A.; Miller, J. W.; Mones, J.; Murphy, S. A.; Pieramici, D. J.; Potter, M. J.; Reaves, A.; Rosenfeld, P. J.; Schachat, A. P.; Schmidt-Erfurth, U.; Singerman, L.; Strong, H. A.; Stur, M.; Williams, G. A. Verteporfin therapy of subfoveal choroidal neovascularization in age-related macular degeneration: Two-year results of a randomized clinical trial including lesions with occult with no classic choroidal neovascularization - Verteporfin in photodynamic the. *Am. J. Ophthalmol.* **2001**, *131*, 541–560, doi:10.1016/S0002-9394(01)00967-9.

20. Mellish, K. J.; Brown, S. B. Expert Opinion on Pharmacotherapy Verteporfin: a milestone in opthalmology and photodynamic therapy Verteporfin: a milestone in opthalmology and photodynamic therapy. *Expert Opin. Pharmacother.* **2001**, *2*, 351–361, doi:10.1517/14656566.2.2.351doi.org/10.1517/14656566.2.2.351.

21. Northfelt, D. W.; Martin, F. J.; Working, P.; Volberding, P. A.; Russell, J.; Newman, M.; Amantea, M. A.; Kaplan, L. D.; Voiberding, P. A.; Martin, J.; Kaplan, D. Doxorubicin Encapsulated in Liposomes Containing Polyethylene Glycol : Tumor and Safety in Patients with Kaposi ' s Sarcoma. *J. Clin. Pharmacol.* **1996**, *36*, 55–63, doi:10.1002/j.1552-4604.1996.tb04152.x.

22. Barenholz, Y. (Chezy) Doxil® — The first FDA-approved nano-drug: Lessons learned. *J. Control. Release* **2012**, *160*, 117–134, doi:10.1016/J.JCONREL.2012.03.020.

23. Wu, W.; Jiang, X. Polymeric Micelles for Drug Delivery. In *Biomedical Nanomaterials*; Wiley-VCH Verlag GmbH & Co. KGaA: Weinheim, Germany, 2016; pp. 87–97 ISBN 9783527694396.

24. Ishida, T.; Harada, M.; Wang, X. Y.; Ichihara, M.; Irimura, K.; Kiwada, H. Accelerated blood clearance of PEGylated liposomes following preceding liposome injection: Effects of lipid dose and PEG surface-density and chain length of the first-dose liposomes. *J. Control. Release* **2005**, *105*, 305–317, doi:10.1016/J.JCONREL.2005.04.003.

25. Ishida, T.; Ichihara, M.; Wang, X.; Yamamoto, K.; Kimura, J.; Majima, E.; Kiwada, H. Injection of PEGylated liposomes in rats elicits PEG-specific IgM, which is responsible for rapid elimination of a second dose of PEGylated liposomes. *J. Control. Release* **2006**, *112*, 15–25, doi:10.1016/J.JCONREL.2006.01.005.

26. Gaucher, G.; Asahina, K.; Wang, J.; Leroux, J.-C. Effect of Poly(N -vinyl-pyrrolidone)-block -poly(d , l -lactide) as Coating Agent on the Opsonization, Phagocytosis, and Pharmacokinetics of Biodegradable Nanoparticles. *Biomacromolecules* **2009**, *10*, 408–416, doi:10.1021/bm801178f.

27. Ishihara, T.; Maeda, T.; Sakamoto, H.; Takasaki, N.; Shigyo, M.; Ishida, T.; Kiwada, H.; Mizushima, Y.; Mizushima, T. Evasion of the Accelerated Blood Clearance Phenomenon by Coating of Nanoparticles with Various Hydrophilic Polymers. *Biomacromolecules* **2010**, *11*, 2700–2706, doi:10.1021/bm100754e.

28. Kim, T.-Y.; Kim, D.-W.; Chung, J.-Y.; Shin, S. G.; Kim, S.-C.; Heo, D. S.; Kim, N. K.; Bang, Y.-J. Phase I and pharmacokinetic study of Genexol-PM, a cremophor-free, polymeric micelle-formulated paclitaxel, in patients with advanced malignancies. *Clin. Cancer Res.* **2004**, *10*, 3708–16, doi:10.1158/1078-0432.CCR-03-0655.

29. Wang, H.; Zhao, Y.; Wu, Y.; Hu, Y.; Nan, K.; Nie, G.; Chen, H. Enhanced anti-tumor efficacy by co-delivery of doxorubicin and paclitaxel with amphiphilic methoxy PEG-PLGA copolymer nanoparticles. *Biomaterials* **2011**, *32*, 8281–8290, doi:10.1016/J.BIOMATERIALS.2011.07.032.

30. Zhu, Z.; Li, Y.; Li, X.; Li, R.; Jia, Z.; Liu, B.; Guo, W.; Wu, W.; Jiang, X. Paclitaxel-loaded poly(N-vinylpyrrolidone)-b-poly(ε-caprolactone) nanoparticles: Preparation and antitumor activity in vivo. *J. Control. Release* **2010**, *142*, 438–446, doi:10.1016/J.JCONREL.2009.11.002.

31. Adams, M. L.; Lavasanifar, A.; Kwon, G. S. Amphiphilic block copolymers for drug delivery. *J. Pharm. Sci.* **2003**, *92*, 1343–1355, doi:10.1002/jps.10397.

32. Phillips, D. J.; Gibson, M. I. Redox-Sensitive Materials for Drug Delivery: Targeting the Correct Intracellular Environment, Tuning Release Rates, and Appropriate Predictive Systems. *Antioxid. Redox Signal.* **2014**, *21*, 786–803, doi:10.1089/ars.2013.5728.

33. Low, S. A.; Yang, J.; Kopeček, J. Bone-Targeted Acid-Sensitive Doxorubicin Conjugate Micelles as Potential Osteosarcoma Therapeutics. *Bioconjug. Chem.* **2014**, *25*, 2012–2020, doi:10.1021/bc500392x.

34. Gillies, E. R.; Fréchet, J. M. J. Dendrimers and dendritic polymers in drug delivery. *Drug Discov. Today* **2005**, *10*, 35–43, doi:10.1016/S1359-6446(04)03276-3.

35. Gao, C.; Yan, D. Hyperbranched polymers: from synthesis to applications. *Prog. Polym. Sci.* **2004**, *29*, 183–275, doi:10.1016/J.PROGPOLYMSCI.2003.12.002.

36. Tomalia, D. A.; Baker, H.; Dewald, J.; Hall, M.; Kallos, G.; Martin, S.; Roeck, J.; Ryder, J.; Smith, P. A New Class of Polymers: Starburst-Dendritic Macromolecules. *Polym. J.* **1985**, *17*, 117–132, doi:10.1295/polymj.17.117.

37. de Gennes, P. G.; Hervet, H. Statistics of « starburst » polymers. *J. Phys. Lettres* **1983**, *44*, 351–360, doi:10.1051/jphyslet:01983004409035100.

38. Hawker, C. J.; Frechet, J. M. J. Preparation of polymers with controlled molecular architecture. A new convergent approach to dendritic macromolecules. *J. Am. Chem. Soc.* **1990**, *112*, 7638–7647, doi:10.1021/ja00177a027.

39. Nanjwade, B. K.; Bechra, H. M.; Derkar, G. K.; Manvi, F. V.; Nanjwade, V. K. Dendrimers: Emerging polymers for drug-delivery systems. *Eur. J. Pharm. Sci.* **2009**, *38*, 185–196, doi:10.1016/J.EJPS.2009.07.008.

40. Grayson, S. M.; Jayaraman, M.; Fréchet, J. M. J. Convergent synthesis and “surface” functionalization of a dendritic analog of poly(ethylene glycol). *Chem. Commun.* **1999**, 1329–1330, doi:10.1039/a902340b.

41. Carnahan, M. A.; Grinstaff, M. W. Synthesis and characterization of poly(glycerol-succinic acid) dendrimers. *Macromolecules* **2001**, *34*, 7648–7655, doi:10.1021/ma010848n.

42. Kesharwani, P.; Jain, K.; Jain, N. K. Dendrimer as nanocarrier for drug delivery. *Prog. Polym. Sci.* **2014**, *39*, 268–307, doi:10.1016/j.progpolymsci.2013.07.005.

43. Rupp, R.; Rosenthal, S. L.; Stanberry, L. R. VivaGel™(SPL7013 Gel): A candidate

dendrimer–microbicide for the prevention of HIV and HSV infection. *Int. J. Nanomedicine* **2007**, *2*, 561.

44. McCarthy, T. D.; Karellas, P.; Henderson, S. A.; Giannis, M.; O'Keefe, D. F.; Heery, G.; Paull, J. R. A.; Matthews, B. R.; Holan, G. Dendrimers as drugs: Discovery and preclinical and clinical development of dendrimer-based microbicides for HIV and STI prevention. *Mol. Pharm.* **2005**, *2*, 312–318, doi:10.1021/mp050023q.

45. Jansen, J. F.; de Brabander-van den Berg, E. M.; Meijer, E. W. Encapsulation of guest molecules into a dendritic box. *Science* **1994**, *266*, 1226–9, doi:10.1126/science.266.5188.1226.

46. Jansen, J. F. G. A.; Meijer, E. W.; de Brabander-van den Berg, E. M. M. The Dendritic Box: Shape-Selective Liberation of Encapsulated Guests. *J. Am. Chem. Soc.* **1995**, *117*, 4417–4418, doi:10.1021/ja00120a032.

47. Svenson, S. Dendrimers as versatile platform in drug delivery applications. *Eur. J. Pharm. Biopharm.* 2009, *71*, 445–462.

48. Kienle, R. H.; Hovey, A. G. THE POLYHYDRIC ALCOHOL-POLYBASIC ACID REACTION. I. GLYCEROL-PHTHALIC ANHYDRIDE. *J. Am. Chem. Soc.* **1929**, *51*, 509–519, doi:10.1021/ja01377a021.

49. Flory, P. J. Molecular Size Distribution in Three Dimensional Polymers. I. Gelation. *J. Am. Chem. Soc.* **1941**, *63*, 3083–3090, doi:10.1021/ja01856a061.

50. Santra, S.; Kaittanis, C.; Perez, J. M. Cytochrome c Encapsulating Theranostic Nanoparticles: A Novel Bifunctional System for Targeted Delivery of Therapeutic Membrane-Impermeable Proteins to Tumors and Imaging of Cancer Therapy. *Mol. Pharm.* **2010**, *7*, 1209–1222, doi:10.1021/mp100043h.

51. Akinc, A.; Thomas, M.; Klibanov, A. M.; Langer, R. Exploring polyethylenimine-mediated DNA transfection and the proton sponge hypothesis. *J. Gene Med.* **2005**, *7*, 657–663, doi:10.1002/jgm.696.

52. Staedtler, A. M.; Hellmund, M.; Sheikhi Mehrabadi, F.; Thota, B. N. S.; Zollner, T. M.; Koch, M.; Haag, R.; Schmidt, N. Optimized effective charge density and size of polyglycerol amines leads to strong knockdown efficacy in vivo. *J. Mater. Chem. B* **2015**, *3*, 8993–9000, doi:10.1039/C5TB01466B.

53. Chen, Y.; Zhou, L.; Pang, Y.; Huang, W.; Qiu, F.; Jiang, X.; Zhu, X.; Yan, D.; Chen, Q. Photoluminescent Hyperbranched Poly(amido amine) Containing β-Cyclodextrin as a

Nonviral Gene Delivery Vector. *Bioconjug. Chem.* **2011**, *22*, 1162–1170, doi:10.1021/bc200010w.

54. Hellmund, M.; Achazi, K.; Neumann, F.; Thota, B. N. S.; Ma, N.; Haag, R. Systematic adjustment of charge densities and size of polyglycerol amines reduces cytotoxic effects and enhances cellular uptake. *Biomater. Sci.* **2015**, doi:10.1039/c5bm00187k.

55. Sunder, A.; Hanselmann, R.; Frey, H.; Mülhaupt, R. Controlled synthesis of hyperbranched polyglycerols by ring-opening multibranching polymerization. *Macromolecules* **1999**, *32*, 4240–4246.

56. Calderón, M.; Quadir, M. A.; Sharma, S. K.; Haag, R. Dendritic Polyglycerols for Biomedical Applications. *Adv. Mater.* **2010**, *22*, 190–218, doi:10.1002/adma.200902144.

57. Frey, H.; Haag, R. Dendritic polyglycerol: a new versatile biocompatible material. *Rev. Mol. Biotechnol.* **2002**, *90*, 257–267, doi:10.1016/S1389-0352(01)00063-0.

58. Kainthan, R. K.; Brooks, D. E. In vivo biological evaluation of high molecular weight hyperbranched polyglycerols. *Biomaterials* **2007**, *28*, 4779–4787, doi:10.1016/j.biomaterials.2007.07.046.

59. Kainthan, R. K.; Hester, S. R.; Levin, E.; Devine, D. V.; Brooks, D. E. In vitro biological evaluation of high molecular weight hyperbranched polyglycerols. *Biomaterials* **2007**, *28*, 4581–4590, doi:10.1016/J.BIOMATERIALS.2007.07.011.

60. Jeong, J. H.; Schmidt, J. J.; Kohman, R. E.; Zill, A. T.; DeVolder, R. J.; Smith, C. E.; Lai, M.-H.; Shkumatov, A.; Jensen, T. W.; Schook, L. G.; Zimmerman, S. C.; Kong, H. Leukocyte-Mimicking Stem Cell Delivery via in Situ Coating of Cells with a Bioactive Hyperbranched Polyglycerol. *J. Am. Chem. Soc.* **2013**, *135*, 8770–8773, doi:10.1021/ja400636d.

61. González-Rodríguez, S.; Quadir, M. A.; Gupta, S.; Walker, K. A.; Zhang, X.; Spahn, V.; Labuz, D.; Rodriguez-Gaztelumendi, A.; Schmelz, M.; Joseph, J.; Parr, M. K.; Machelska, H.; Haag, R.; Stein, C. Polyglycerol-opioid conjugate produces analgesia devoid of side effects. *Elife* **2017**, *6*, 1–24, doi:10.7554/eLife.27081.

62. Gao, S.; Guan, Q.; Chafeeva, I.; Brooks, D. E.; Nguan, C. Y. C.; Kizhakkedathu, J. N.; Du, C. Hyperbranched Polyglycerol as a Colloid in Cold Organ Preservation Solutions. *PLoS One* **2015**, *10*, e0116595, doi:10.1371/journal.pone.0116595.

63. Li, S.; Constantinescu, I.; Guan, Q.; Kalathottukaren, M. T.; Brooks, D. E.; Nguan, C.

Y. C.; Kizhakkedathu, J. N.; Du, C. Advantages of replacing hydroxyethyl starch in University of Wisconsin solution with hyperbranched polyglycerol for cold kidney perfusion. *J. Surg. Res.* **2016**, *205*, 59–69, doi:10.1016/j.jss.2016.06.015.

64. Li, S.; Liu, B.; Guan, Q.; Chafeeva, I.; Brooks, D. E.; Nguan, C. Y.; Kizhakkedathu, J. N.; Du, C. Cold preservation with hyperbranched polyglycerol-based solution improves kidney functional recovery with less injury at reperfusion in rats. *Am. J. Transl. Res.* **2017**, *9*, 429–441.

65. Abbina, S.; Vappala, S.; Kumar, P.; Siren, E. M. J.; La, C. C.; Abbasi, U.; Brooks, D. E.; Kizhakkedathu, J. N. Hyperbranched polyglycerols: recent advances in synthesis, biocompatibility and biomedical applications. *J. Mater. Chem. B* **2017**, *5*, 9249–9277, doi:10.1039/C7TB02515G.

66. Sisson, A. L.; Haag, R. Polyglycerol nanogels: highly functional scaffolds for biomedical applications. *Soft Matter* **2010**, *6*, 4968, doi:10.1039/c0sm00149j.

67. Kurniasih, I. N.; Keilitz, J.; Haag, R. Dendritic nanocarriers based on hyperbranched polymers. *Chem. Soc. Rev.* **2015**, *44*, 4145–4164, doi:10.1039/C4CS00333K.

68. Sisson, A. L.; Papp, I.; Landfester, K.; Haag, R. Functional nanoparticles from dendritic precursors: Hierarchical assembly in miniemulsion. *Macromolecules* **2009**, *42*, 556–559, doi:10.1021/ma802238e.

69. Steinhilber, D.; Witting, M.; Zhang, X.; Staegemann, M.; Paulus, F.; Friess, W.; Küchler, S.; Haag, R. Surfactant free preparation of biodegradable dendritic polyglycerol nanogels by inverse nanoprecipitation for encapsulation and release of pharmaceutical biomacromolecules. *J. Control. Release* **2013**, *169*, 289–295, doi:10.1016/J.JCONREL.2012.12.008.

70. Dimde, M.; Neumann, F.; Reisbeck, F.; Ehrmann, S.; Cuellar-Camacho, J. L.; Steinhilber, D.; Ma, N.; Haag, R. Defined pH-sensitive nanogels as gene delivery platform for siRNA mediated in vitro gene silencing. *Biomater. Sci.* **2017**, *5*, 2328–2336, doi:10.1039/C7BM00729A.

71. Giulbudagian, M.; Hönzke, S.; Bergueiro, J.; Işık, D.; Schumacher, F.; Saeidpour, S.; Lohan, S. B.; Meinke, M. C.; Teutloff, C.; Schäfer-Korting, M.; Yealland, G.; Kleuser, B.; Hedtrich, S.; Calderón, M. Enhanced topical delivery of dexamethasone by β-cyclodextrin decorated thermoresponsive nanogels. *Nanoscale* **2018**, *10*, 469–479, doi:10.1039/C7NR04480A.

72. Newkome, G. R.; Moorefield, C. N.; Baker, G. R.; Saunders, M. J.; Grossman, S. H.

Unimolecular Micelles. *Angew. Chemie Int. Ed. English* **1991**, *30*, 1178–1180, doi:10.1002/anie.199111781.

73. Newkome, G. R.; Moorefield, C. N.; Baker, G. R.; Johnson, A. L.; Behera, R. K. Alkane Cascade Polymers Possessing Micellar Topology: Micellanoic Acid Derivatives. *Angew. Chemie Int. Ed. English* **1991**, *30*, 1176–1178, doi:10.1002/anie.199111761.

74. Hawker, C. J.; Wooley, K. L.; Fréchet, J. M. J. Unimolecular micelles and globular amphiphiles: dendritic macromolecules as novel recyclable solubilization agents. *J. Chem. Soc., Perkin Trans. 1* **1993**, *0*, 1287–1297, doi:10.1039/P19930001287.

75. Lukowiak, M. C.; Thota, B. N. S.; Haag, R. Dendritic core–shell systems as soft drug delivery nanocarriers. *Biotechnol. Adv.* **2015**, *33*, 1327–1341, doi:http://dx.doi.org/10.1016/j.biotechadv.2015.03.014.

76. Singh, P.; Gupta, U.; Asthana, A.; Jain, N. K. Folate and Folate−PEG−PAMAM Dendrimers: Synthesis, Characterization, and Targeted Anticancer Drug Delivery Potential in Tumor Bearing Mice. *Bioconjug. Chem.* **2008**, *19*, 2239–2252, doi:10.1021/bc800125u.

77. Jin, Y.; Ren, X.; Wang, W.; Ke, L.; Ning, E.; Du, L.; Bradshaw, J. A 5-fluorouracil-loaded pH-responsive dendrimer nanocarrier for tumor targeting. *Int. J. Pharm.* **2011**, *420*, 378–384, doi:10.1016/J.IJPHARM.2011.08.053.

78. Kurniasih, I. N.; Liang, H.; Rabe, J. P.; Haag, R. Supramolecular Aggregates of Water Soluble Dendritic Polyglycerol Architectures for the Solubilization of Hydrophobic Compounds. *Macromol. Rapid Commun.* **2010**, *31*, 1516–1520, doi:10.1002/marc.201000112.

79. Kurniasih, I. N.; Liang, H.; Kumar, S.; Mohr, A.; Sharma, S. K.; Rabe, J. P.; Haag, R. A bifunctional nanocarrier based on amphiphilic hyperbranched polyglycerol derivatives. *J. Mater. Chem. B* **2013**, *1*, 3569, doi:10.1039/c3tb20366b.

80. Chen, G.; Guan, Z. Transition Metal-Catalyzed One-Pot Synthesis of Water-Soluble Dendritic Molecular Nanocarriers. *J. Am. Chem. Soc.* **2004**, *126*, 2662–2663, doi:10.1021/ja039829e.

81. Popeney, C. S.; Lukowiak, M. C.; Böttcher, C.; Schade, B.; Welker, P.; Mangoldt, D.; Gunkel, G.; Guan, Z.; Haag, R. Tandem Coordination, Ring-Opening, Hyperbranched Polymerization for the Synthesis of Water-Soluble Core–Shell Unimolecular Transporters. *ACS Macro Lett.* **2012**, *1*, 564–567, doi:10.1021/mz300083y.

82. Chen, H.; Li, G.; Chi, H.; Wang, D.; Tu, C.; Pan, L.; Zhu, L.; Qiu, F.; Guo, F.; Zhu, X. Alendronate-Conjugated Amphiphilic Hyperbranched Polymer Based on Boltorn H40 and Poly(ethylene glycol) for Bone-Targeted Drug Delivery. *Bioconjug. Chem.* **2012**, *23*, 1915–1924, doi:10.1021/bc3003088.

83. Radowski, M. R.; Shukla, A.; von Berlepsch, H.; Böttcher, C.; Pickaert, G.; Rehage, H.; Haag, R. Supramolecular aggregates of dendritic multishell architectures as universal nanocarriers. *Angew. Chem. Int. Ed. Engl.* **2007**, *46*, 1265–9, doi:10.1002/anie.200603801.

84. Quadir, M. A.; Radowski, M. R.; Kratz, F.; Licha, K.; Hauff, P.; Haag, R. Dendritic multishell architectures for drug and dye transport. *J. Control. Release* **2008**, *132*, 289–94, doi:10.1016/j.jconrel.2008.06.016.

85. Küchler, S.; Radowski, M. R.; Blaschke, T.; Dathe, M.; Plendl, J.; Haag, R.; Schäfer-Korting, M.; Kramer, K. D. Nanoparticles for skin penetration enhancement--a comparison of a dendritic core-multishell-nanotransporter and solid lipid nanoparticles. *Eur. J. Pharm. Biopharm.* **2009**, *71*, 243–50, doi:10.1016/j.ejpb.2008.08.019.

86. Fleige, E.; Ziem, B.; Grabolle, M.; Haag, R.; Resch-Genger, U. Aggregation Phenomena of Host and Guest upon the Loading of Dendritic Core-Multishell Nanoparticles with Solvatochromic Dyes. *Macromolecules* **2012**, *45*, 9452–9459, doi:10.1021/ma301977r.

87. Rabe, C.; Fleige, E.; Vogtt, K.; Szekely, N.; Lindner, P.; Burchard, W.; Haag, R.; Ballauff, M. The multi-domain nanoparticle structure of a universal core-multi-shell nanocarrier. *Polymer (Guildf).* **2014**, *55*, 6735–6742, doi:10.1016/j.polymer.2014.10.061.

88. Boreham, A.; Pfaff, M.; Fleige, E.; Haag, R.; Alexiev, U. Nanodynamics of dendritic core-multishell nanocarriers. *Langmuir* **2014**, *30*, 1686–95, doi:10.1021/la4043155.

89. Weber, M.; Zoschke, C.; Sedighi, A.; Fleige, E.; Haag, R.; Schäfer-Korting, M. Free Energy Simulations of Cargo-Carrier Interactions for Core-Multishell Nanotransporters. *J. Nanomed. Nanotechnol.* **2014**, *5*, doi:10.4172/2157-7439.1000234.

90. Keilitz, J.; Schwarze, M.; Nowag, S.; Schomäcker, R.; Haag, R. Homogeneous Stabilization of Pt Nanoparticles in Dendritic Core-Multishell Architectures: Application in Catalytic Hydrogenation Reactions and Recycling. *ChemCatChem* **2010**, *2*, 863–870, doi:10.1002/cctc.201000013.

91. Nowag, S.; Frangville, C.; Multhaup, G.; Marty, J.-D.; Mingotaud, C.; Haag, R.

Biocompatible, hyperbranched nanocarriers for the transport and release of copper ions. *J. Mater. Chem. B* **2014**, *2*, 3915–3918, doi:10.1039/C4TB00454J.

92. Prabaharan, M.; Grailer, J. J.; Pilla, S.; Steeber, D. A.; Gong, S. Amphiphilic Multi-Arm Block Copolymer Based on Hyperbranched Polyester, Poly(L-lactide) and Poly(ethylene glycol) as a Drug Delivery Carrier. *Macromol. Biosci.* **2009**, *9*, 515–524, doi:10.1002/mabi.200800269.

93. Prabaharan, M.; Grailer, J. J.; Pilla, S.; Steeber, D. A.; Gong, S. Folate-conjugated amphiphilic hyperbranched block copolymers based on Boltorn® H40, poly(l-lactide) and poly(ethylene glycol) for tumor-targeted drug delivery. *Biomaterials* **2009**, *30*, 3009–3019, doi:10.1016/J.BIOMATERIALS.2009.02.011.

94. Xu, W.; Siddiqui, I. A.; Nihal, M.; Pilla, S.; Rosenthal, K.; Mukhtar, H.; Gong, S. Aptamer-conjugated and doxorubicin-loaded unimolecular micelles for targeted therapy of prostate cancer. *Biomaterials* **2013**, *34*, 5244–5253, doi:10.1016/J.BIOMATERIALS.2013.03.006.

95. Fleige, E.; Quadir, M. A.; Haag, R. Stimuli-responsive polymeric nanocarriers for the controlled transport of active compounds: concepts and applications. *Adv. Drug Deliv. Rev.* **2012**, *64*, 866–84, doi:10.1016/j.addr.2012.01.020.

96. Schafer, F. Q.; Buettner, G. R. Redox environment of the cell as viewed through the redox state of the glutathione disulfide/glutathione couple. *Free Radic. Biol. Med.* **2001**, *30*, 1191–1212, doi:10.1016/S0891-5849(01)00480-4.

97. Carlisle, R. C.; Etrych, T.; Briggs, S. S.; Preece, J. A.; Ulbrich, K.; Seymour, L. W. Polymer-coated polyethylenimine/DNA complexes designed for triggered activation by intracellular reduction. *J. Gene Med.* **2004**, *6*, 337–344, doi:10.1002/jgm.525.

98. Liu, J.; Pang, Y.; Huang, W.; Huang, X.; Meng, L.; Zhu, X.; Zhou, Y.; Yan, D. Bioreducible Micelles Self-Assembled from Amphiphilic Hyperbranched Multiarm Copolymer for Glutathione-Mediated Intracellular Drug Delivery. *Biomacromolecules* **2011**, *12*, 1567–1577, doi:10.1021/bm200275j.

99. Schmaljohann, D. Thermo- and pH-responsive polymers in drug delivery. *Adv. Drug Deliv. Rev.* **2006**, *58*, 1655–1670, doi:10.1016/J.ADDR.2006.09.020.

100. Fluhr, J. W.; Elias, P. M. Stratum corneum pH: Formation and Function of the “Acid Mantle.” *Exog. Dermatology* **2002**, *1*, 163–175, doi:10.1159/000066140.

101. Vaupel, P.; Kallinowski, F.; Okunieff, P. Blood flow, oxygen and nutrient supply, and

metabolic microenvironment of human tumors: a review. *Cancer Res.* **1989**, *49*, 6449–65.

102. Spahn, V.; Del Vecchio, G.; Labuz, D.; Rodriguez-Gaztelumendi, A.; Massaly, N.; Temp, J.; Durmaz, V.; Sabri, P.; Reidelbach, M.; Machelska, H.; Weber, M.; Stein, C. A nontoxic pain killer designed by modeling of pathological receptor conformations. *Science* **2017**, *355*, 966–969, doi:10.1126/science.aai8636.

103. Mukherjee, S.; Ghosh, R. N.; Maxfield, F. R. Endocytosis. *Physiol. Rev.* **1997**, *77*, 759–803, doi:10.1152/physrev.1997.77.3.759.

104. Li, H. J.; Du, J. Z.; Liu, J.; Du, X. J.; Shen, S.; Zhu, Y. H.; Wang, X.; Ye, X.; Nie, S.; Wang, J. Smart Superstructures with Ultrahigh pH-Sensitivity for Targeting Acidic Tumor Microenvironment: Instantaneous Size Switching and Improved Tumor Penetration. *ACS Nano* **2016**, *10*, 6753–6761, doi:10.1021/acsnano.6b02326.

105. Calderón, M.; Welker, P.; Licha, K.; Fichtner, I.; Graeser, R.; Haag, R.; Kratz, F. Development of efficient acid cleavable multifunctional prodrugs derived from dendritic polyglycerol with a poly(ethylene glycol) shell. *J. Control. Release* **2011**, *151*, 295–301, doi:10.1016/J.JCONREL.2011.01.017.

106. Fleige, E.; Achazi, K.; Schaletzki, K.; Triemer, T.; Haag, R. pH-Responsive Dendritic Core-Multishell Nanocarriers. *J. Control. Release* **2014**, *185*, 99–108, doi:10.1016/j.jconrel.2014.04.019.

107. Mao, J.; Gan, Z. The Influence of Pendant Hydroxyl Groups on Enzymatic Degradation and Drug Delivery of Amphiphilic Poly[glycidol- *block* -(ε -caprolactone)] Copolymers. *Macromol. Biosci.* **2009**, *9*, 1080–1089, doi:10.1002/mabi.200900104.

108. Calderón, M.; Graeser, R.; Kratz, F.; Haag, R. Development of enzymatically cleavable prodrugs derived from dendritic polyglycerol. *Bioorg. Med. Chem. Lett.* **2009**, *19*, 3725–3728, doi:10.1016/J.BMCL.2009.05.058.

109. Khandare, J. J.; Jayant, S.; Singh, A.; Chandna, P.; Wang, Y.; Vorsa, N.; Minko, T. Dendrimer versus linear conjugate: Influence of polymeric architecture on the delivery and anticancer effect of paclitaxel. *Bioconjug. Chem.* **2006**, *17*, 1464–1472, doi:10.1021/bc060240p.

110. Vogt, A.; Wischke, C.; Neffe, A. T.; Ma, N.; Alexiev, U. Nanocarriers for drug delivery into and through the skin — Do existing technologies match clinical challenges? *J. Control. Release* **2016**, *242*, 3–15, doi:10.1016/J.JCONREL.2016.07.027.

111. Menon, G. K. New insights into skin structure: scratching the surface. *Adv. Drug Deliv. Rev.* **2002**, *54*, S3–S17, doi:10.1016/S0169-409X(02)00121-7.

112. Elias, P. M. Structure and function of the stratum corneum permeability barrier. *Drug Dev. Res.* **1988**, *13*, 97–105, doi:10.1002/ddr.430130203.

113. Liang, X.; Xu, Z.; Grice, J.; Zvyagin, A.; Roberts, M.; Liu, X. Penetration of Nanoparticles into Human Skin. *Curr. Pharm. Des.* **2013**, *19*, 6353–6366, doi:10.2174/1381612811319350011.

114. Mitragotri, S. A theoretical analysis of permeation of small hydrophobic solutes across the stratum corneum based on Scaled Particle Theory. *J. Pharm. Sci.* **2002**, *91*, 744–752, doi:10.1002/jps.10048.

115. Lipinski, C. A.; Lombardo, F.; Dominy, B. W.; Feeney, P. J. Experimental and computational approaches to estimate solubility and permeability in drug discovery and development settings. *Adv. Drug Deliv. Rev.* **2001**, *46*, 3–26, doi:10.1016/S0169-409X(00)00129-0.

116. Vogt, A.; Combadiere, B.; Hadam, S.; Stieler, K. M.; Lademann, J.; Schaefer, H.; Autran, B.; Sterry, W.; Blume-Peytavi, U. 40 nm, but not 750 or 1,500 nm, Nanoparticles Enter Epidermal CD1a+ Cells after Transcutaneous Application on Human Skin. *J. Invest. Dermatol.* **2006**, *126*, 1316–1322, doi:10.1038/SJ.JID.5700226.

117. Patzelt, A.; Richter, H.; Knorr, F.; Schäfer, U.; Lehr, C.-M.; Dähne, L.; Sterry, W.; Lademann, J. Selective follicular targeting by modification of the particle sizes. *J. Control. Release* **2011**, *150*, 45–48, doi:10.1016/j.jconrel.2010.11.015.

118. Radtke, M.; Patzelt, A.; Knorr, F.; Lademann, J.; Netz, R. R. Ratchet effect for nanoparticle transport in hair follicles. *Eur. J. Pharm. Biopharm.* **2017**, *116*, 125–130, doi:10.1016/J.EJPB.2016.10.005.

119. García Ortiz, P.; Hansen, S. H.; Shah, V. P.; Menné, T.; Benfeldt, E. Impact of adult atopic dermatitis on topical drug penetration: Assessment by cutaneous microdialysis and tape stripping. *Acta Derm. Venereol.* **2009**, *89*, 33–38, doi:10.2340/00015555-0562.

120. Lin, Y.-K.; Yang, S.-H.; Chen, C.-C.; Kao, H.-C.; Fang, J.-Y. Using Imiquimod-Induced Psoriasis-Like Skin as a Model to Measure the Skin Penetration of Anti-Psoriatic Drugs. *PLoS One* **2015**, *10*, e0137890, doi:10.1371/journal.pone.0137890.

121. Xing, J.; Deng, L.; Li, J.; Dong, A. Amphiphilic poly{[alpha-maleic anhydride-omega-

methoxy-poly(ethylene glycol)]-co-(ethyl cyanoacrylate)} graft copolymer nanoparticles as carriers for transdermal drug delivery. *Int. J. Nanomedicine* **2009**, *4*, 227–32.

122. Alnasif, N.; Zoschke, C.; Fleige, E.; Brodwolf, R.; Boreham, A.; Rühl, E.; Eckl, K.-M.; Merk, H.-F.; Hennies, H. C.; Alexiev, U.; Haag, R.; Küchler, S.; Schäfer-Korting, M. Penetration of normal, damaged and diseased skin--an in vitro study on dendritic core-multishell nanotransporters. *J. Control. Release* **2014**, *185*, 45–50, doi:10.1016/j.jconrel.2014.04.006.

123. Witting, M.; Molina, M.; Obst, K.; Plank, R.; Eckl, K. M.; Hennies, H. C.; Calderón, M.; Frieß, W.; Hedtrich, S. Thermosensitive dendritic polyglycerol-based nanogels for cutaneous delivery of biomacromolecules. *Nanomedicine Nanotechnology, Biol. Med.* **2015**, *11*, 1179–1187, doi:10.1016/J.NANO.2015.02.017.

124. Stefani, S.; Kurniasih, I. N.; Sharma, S. K.; Böttcher, C.; Servin, P.; Haag, R. Triglycerol-based hyperbranched polyesters with an amphiphilic branched shell as novel biodegradable drug delivery systems. *Polym. Chem.* **2016**, *7*, 887–898, doi:10.1039/C5PY01314C.

125. Walker, K.; Stumbé, J.-F.; Haag, R. Polyester-Based, Biodegradable Core-Multishell Nanocarriers for the Transport of Hydrophobic Drugs. *Polymers (Basel).* 2016, *8*, 192.

126. Marie-Christine Jones, †; Maxime Ranger, ‡ and; Jean-Christophe Leroux†, * pH-Sensitive Unimolecular Polymeric Micelles: Synthesis of a Novel Drug Carrier. **2003**, doi:10.1021/BC020041F.

127. Sant, V. P.; Smith, D.; Leroux, J.-C. Novel pH-sensitive supramolecular assemblies for oral delivery of poorly water soluble drugs: preparation and characterization. *J. Control. Release* **2004**, *97*, 301–312, doi:10.1016/J.JCONREL.2004.03.026.

128. Cabane, E.; Zhang, X.; Langowska, K.; Palivan, C. G.; Meier, W. Stimuli-Responsive Polymers and Their Applications in Nanomedicine. *Biointerphases* **2012**, *7*, 9, doi:10.1007/s13758-011-0009-3.